Fall 2013

Semiconductor Nanomaterial Development For Photovoltaic And Thermoelectric Applications

Liangliang Chen
Purdue University

Graduate School ETD Form 9
(Revised 12/07)

PURDUE UNIVERSITY
GRADUATE SCHOOL
Thesis/Dissertation Acceptance

This is to certify that the thesis/dissertation prepared

By Liangliang Chen

Entitled
SEMICONDUCTOR NANOMATERIAL DEVELOPMENT FOR PHOTOVOLTAIC AND THERMOELECTRIC APPLICATIONS

For the degree of Doctor of Philosophy

Is approved by the final examining committee:

Xiulin Ruan
Chair

Xianfan Xu

Timothy Fisher

Alexander Wei

To the best of my knowledge and as understood by the student in the *Research Integrity and Copyright Disclaimer (Graduate School Form 20)*, this thesis/dissertation adheres to the provisions of Purdue University's "Policy on Integrity in Research" and the use of copyrighted material.

Approved by Major Professor(s): Xiulin Ruan

Approved by: Dave Anderson 09/17/2013
Head of the Graduate Program Date

SEMICONDUCTOR NANOMATERIAL DEVELOPMENT FOR PHOTOVOLTAIC AND THERMOELECTRIC APPLICATIONS

A Dissertation

Submitted to the Faculty

of

Purdue University

by

Liangliang Chen

In Partial Fulfillment of the

Requirements for the Degree

of

Doctor of Philosophy

December 2013

Purdue University

West Lafayette, Indiana

ACKNOWLEDGEMENTS

First, I would like to thank my major advisor Professor Xiulin Ruan for bringing me to Purdue, teaching me how to do research, helping me through countless number of challenges during my PhD study and offering tremendous help during my job hunting. We have been working together for more than 5 years. In the past five years, we started our lab from scratch and eventually built up our current lab in Birck Nanotechnology Center. We discussed what we want to do and what we can do, designed our experiments, purchased scientific instrument and chemicals, set up the synthesis and characterization methods, did the experiments and addressed the challenges, and finally obtained useful data to wrap up my PhD research. Without the support and guidance from Professor Ruan, I can't imagine how any of these would come true. During my job hunting, Professor Ruan always forwarded me useful information and wrote helpful recommendation letters for me. This is the best support I can imagine from an advisor to his students. I will always feel deeply connected with the lab and devote my knowledge and skills to the continuous growth of the lab.

I also want to express special thanks to my other committee members, Professor Xianfan Xu, Professor Alexander Wei, and Professor Timothy Fisher.

Professor Xu has generously granted me access to his laser equipment and appointed a post doctor to train me and help me set up the laser equipment so that I could perform

ultrafast laser spectroscopy experiments on my CdSe nanocrystals and experimentally study the hot electron relaxation dynamics in them.

Professor Alexander Wei has been generously sharing with me his knowledge in wet chemistry and pointing out to me the important knowledge and skills that I have missed in my wet chemistry experiments. Before talking to Professor Wei, I didn't pay much attention to the fundamental knowledge related to my research. I didn't recognize its importance until Profess Wei asked me some challenging questions during my preliminary examination. Since then, I have been paying special attention to and spending more time on fundamental chemistry knowledge and therefore become more confident in explaining my research data in terms of fundamental theory and knowledge rather than just quoting other researchers' results.

Professor Timothy Fisher has generously granted me access to his lab in Birck Nanotechnology Center and allowed me to use his equipment for photovoltaic characterization on our solar cell devices. His lab is so well organized and always runs smoothly even if there are many users using the lab simultaneously. I have learned a lot from the way he runs his lab and transplanted some of their lab management experience to our own lab.

I'd also like to thank both my current and previous co-workers, Hua Bao, Bryan Spann, Bo Qiu, Dr Wenzhi Wu, Wonjun Park, Luis A Jauregui, Qing Zhao, Kelly Rickey, Christopher Robinson, Dr Venkataprasad Bhat, Ajit Vallabhaneni, Bhagirath Duvvuri, Hao Wu, Jingjing Shi, Xiangyu Li, Zexi Lu, Zuyuan Wang, Qiong Nian, Dr Shanglong Xu, and Yalin Dong.

Hua Bao is an expert in simulations. He has taught me how to use VASP and helped me use VASP to study the phonon assisted hot electron relaxation dynamics in CdSe nanomaterials.

Wonjun Park and Luis A Jauregui have spent a lot of time training me to use their Raman spectrometer and programmable temperature controlling system to perform temperature-dependent Raman spectroscopy experiments on CdSe nanocrystals, even if they are already busy with their own work. Every time I have a need to use their equipment, they try their best to find out some free time slot for me at the sacrifice of their own time.

Haiyu Fang and Haoran Yang have helped train me on Seebeck coefficient measurement system in Professor Yue Wu's lab. Dr Wenzhi Wu, Dr Yaguo Wang and Dr Karl Liebig have given me training on ultrafast laser equipment and helped me set up equipment for ultrafast laser experiment. Sergey Suslov has spent a lot of nights training me on FIB and TEM and solving technical problems for me whenever I encounter them.

Christopher Robinson has helped in ball milling and hot pressing experiments. Kelly Rickey has helped in wet chemistry synthesis, Seebeck coefficient measurement and SEM characterization. Qing Zhao, Yiwen Chen, Karl Rodney Tucker JR, and Taizhi Tan have helped in wet chemistry synthesis and nanocrystal characterization. Haoxiang has helped in setting up and calibrating absorption and transmission spectrometer. The help from them has ensured the outcome of our research project even when I have to spend a large fraction of time on data processing, paper writing and thesis writing.

Bryan Spann, Bo Qiu, Dr Wenzhi Wu, Dr Venkataprasad Bhat, Ajit Vallabhaneni, Bhagirath Duvvuri, Hao Wu, Jingjing Shi, Xiangyu Li, Zexi Lu, Zuyuan Wang, Qiong

Nian, Dr Shanglong Xu, and Yalin Dong have also been very helpful in providing constructive feedback regarding my presentation slides and manuscripts.

At the end, I want to thank my family and friends, Andy Kyger, Guoping Xiong, Gang Yang, Lei Jin, and Nick Green for always being there for me whenever I need someone to talk to.

TABLE OF CONTENTS

LIST OF FIGURES

Figure Page

LIST OF TABLES

LIST OF ABBREVIATIONS

CB:	conduction band
DFT:	density functional theory
DOS:	density of states
DPE:	diphenyl ether
ECE:	energy conversion efficiency
EQD:	elongated quantum dot
FSSH:	fewest switch surface hopping
FTIR:	Fourier transform infrared spectroscopy
HOMO:	highest occupied molecular orbital
HPA:	hexylphosphonic acid
IR:	infra red
KS:	Kohn-Sham
LUMO:	lowest unoccupied molecular orbital
MD:	molecular dynamics
NC:	nanocrystal
NR:	nanorod
NW:	nanowire
OA:	oleic acid

ODE: 1-octadecene

QD: spherical quantum dot

QR: quantum rod

SEM: scanning electron microscopy

TDPA: tetradecylphosphonic acid

TEM: transmission electron microscopy

TOP: tri-n-octylphosphine

TOPO: tri-n-octylphosphine oxide

VASP: Vienna Ab initio Simulation Package

VB: valence band

XRD: x-ray diffraction

ABSTRACT

Chen, Liangliang, Ph.D., Purdue University, December 2013. Semiconductor Nanomaterial Development for Photovoltaic and Thermoelectric Applications. Major Professor: Xiulin Ruan, School of Mechanical Engineering.

Today's world is frequently going through fossil energy shortage and environmental consequences brought by the over-emission of greenhouse gas from burning fossil fuels. Therefore, it is urgent now more than ever to discover or develop clean and sustainable power generation approaches. Among various approaches, photovoltaics and thermoelectrics have been more and more attentive both in academia and industry. Photovoltaic power generators can significantly decrease carbon dioxide emission by directly converting sunlight into electricity, and thermoelectric power generators can increase energy use efficiency by recycling waste heat into electricity. This research seeks to gain a better understanding of the mechanism that influences the energy conversion process in photovoltaic and thermoelectric materials and meanwhile use nano-engineering approaches to improve the performance of thermoelectric materials.

For photovoltaic nanomaterials, we have first made progress in simulations of electron-phonon coupling, which is a major mechanism for efficiency loss, in CdSe quantum dots. Time-domain non-adiabatic ab initio simulations have been performed to study the phonon-assisted hot electron relaxation dynamics in CdSe nanocrystals. It is found that

the shape of the nanocrystals has a strong impact on the electron decay dynamics. The electron-phonon coupling is generally stronger in elongated nanocrystal than in the spherical nanocrystal. The relaxation of hot electrons proceeds faster in the elongated nanocrystal than in the spherical nanocrystal, and it also shows stronger temperature dependence in the elongated nanocrystal. The hot electron decay rates calculated from non-adiabatic molecular dynamics show weaker temperature dependence than the T^{-1} trend in both elongated and spherical nanocrystals, which can be attributed to the thermal expansion effect.

We then performed experiments to synthesize and characterize semiconductor nanocrystals. Monodisperse CdSe, PbSe, and PbTe nanocrystals of various morphologies have been synthesized by using different combinations of surfactant and solvent in the refined phosphonic-acid-assisted organometallic method. XRD spectra have confirmed the formation of desired crystal phase and size. SEM and TEM images have confirmed the morphology and crystallinity. UV-visible absorption spectra show that the bandgap decreases with increasing crystal size. With collaborators, we have characterized the hot electron relaxation dynamics using transient absorption spectroscopy. The results show that the hot electron relaxation can result from both electron-phonon coupling and the Auger process

Raman spectroscopy has also been used to investigate the size, shape and temperature dependence of phonon vibrational modes, for the interest of Raman thermometry using NCs. For spherical CdSe NCs of diameters 2.8 nm, 3.6 nm, and 4.4 nm, the temperature sensitivities are -0.0131 cm^{-1}/K, -0.0171 cm^{-1}/K, and -0.0242 cm^{-1}/K, respectively. This trend indicates that as the diameter increases, the effect of increasing phonon

anharmonicity dominates over the effect of the decreasing thermal expansion coefficient. On the other hand, triangular NCs with a size of 4.2 nm and elongated NCs of a dimension of 4.6 nm by 14 nm show temperature sensitivities of -0.0182 cm^{-1}/K and -0.0176 cm^{-1}/K, respectively. This trend indicates that in non-spherical shape NCs, the effect of decreasing thermal expansion coefficient dominates over the effect of slightly increasing phonon anharmonicity.

For thermoelectric nanomaterials, both material synthesis and device fabrication have been conducted. For the material synthesis part, Bi_2Te_3-based nanocrystals have been made using both pyrolysis of organometallic method and ball milling method. Experimental parameters have been optimized to make impurity-free Bi_2Te_3 nanocrystals of various morphologies. Raman spectroscopy has been used to investigate the morphology dependence of phonon modes. The A_{1u} mode is invisible in bulk Bi_2Te_3, but becomes visible in Bi_2Te_3 nanocrystals no matter whether they are synthesized by wet-chemistry method or ball milling method. Furthermore, for wet-chemistry synthesized Bi_2Te_3 nanocrystals, the 2D nanostructure shows similar Raman features as those of few-quintuple-thick Bi_2Te_3 layers, while the 0D and 1D nanostructures show a blue-shifted A_{1g}^2 mode and a much stronger A_{1u} mode, which is the first report regarding the morphology impact on the Raman modes of Bi_2Te_3 nanocrystals.

We have also used ball milling and hot pressing to obtain nanostructured bulk and improve the figure of merit of Bi_2Te_3 based alloys. Nanostructured bulk pellets are fabricated by densifying nanocrystal powders into bulk using hot pressing method. Due to the increased phonon scattering at the grain boundaries introduced in nanostructured bulk process, significantly reduced thermal conductivities have been obtained on

nanostructured bulk Bi_2Te_3 pellet samples. It is also observed that thermal conductivity decreases with decreasing average grain size. Several post-fabrication treatments, like removing surface oxide layer by Ar plasma and improving crystallinity by thermal annealing, have been used to further improve the thermoelectric properties of the samples. Ion bombardment by Ar plasma is found to improve the contact between the metal electrodes and the material. Thermal annealing is found to not only increase the electrical conductivity but also the increase the Seebeck coefficient. The improved figure of merit at room temperature is around 1.23 on the p-type $Bi_{0.5}Sb_{1.5}Te_3$ sample and 0.32 on the n-type $Bi_2Te_{2.7}Se_{0.3}$ sample. The value from the p-type sample is close to the state-of-the-art value and still has room for improvement.

CHAPTER 1. INTRODUCTION

Molecular and bulk materials have exhibited distinct properties in optical, thermal, electrical, thermoelectric, photovoltaic, as well as magnetic applications. The size of nanomaterials lies in the intermediate regime between molecular and bulk scales. The study of nanoscale materials brings up a chance for scientists to study the evolution of those properties as size increases from molecule to bulk.

The size dependent properties of semiconductor nanomaterials mainly arise from the size dependent electronic structures when their size falls into the so-called strong confined region, Bohr Radius. Within the strong confined region, the continuous electronic energy bands in bulk materials break into discrete energy levels and the spacing between electronic levels as well as the bandgap increases with decreasing size. This is so called quantum confinement effect. By studying the size-dependent behavior of physical and chemical properties, people can gain a better understanding of the underlying mechanism, which will hence lead to advances in synthesizing materials with desired properties in more precise ways.

1.1 Photovoltaic Applications of Semiconductor Nanomaterials

In photovoltaic semiconductor materials, valance-band electrons can be excited into conduction band upon the absorption of photons with enough energy. These excited electrons are called hot electrons, and as a result of the broad bandwidth of the solar

radiation, electrons may end up in different energy states depending on the energies of the absorbed photons.

However, these hot electrons are in a metastable status and can eventually lose their excess energies to the ambient via a series of scattering events, with phonons, photons, holes, defects, and so on, among which electron-phonon interaction is of great importance. These energy loss processes compete strongly with the energy harvest process, and this is undesirable in the photovoltaic applications. As a matter of fact, such energy loss has been dominating over energy harvest and become a big limiting factor in further increasing the conversion efficiency of solar cell devices. It prevents the cost of using solar energy from being reduced. Therefore, to address this issue for possible solar efficiency improvement, the hot electron relaxation (decay) rate should be significantly reduced so that hot electrons can be extracted into the external circuit before decaying back to the valence band and making no contributions.[1-3]

Minimizing electron-phonon coupling is helpful in slowing down hot electron relaxation rate, so it is necessary to study phonon properties in these confined nanocrystals to gain a better understanding of energy-involved electron-phonon interactions.

With an energy band gap (1.73 eV) lying within the visible region of the solar spectrum, cadmium selenide (CdSe) is considered to be a promising substitute for the conventional silicon materials in photovoltaic industry. When the size reduces to a few nanometers, the band gap of CdSe nanocrystals (NCs) can be tuned through changing size [4] and surface chemistry [5, 6], or doping [7]. This makes it convenient to control absorption properties for potential solar cell applications. Lead selenide (PbSe), an IV-VI

group semiconductor, has exhibited similar size-tunable optical and electrical properties [8, 9]. Different from CdSe, whose bandgap is located in the visible range, PbSe has a much smaller energy bandgap (0.27eV), located in the infrared range. This small bandgap extends the absorption range to the infrared area and favors the multiple exciton generation process but makes PbSe-based solar cells less likely to provide high photovoltage output. Schottky solar cell devices based on PbSe nanocrystal films have achieved an energy conversion efficiency (ECE) of up to 3.6% [10], and nanocrystal sensitized solar cell devices using CdSe nanocrystal as the light absorber have reached an ECE of up to 4.44%[11].

Guyot-Sionnest et al.[12] have demonstrated the strong influence of surface ligands on the intraband electronic relaxation in CdSe NCs. Jaroz et al.[13] have showed in their work that photoconductivity of NC films can be increased by treating the as-deposited film with amines and sodium hydroxide, which can significantly increase the NC surface passivation and reduce the inter-NC spacing. Gur et al.[14] have found out sintering at appropriate temperatures could increase the solar cell efficiency. Koleilat et al.[10] have increased the efficiency of PbSe NC film based solar cell to 3.6% by replacing the long oleate ligands with a strongly bound bidentate linker, benzenedithiol.

Semiconductor NCs have also been chosen as substitutes for dyes in dye sensitized solar cells because of their size-tunable bandgap and relatively large absorption cross sections[15]. Although the efficiency of NC sensitized solar cell is still lower than the efficiency of traditional dye sensitized solar cell (11%), some progresses have been made in the past few years. By increasing the fraction of large TiO_2 particles and keeping the balance between the light scattering and surface area, Zhang et al. are able to obtain

efficiency as high as 4.92% in their CdSe/CdS co-sensitized solar cell device. Zheng and co-workers[11] have obtained a 4.44% efficiency in devices made through refined fabrication techniques.

Some experiments have shown that the electron-hole interaction, which is also called Auger process and usually proceeds faster than the electron-phonon interaction, can co-exist with and hence dominate over the electron-phonon interaction in the electron relaxation process in NCs [16]. Depending on the types of the materials, status of surface passivation, and types of surface ligands, the Auger process can be suppressed if electrons and holes are separated or if electrons and holes have similar density of states (DOS). For instance, with shallow hole-trapping surfactants attached to the NCs, the Auger process is dominating and the hot electron relaxation is very fast,[16-20] while with deep hole-trapping surfactants attached, the Auger process can be suppressed through an effective electron hole separation and leave the electron-phonon interaction dominating in the decay process.[16, 21]

With the knowledge of suppressing the relatively fast electron-hole coupling, the remaining step to reduce the electron decay rate is to further suppress the relatively slow electron-phonon interaction in materials via modifying the electronic properties of the materials. For bulk materials, it's hard to achieve this. However, making the bulk semiconductors into nanostructures, such as quantum dots and quantum rods, has shown the potential to slow down the electron-phonon interaction. According to the quantum confinement effect, when bulk materials are made into nano materials, their previously continuous energy bands will break into discrete energy levels, and the spacings between adjacent energy levels will increase as decreasing the size and exceed the energy of a

single phonon at some point, which will hence result in mismatch between electronic transition energy and phonon energy. As a result, hot electrons will need to couple with multiple phonons simultaneously to relax to lower levels. This higher order process is supposed to result in lower electron decay rates in nano materials, in contrast to bulk materials.[1, 22, 23] Such prediction has been observed in experiments.[16, 24] Furthermore, slowing down the electron relaxation rate is also desired for the possible multiple exciton generation process to be efficient,[3, 25-30] which in turn will also improve the overall conversion efficiency of solar cell devices.

Recognizing the importance and feasibility of slowing down the electron-phonon interaction in the application of photovoltaic materials, it is both fundamentally and practically crucial to first understand how the electron-phonon relaxation is affected by a variety of factors, such as material, temperature, nanoparticle size and shape, surface terminations, surfactants, etc.[31] Progresses have been made in both experiments and simulations.

For instance, Guyot-Sionnest et al.,[16] have investigated the influence of capping ligands and observed a 200ps long decay curve on CdSe NCs capped with pyridine, which is orders of magnitude longer than that observed in bulk CdSe. Yu et al.[32] have found that the intraband energy relaxation is 8 times faster in the thin CdSe QRs than the thick ones. Mohamed et al.[33] have shown that electrons of higher energy states decay faster in the CdSe QRs than the QDs. In addition to the experimental progresses, a non-adiabatic molecular dynamics approach has been developed[34, 35] to simulate the hot electron relaxation process in NCs,[36-38] and this approach has been used to investigate

the temperature dependence of hot carrier relaxation in PbSe and CdSe NCs.[39, 40] It's also found that the hot electron relaxation time decreases with increasing temperature, but the dependence deviates from the classical T^{-1} trend due to the thermal expansion effect.

Raman spectroscopy has been widely used to study the phonon vibrations in CdSe NCs by virtue of its sensitivity to local atomic arrangement and lattice vibration. The impact of nanocrystal shape and size, capping ligand, excitation wavelength, and matrix on phonon modes in CdSe nanocrystals has been intensively studied using Raman spectroscopy [6, 41-53], in which phonon properties can be exacted from the frequency and bandwidth of the Raman modes, and the intensity ratio of the LO mode to the 2LO mode [44-46, 50-52].

For instance, Tanaka et al. have found that the LO phonon peak shifts to lower frequencies and the bandwidth broadens with decreasing NC size or increasing temperature[54]. Meulenberg et al. have shown that the ZnS-shell-induced LO phonon shift is larger for smaller dots than for larger dots because of the larger compressive stress resulting from the larger mismatch between core and shell for smaller dots[55]. Kusch et al. have found that higher-order phonon processes are enhanced with decreasing NC size[56]. Tanaka ea al have studied CdSe microcrystals embedded in a germanate glass matrix and found the frequency of the peak decreases and the bandwidth broadens with decreasing size [42]. It's also found that surface tension, resulted from the lattice mismatch, can cause the frequency and bandwidth to change, which can be seen in typical core/shell QDs and QDs embedded in glass matrices [42, 43, 57]. In the work of Dzhagan et al., LO phonon peak of two kinds of CdSe/ZnS core/shell QDs is found to

shift to opposite sides of the LO phonon peak of the uncoated CdSe QDs due to different intermixing rates of core and shell materials [57]. Meulenberg's work has shown that a ZnS shell can induce a much larger compressive stress on a smaller dot than a larger dot, which can be attributed to the larger mismatch in the case of the smaller dot [55]. These studies have contributed to unveil the underlying mechanisms affecting the phonon vibrational behavior in CdSe NCs.

Despite all the progresses, it is also found that no systematic efforts have been devoted to investigating the influence of the CdSe QR length on the hot electron relaxation in either simulations or experiments, which hinders a fundamental understanding of the structure-property relationship.

1.2 Microscale Thermometry Applications of CdSe Nanomaterials

In the field of microscale temperature probing, Raman spectroscopy has also been widely used due to its high spatial resolution and feasibility in sample preparation.

Tanaka et al have studied the phonon modes in the embedded CdSe microcrystals below room temperature [42]. Dzhagan et al. have investigated the phonon behavior in the core/shell CdSe QDs below room temperature. Song et al. find that radial breathing mode corresponding to larger diameter has higher temperature sensitivity in single-walled carbon nanotubes[58]. The work of Calizo et al. shows that there's no significant difference in temperature sensitivity between single-layer and bi-layer graphenes[59]. In nanomaterials, crystal geometry poses a significant influence on Raman properties. However, little work has been done to study the geometry impact due to the ambiguities caused by non-monodispersity of CdSe NCs.

1.3 Thermoelectric Applications of Bi_2Te_3-Based Nanomaterials

Thermoelectric effects refer to phenomena that a temperature difference or gradient can generate an electrical potential difference or an electrical current can generate a temperature difference. Although thermoelectric effects can be observed in most materials, a good candidate material for thermoelectric applications should have a high figure of merit value. Compared with insulators, semiconductors have relatively high and tunable electrical conductivity. Compared with metals, semiconductors have relatively high Seebeck coefficient. The combination of moderate electrical conductivity and Seebeck coefficient makes semiconductor materials promising materials for thermoelectric applications. Bismuth telluride and its alloys, well known for that they possess the highest figure of merit at room temperature, are widely used for solid-state cooling devices[60]. Bulk Bi_2Te_3-based alloys possess a ZT value close to 1 [61]. However, in order for TE power generation to become competitive to other power generation approaches, a ZT value of 3-4 is required [62].

Theoretical studies show that low-dimensional nanomaterials can have a much higher figure of merit compared with their bulk counterparts[63, 64] as a result of decreased thermal conductivities. Zhao et al.[65] have shown that ZT value of Bi_2Te_3 nanocomposites can be enhanced by introducing non-uniform micro structures even without changing chemical compositions. Mavrokefalos et al.[66] show that better control over chemical composition is necessary to improve the ZT of the electrodeposited nanowires. Theoretical studies done by Qiu et al.[67] show that Bi_2Te_3 nanowires of a diameter smaller than 10nm possess a higher ZT value than their bulk counterparts. Hicks et al. show that the ZT value of Bi_2Te_3 quantum well may be 9 times higher than the bulk

value [64] and the ZT value of 1D Bi_2Te_3 nanowire can be increased to ~14 from the bulk value [63].

Raman spectroscopy has been used to detect the lattice vibration of Bi_2Te_3 materials. With Raman spectroscopy, the influence of thickness in few-quintuple Bi_2Te_3 layers and chemical stoichiometry in Bi_2Te_3 films has been studied [68-71]. To our best knowledge, little work has been done to study the phonon modes in Bi_2Te_3 nanorods and small Bi_2Te_3 nanoparticles whose sizes are within the strong quantum confinement region.

1.4 Progress in Wet-Chemistry Synthesis of Semiconductor Nanomaterials

For photovoltaic applications, a large part of the contribution to the external quantum efficiency (ECE) improvement can be attributed to the progress in NC synthesis and modification. So far, II-IV and IV-VI NCs can be synthesized via organometallic[4, 72, 73], hydrothermal[74] [75], ultrasonic [76], and microwave irradiation assisted route [8, 77]. For example, high-crystallinity semiconductor NCs can be synthesized with high yield since Murray et al.[4] have developed a new synthesis method by combining hot-injection with pyrolysis of organometallic compound. Deng et al.[78] have synthesized high-crystallinity zinc-blende CdSe NCs with a non-TOP route. Yu et al.[15] have developed an empirical equation that directly relates optical absorption maximum with the size of NCs. Norris et al.[79] have studied the size-dependent optical properties of CdSe NCs. Bullen et al.[80] systematically investigate the nucleation and growth mechanisms of CdSe NCs in octadecene, which is a commonly used non-coordinating solvent in the synthesis.

Among the methods mentioned above, the fast-injection organometallic route is popularly used to prepare monodisperse CdSe NCs. By employing a hot injection

technique at a high temperature (~300 ℃), the organometallic route can result in a narrow size distribution through a fast nucleation process. Additionally, because of the relatively high reaction temperature, organometallic route usually produce samples of better crystallinity in a far shorter period than samples prepared by other methods. Solvents used in the fabrication have strong influence on the NCs' properties. As a coordinating solvent, TOP/TOPO also acts as the surfactant, which is used to stabilize and passivate the NCs. Although coordinating solvent can favor the formation of high-crystallinity and well-shaped NCs [81, 82], non-coordinating solvents, like octadecene, still have some advantages over coordinating solvent [53]. First, when octadecene is used, the concentration of the surfactants can be easily tuned in order to optimize the reaction rate. Second, octadecene is less toxic and easy to measure and mix with other chemicals. In our work, a combination of octadecene and TOPO is used as the solvent in order to take advantage of both. Also, Wang et al. [83] have shown in their work that syntheses using longer chain phosphonic acids tend to produce spherical CdSe NCs and impose more control over the reaction rate.

For thermoelectric applications, tremendous efforts have also been put into the preparation of nanostructured bismuth telluride (Bi_2Te_3). They have been synthesized via methods, like co-precipitation of bismuth and tellurium oxides[84], reduction of metal-organo complexes[85], surfactant-controlled hydrothermal (solvothermal) methods[86-89], and electric-field-assisted deposition[90, 91]. Various shapes of Bi_2Te_3 NCs have been synthesized in experiments, including nanorods[92], random[93] and arrayed[90] nanowires, nanoparticles[87, 91, 94, 95], nanosheets[87, 93], nanosheet-rods[93],

nanotubes[86, 88] and nanofoils[96], with the development of various experimental techniques.

Among all these methods mentioned above, the hydrothermal and electrodeposition routes have attracted the most attention because of their easy operations and low-energy cost. In the hydrothermal process, the reaction temperature, time, concentration, surfactants and reductants all have vital influence on the as-synthesized nanocrystal properties, like microstructure, shape and size, while in the electrodeposition process, the electric field, reaction time, substrate and template all play an important role. Due to the application of high pressure, hydrothermal (solvothermal) approaches normally result in overgrown Bi_2Te_3 nanocrystals [87].

However, with the expectation of utilizing the quantum confinement effect, smaller Bi_2Te_3 nanoparticles (< 10nm) with better size distributions are more desirable, which have not been realized in either hydrothermal or electrodeposition method. The smallest Bi_2Te_3 nanoparticles that could be achieved in the hydrothermal technique are ~30nm with a broad size distribution.

So far, the synthesis of pure-phase Bi_2Te_3 nanoparticles smaller than 10 nm still remains a challenge due to the high reactivity between bismuth and tellurium salts. A recent work by Purkayastha et al.[97] has used an innovative synthetic procedure, which results in Bi_2Te_3 nanoparticles as small as 5nm with relatively narrow distributions. This experiment is carried out at room temperature and employs a microemulsion method to promote the nucleation and growth of Bi_2Te_3 nanoparticles. The resulted nanoparticles are protected by thioglycolic acid from agglomeration and surface oxidization. The high Seebeck coefficient (-107 μV/K)[97] measured from the sample exhibits their potential as

a thermoelectric material with high figure of merit. However the XRD results show the existence of sulfur-related impurities. Scheele et al. [98] have used a two-step reduction method to produce nanoparticles of 7 nm, but there is still a trace of impurities.

1.5 Objectives and Scope of Thesis

This thesis has two objectives. The first objective is to gain a better understanding about the phonon vibrations and electron-phonon coupling in photovoltaic materials through both simulations and experiments. For simulations, time-domain density functional theory is used to study phonon-assisted hot electron relaxation dynamics. For experiments, semiconductor nanocrystals are synthesized using pyrolysis of organometallic compounds and characterized using various methods, Raman spectroscopy, XRD, SEM, TEM, UV-Vis absorption spectroscopy and IR spectroscopy. The second objective is to develop high-ZT materials for high-performance thermoelectric devices through nanostructured bulk approach. For material development, nanocrystals are prepared using both pyrolysis of organometallic compounds and ball milling. For device fabrication, nanostructured bulk is fabricated by hot pressing nanocrystal powders.

The thesis is organized in the following way. Chapter 1 is dedicated to giving an introduction of research motivation, research background, major progresses and challenges in the research. Chapter 2 and 3 are dedicated to studies regarding photovoltaics and will demonstrate the research progress and findings that I have made in photovoltaics area. Chapter 4 and 5 are dedicated to studies regarding thermoelectrics and will demonstrate the research progress and findings that I have made in thermoelectric area. Chapter 6 is dedicated to a brief summary of important achievement during my PhD

study as well as suggestions for future research directions. Details about the methods and equipment used for experiments and simulations will be given in each individual chapter.

Chapter 2 focuses on the simulation work that has been done to study the hot electron decay dynamics in CdSe nanocrystals. The real-time ab initio simulation is performed by implementing trajectory surface hopping into time-domain Kohn-Sham theory. Two types of CdSe nanocrystals are studied, spherical NC and elongated NC. The electronic DOS and band structure are first calculated. Then the band gap is calculated from which the optical absorption spectra are derived. The electron-phonon coupling strength spectra are then obtained by taking the Fourier transforms of the time-domain electronic energy levels. The hot electron decay rates are calculated using non-adiabatic molecular dynamics and their dependencies on temperature and shape are analyzed.

Chapter 3 focuses on experimental work inspired by the simulation findings and performed to synthesize and characterize semiconductor nanocrystals for photovoltaic applications. For the synthesis part, monodisperse CdSe, PbSe, and PbTe nanocrystals of various morphologies are synthesized using the refined phosphonic-acid-assisted organometallic method. For the characterization part, XRD spectra are used to characterize the crystal phase and size. SEM and TEM images are used to characterize the crystal morphology and crystallinity. UV-visible absorption spectra are used to monitor the crystal growth. Raman spectroscopy is used to study the size, shape and temperature dependence of phonon vibrational modes in CdSe nanocrystals. Besides photovoltaic applications, with the understanding of temperature-dependent phonon properties, knowledge acquired can also be used to improve the application of Raman spectroscopy in microscale thermometry.

For thermoelectric applications, both material synthesis and device fabrication have been conducted.

Chapter 4 focuses on material synthesis and characterization for thermoelectric applications. For the material synthesis part, Bi_2Te_3-based nanocrystals have been made using both pyrolysis of organometallic method and ball milling method. Experimental parameters have been optimized to make impurity-free Bi_2Te_3 nanocrystals of various morphologies. Raman spectroscopy has also been used to investigate the morphology dependence of phonon modes. The A_{1u} mode is invisible in bulk Bi_2Te_3, but becomes visible in Bi_2Te_3 nanocrystals no matter whether they are synthesized by wet-chemistry method or ball milling method. Furthermore, for wet-chemistry synthesized Bi_2Te_3 nanocrystals, the 2D nanostructure shows similar Raman features as those of few-quintuple-thick Bi_2Te_3 layers, while the 0D and 1D nanostructures show a blue-shifted A_{1g}^2 mode and a much stronger A_{1u} mode, which is the first report regarding the morphology impact on the Raman modes of Bi_2Te_3 nanocrystals.

Chapter 5 focuses on nanostructured bulk fabrication and characterization for thermoelectric applications. For the thermoelectric device fabrication, nanostructured bulk approach has been adopted to improve the figure of merit of Bi_2Te_3 based alloys. Nanostructured bulk pellets are fabricated by densifying nanocrystal powders into bulk using hot pressing method. Due to the increased phonon scattering at the grain boundaries introduced in nanostructured bulk process, significantly reduced thermal conductivities have been observed in nanostructured bulk Bi_2Te_3 samples. It is also observed that thermal conductivity decreases with decreasing average grain size. Several post-fabrication treatments, like removal of surface oxide layer by Ar plasma and thermal

annealing, have been used to further improve the thermoelectric properties of the samples. Thermal annealing is found to not only increase the electrical conductivity but also the increase the Seebeck coefficient. The improved room-temperature figure of merit on p-type $Bi_{0.5}Sb_{1.5}Te_3$ is around 1.23, which is close to the state of the art value and still has room for improvement.

CHAPTER 2. PHOTOVOLTAICS -- PHONON ASSISTED HOT ELECTRON RELAXATION IN CDSE NANOCRYSTALS

For this part of the work, we have performed time-domain non-adiabatic molecular dynamics simulations on CdSe spherical quantum dot (QD) and elongated quantum dot (EQD) in order to gain a clear picture of how the length and temperature affects the phonon-assisted hot electron relaxation dynamics.

2.1 Simulation Method and Details

The time-domain non-adiabatic molecular dynamics simulation of the electron-phonon relaxation dynamics is realized by implementing the fewest switching surface hopping technique [34, 99, 100] in the time-domain Kohn-Sham theory [101]. Details of this method can be found in the reference [38], and here we only outline the procedure.

The electron density is written in the Kohn-Sham (KS) representation as[101],

$$\rho(x,t) = \sum_{P=1}^{Ne} |\varphi_P(x,t)|^2, \tag{2.1}$$

where *Ne* is the number of electrons and $\varphi_P(x,t)$ is single-electron KS orbital. Applying the time-dependent variational principle to the expectation value of the KS density functional will lead to the system of coupled equations of motion for the single-particle KS orbitals[101],

$$i\hbar \frac{\partial \varphi_P(x,t)}{\partial t} = H\big(\varphi(x,t)\big)\varphi_P(x,t), P = 1, \dots, Ne. \tag{2.2}$$

The time-dependent KS orbitals can be expanded in terms of adiabatic KS orbitals,

$$\varphi_P(x,t) = \sum_{P=1}^{Ne} c_{pk}(t)|\tilde{\varphi}_k(x;R) >, \tag{2.3}$$

where R is the ion configuration. After plugging Eq. (2.3) into Equation (2.2), the latter transforms into the equation of motion for the expansion coefficients c_{pk},

$$i\hbar \frac{\partial c_{Pk}(x,t)}{\partial t} = \sum_{m=1}^{Ne} c_{pm}(t)\left(\varepsilon_m \delta_{km} + \boldsymbol{d_{km}} \cdot \dot{\boldsymbol{R}}\right), \tag{2.4}$$

where $\boldsymbol{d_{km}}$ is the electron-phonon coupling term defined as,

$$\boldsymbol{d_{km}} = -i\hbar < \tilde{\varphi}_k(x;R)|\nabla_R|\tilde{\varphi}_m(x;R). \tag{2.5}$$

The non-adiabatic coupling factor is given by [102]

$$NA = \boldsymbol{d_{km}} \cdot \dot{\boldsymbol{R}} = -i\hbar < \tilde{\varphi}_k(x;R)|\nabla_R|\tilde{\varphi}_m(x;R) >\cdot \dot{\boldsymbol{R}}$$

$$NA = -i\hbar < \tilde{\varphi}_k(x;R)\left|\frac{\partial}{\partial t}\right|\tilde{\varphi}_m(x;R) >. \tag{2.6}$$

Here the adiabatic KS orbitals $\tilde{\varphi}_m(x;R)$ are calculated by solving the time-independent KS equations, as implemented[34] in the Vienna Ab initio Simulation Package (VASP)[103]. Using FSSH, the probability of a transition from a given state *k* to another state *m* within the time interval *dt* is given by

$$dP_{km} = \frac{b_{km}}{a_{kk}} dt, \tag{2.7}$$

where

$$b_{km} = -2R_e\left(a_{km}^* \boldsymbol{d_{km}} \cdot \dot{\boldsymbol{R}}\right), a_{km} = c_m^* c_k, \tag{2.8}$$

Here, c_m and c_k are the coefficients evolving according to Eq. (2.4). As explained in references[99, 104], FSSH gives detailed balance between the upward and downward transitions. From the above equations, the time-dependent electron population in each electronic orbital can be determined. Note that our approach captures electron-phonon relaxation channel, while the electron-hole interactions are not included.

The geometry optimization, electronic structure calculation, and molecular dynamics (MD) are performed with VASP code using converged plane-wave basis density functional theory (DFT)[103] in simulation cells periodically repeated in three dimensions. Instead of the simultaneous integration of electronic and ionic equations of motion adopted in Car-Parrinello method, this approach performs an exact evaluation of the instantaneous electronic ground state at each MD-step using an efficient Pulay mixing and efficient matrix diagonalization schemes[103]. In our simulations, the initial structures of the $Cd_{33}Se_{33}$ QD and $Cd_{54}Se_{54}$ EQD were generated from bulk wurtzite-structured CdSe (a = 4.3 Å, c = 7.02 Å). Compared with the QD, the EQD is of the same dimension in radial direction, but elongated in the axial direction. In order to prevent spurious interactions between periodic images of the QDs and EQDs, the cells were constructed to have at least 20 Å of vacuum between neighboring QDs and EQDs. The PW91 density functional [105] and Vanderbilt ultrasoft pseudopotentials[106] were used throughout the study. The KS orbitals were expanded using the plane wave basis set with the energy cutoff of 12.34 Ry (167.9 eV). Higher cutoff energy was also tested and no significant changes were seen in the resulted configuration and electronic structure. For the CdSe QD and EQD, only Γ point calculations are necessary.

The structure was first fully optimized at 0 K and then heated up to different temperatures by MD. Then a 4ps microcanonical trajectory was generated at each temperature. The electronic and ionic time steps are set to be 10^{-3} and 1 fs, respectively. The nuclear trajectories from this microcanonical MD were then used to sample 500 initial conditions to create ensemble averages for the non-adiabatic molecular dynamics.

2.2 Results and Discussions

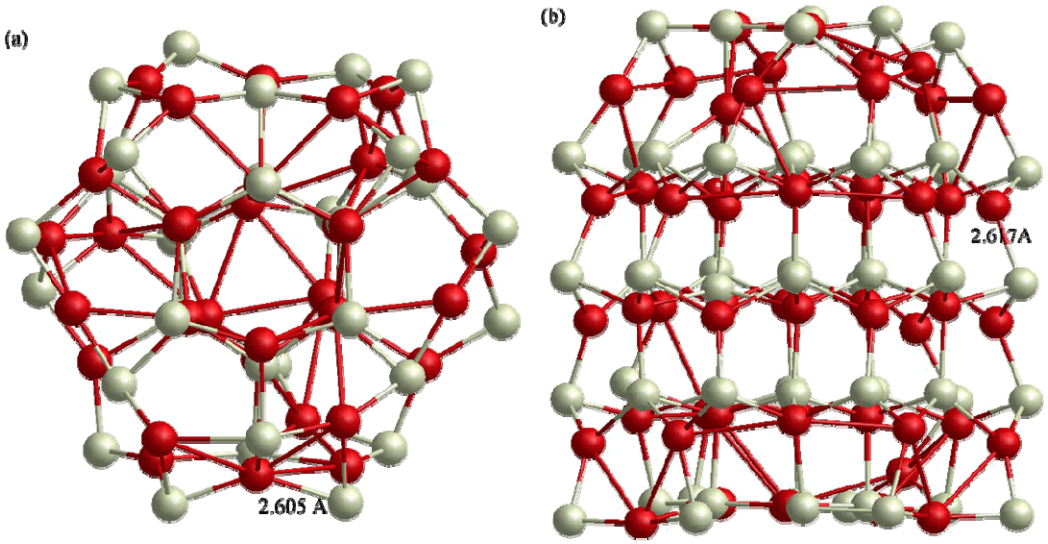

Figure 2.1. Optimized structures. (a) $Cd_{33}Se_{33}$ QD, (b) $Cd_{54}Se_{54}$ EQD.

The initial structures of the QD and EQD were first optimized at 0 K. During the optimization, Cd atoms tend to move inward to minimize the energy and reconstructions occurred at or near the surface, however the bulk crystal structures were found to be well preserved in both QD and EQD, as is shown in Figure 2.1. The optimized QD is ~1.24 nm in diameter and the optimized EQD is ~1.24 nm in diameter and ~1.57 nm in length (c axis). Some lengths of typical Cd-Se bonds are shown in Fig. 2.1. For the QD, the average Cd-Se bond length is 2.663 Å with a spread between 2.491 Å and 2.927 Å, while for the EQD, the average Cd-Se bond length is 2.668 Å with a spread between 2.489 Å and 2.964 Å.

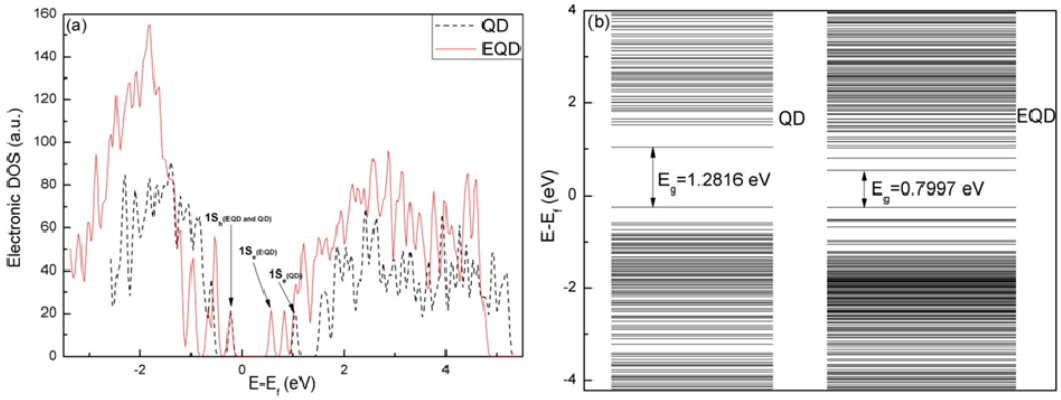

Figure 2.2. (a) Electronic DOS, (b) Electronic structures of the $Cd_{33}Se_{33}$ QD and $Cd_{54}Se_{54}$ EQD.

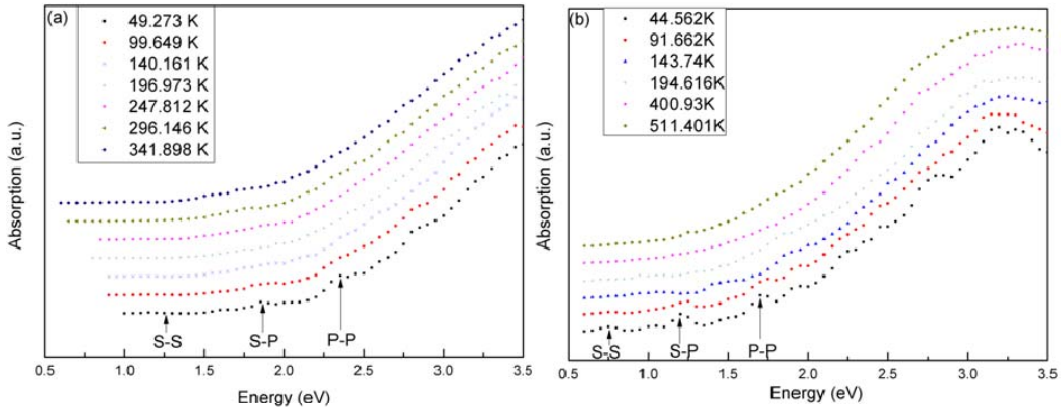

Figure 2.3. Absorption spectra. (a) QD, (b) EQD.

The electronic energy levels and DOS of the CdSe QD and EQD optimized at 0K are shown in Fig. 2.2. The first peak in the conduction band can be attributed to the 1s electron state ($1S_e$) and the first peak in the valance band is the 1s hole state ($1S_h$). In both cases of QD and EQD, hole states are denser than electron states. This agrees well with the effective mass approximation, in which heavier effective mass is used for holes than electrons ($m_h / m_e \approx 6$) [107]. The band gap is estimated by taking the energy difference between the $1S_e$ and $1S_h$ states. The obtained value here is ~1.3 eV for the QD and ~0.8 eV for the EQD, both lower than experimental values, which is commonly seen in typical DFT-based simulations [36-38, 108]. However, the under-predicted band gap will not

significantly affect our calculations of hot electron relaxation since it occurs within the conduction band, and the conduction band curves are expected to be well predicted.

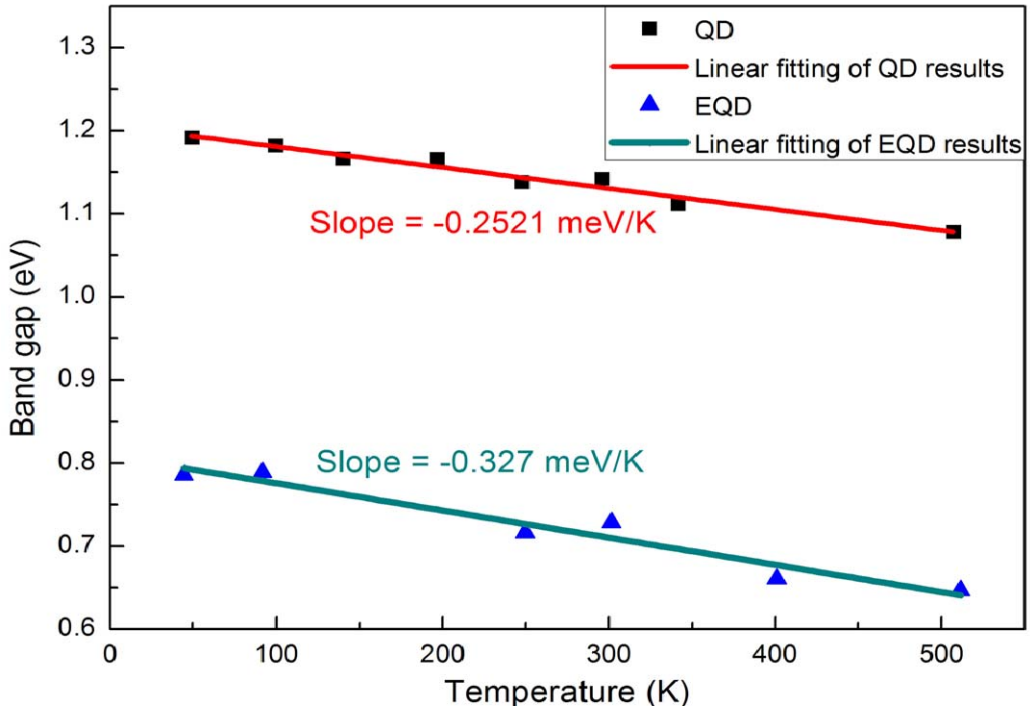

Figure 2.4. Band gap as a function of temperature for the QD and EQD.

Previous experiments show that the band gap of CdSe quantum rod whose size is within the strong confinement regime decreases as their length increases[109]. In our case, the EQD and QD together can be viewed as quantum rods with the same diameter but different lengths. The diameter (~1.24 nm) of both is much smaller than their exciton Bohr radius (~5.6 nm for bulk CdSe), and therefore the NCs are within the strong quantum confinement regime. This fact can explain why in our simulation the shorter quantum rod, i.e. QD, shows a noticeably wider band gap than the longer quantum rod, i.e. EQD, shown in Fig. 2.2.

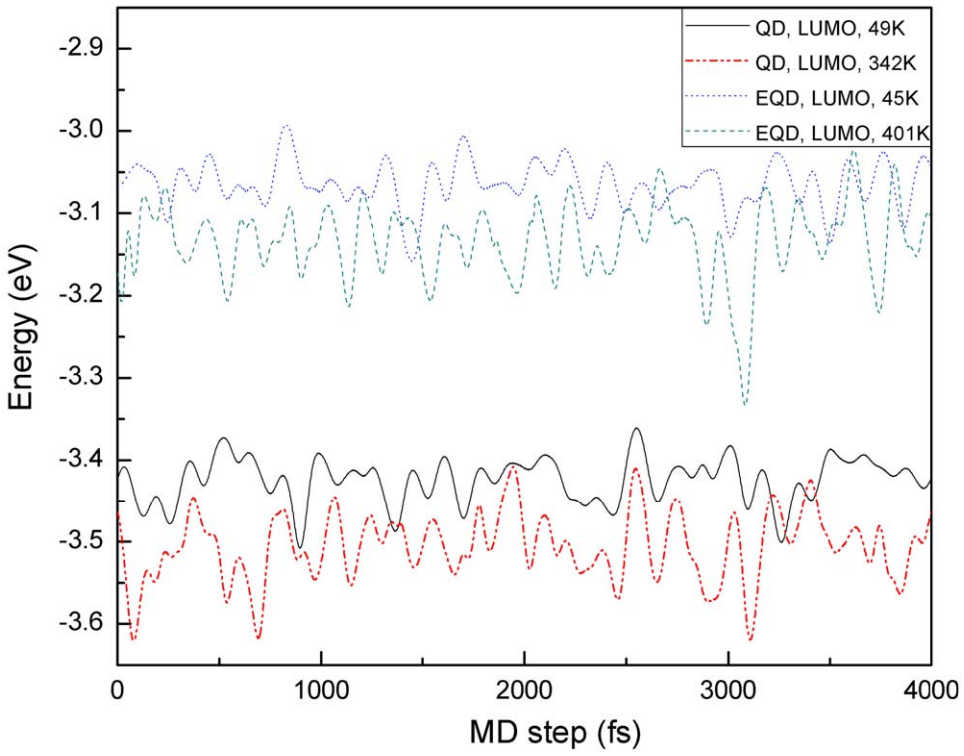

Figure 2.5. Time evolution of the LUMO energy for the QD and EQD at high and low temperatures.

The absorption spectra for the CdSe QD and EQD were calculated by summing over individual transitions across the electronic band gap[39], and the results are shown in Fig. 2.3. According to the DOS, the $1S_e$-$1S_h$, $1S_e$-$1P_h$ ($1P_e$-$1S_h$), and $1P_e$-$1P_h$ electronic transitions correspond to the absorption maxima at around 1.25 eV, 1.85 eV and 2.35 eV for the QD and 0.75 eV, 1.2 eV and 1.7 eV for the EQD. Compared with the QD, the absorption peaks in the EQD occur at lower energies, which is consistent with the fact that the electronic energy levels in the EQD are denser than in the QD. At higher temperatures, the absorption peaks are broadened because more phonons are generated and coupled to the photon absorption process. In addition, as temperature increases, the absorption peaks shift to the red side, indicating that the energy band gap probably should have negative temperature dependence for both QD and EQD.

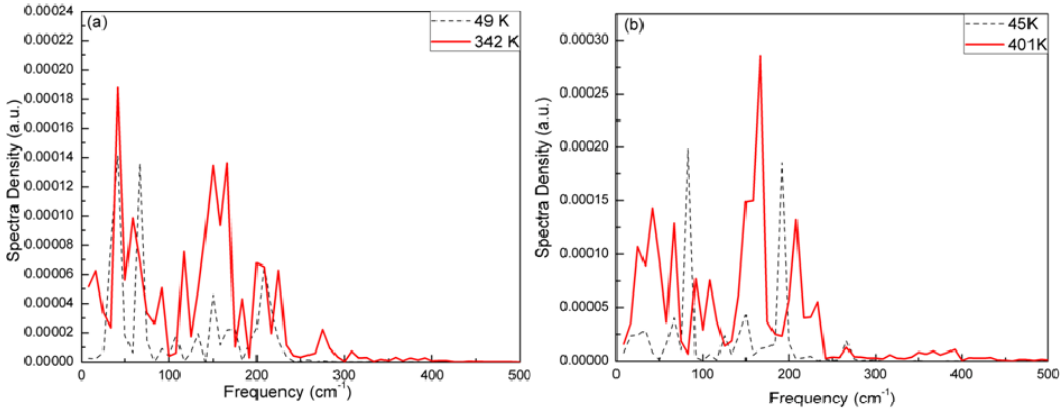

Figure 2.6. Fourier transforms of the LUMO energies. (a) QD, (b) EQD.

The temperature dependence of the band gap of the CdSe QD and EQD is shown in Fig. 2.4. These band gap values were calculated by averaging the energy differences between the lowest unoccupied molecular orbitals (LUMO) and highest occupied molecular orbitals (HOMO) over the MD trajectory at the specified temperature. The result can be fitted linearly with slopes of -0.2521 meV/K and -0.3824 meV/K for the QD and EQD, respectively. The negative temperature dependence of the band gap for both QD and EQD agrees well with the experiments [110-112]. It is also noticed that the band gap of the smaller quantum dot (QD) shows a weaker temperature dependence than that of the larger quantum dot (EQD), and similar trend was also observed in experiments by other researchers[113, 114]. Proposed by Olkhovet et al[113], the temperature dependence of the NC band gap is determined by four factors: dilation of the lattice, thermal expansion of the envelope function, mechanical strain and electron-phonon coupling, among which electron-phonon coupling makes the most dominant contribution. The electron-phonon coupling consists of intraband and interband coupling. The intraband coupling leads to negative temperature dependence, while the interband part gives a positive dependence.

Since the intraband energy differences for CdSe NCs do not approach the energy gap of bulk CdSe, the intraband coupling contributions are much larger than the interband contributions, and therefore the overall temperature dependence of the band gap is negative[113]. Furthermore, in CdSe NCs, the temperature dependence of ΔE contributed by the intraband part can be approximately related to the electron-phonon coupling strength S, $\Delta E/\Delta T \sim -S$[113]. According to our calculation, which will be shown later in Fig. 2.9, the intraband electron-phonon coupling is slightly stronger in the CdSe EQD than the CdSe QD, which can qualitatively explain the slighter stronger temperature dependence of the band gap in the EQD.

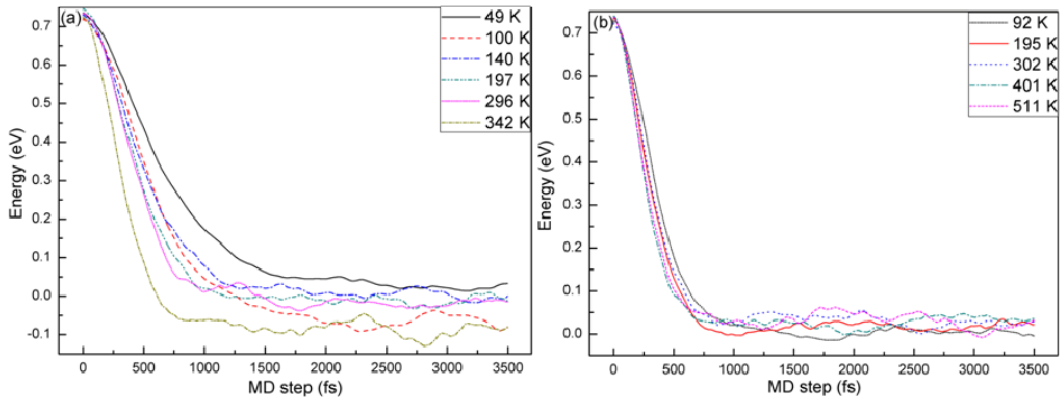

Figure 2.7. Average electron energy decay at different temperatures. (a) QD, (b) EQD.

In MD, temperature is evaluated based on the kinetic energy average over the MD trajectory. The time evolutions of the LUMO in both QD and EQD at low and high temperatures are shown in Fig. 2.5. The energy fluctuations are more significant at high temperature than low temperature for both QD and EQD. The LUMO values for the QD and EQD at various temperatures were obtained by averaging the LUMO values over the

MD trajectory (4000 fs). As temperature increases, the average LUMO value decreases and therefore decreases the band gap value.

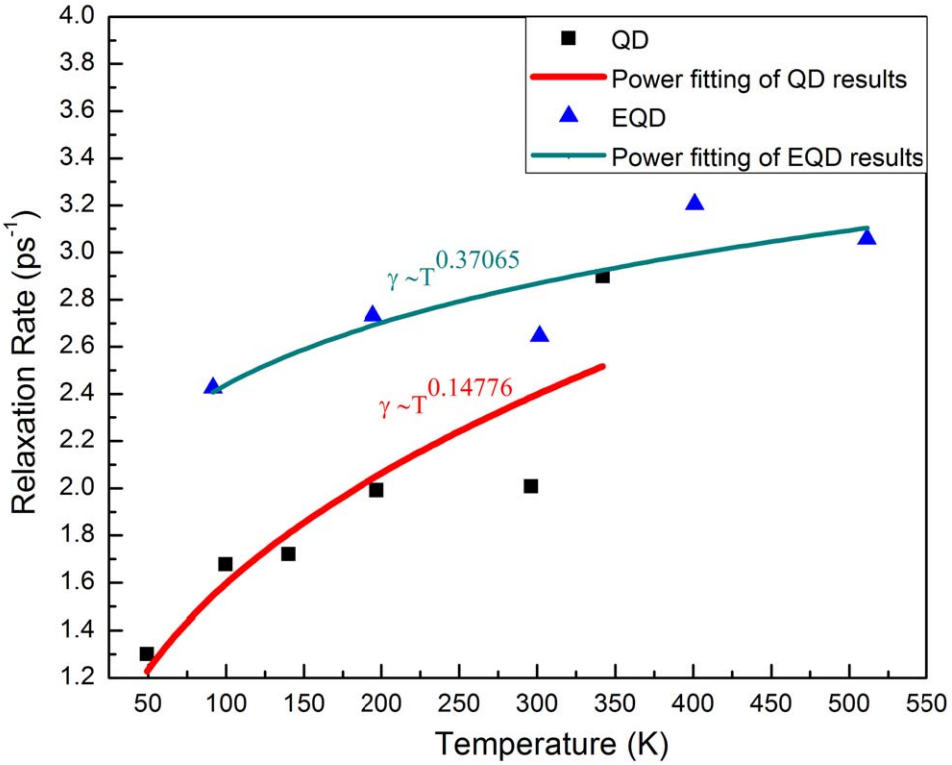

Figure 2.8. Hot electron relaxation rate as a function of temperature for the QD and EQD.

The phonon modes that can effectively couple to electron relaxation were investigated by taking the Fourier transforms of the time-dependent LUMO energies. The coupling strength spectra at different temperatures are plotted as a function of phonon frequencies in Fig. 2.6. As seen, temperature affects the electron-phonon coupling in two ways. First, at higher temperatures, the coupling spectra are broadened, indicating that more phonon modes are excited and coupled to electrons, which can be attributed to stronger anharmonic effect at higher temperatures. Second, at higher temperatures, high-frequency tails show up in the spectra, indicating that higher-frequency phonons are excited and

coupled to hot electrons. Furthermore, spectral densities are larger and more high-frequency vibrational modes are involved for the EQD than for the QD, indicating stronger phonon-electron non-adiabatic coupling in the CdSe EQD.

In this part, electrons were first excited to initial energy states at ~0.75 eV above the LUMO and then were allowed to relax from the non-equilibrium states to the LUMO. The driving force is electron density perturbation induced by lattice vibrations. Within this energy range, only transitions with largest optical activities were chosen as the initial conditions. The result of the time-dependent relaxation is shown in Fig. 2.7. For each temperature, a 3.5 ps decay trajectory is plotted, and the zero energy is set at the corresponding average LUMO value. A typical decay curve is composed of two parts, including a short-period Gaussian and thereafter an exponential component, similar to the previous result[36]. In the CdSe QD, electron energies will decay back to zero at the end of the 3.5 ps trajectories when temperature is higher than 50 K. At 342 K, electron energies can sometimes even fall below zero, which can be rationalized by taking into account the significant energy fluctuation at high temperatures. In the case of EQD, most electrons relax back to the LUMO at the end of the trajectories for a wide range of temperatures. The temperature-dependent hot electron decay rate can be easily calculated. In both QD and EQD, hot electrons decay faster at higher temperatures.

In order to gain a deeper understanding of the underlying relaxation mechanism, the decay rates at different temperatures were extracted from the decay curves, as shown in Fig. 2.8. The decay time here is defined as the time that electrons need in order to decay to the energy equal to 1/e of their initial energy, and the decay rate is defined as the inverse of the decay time with a unit of ps^{-1}. It can be seen in Fig. 2.8 that hot electrons

generally decay faster in the EQD than the QD. As mentioned in Section III.B, the stronger electron-phonon coupling leads to the higher relaxation rate for hot electrons in the EQD. Phonon-assisted electron relaxation can occur via both slow multi-phonon and fast resonant-energy-phonon processes, depending on the DOS[38].

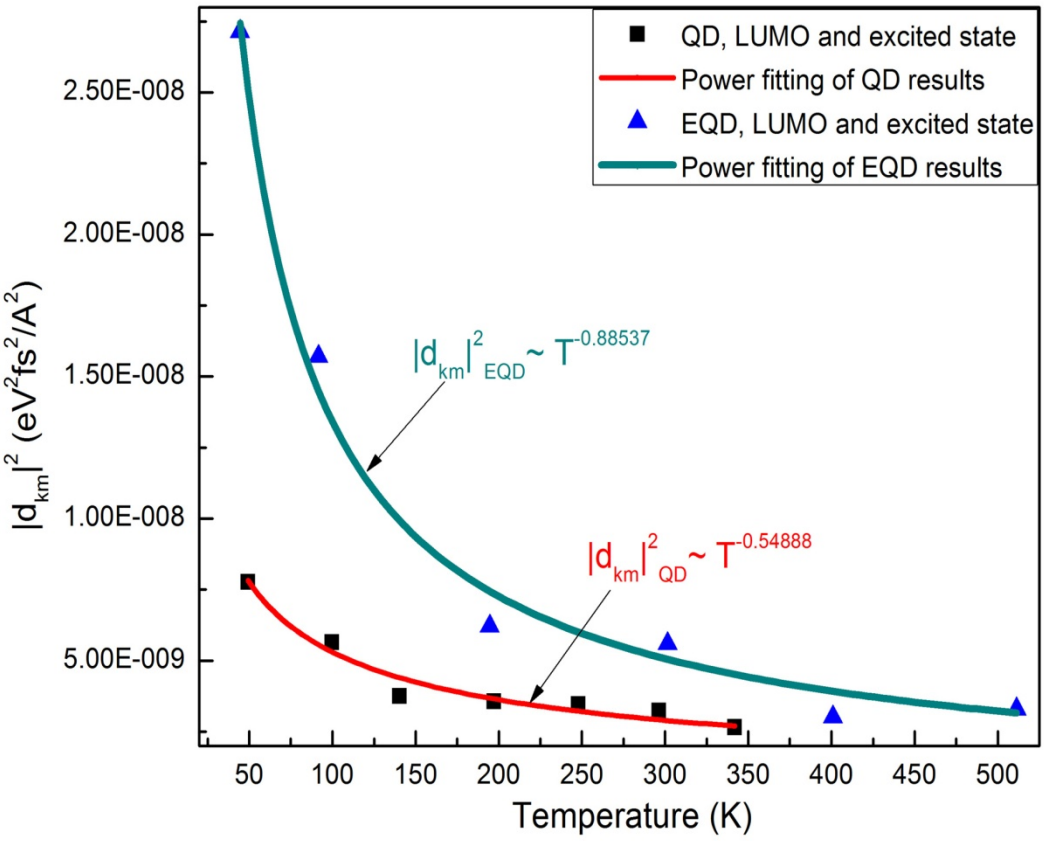

Figure 2.9. Temperature dependence of $| d_{km} |^2$ for the QD and EQD.

In Fig. 2.2, the electron DOS in the QD is different from that in the EQD in two ways. First, the 1S electron state in the QD is well separated from the rest of the CB, while the 1S electron state in the EQD has some overlap with the rest of the CB. Second, in the region well above the LUMO, electron states are denser in the EQD than in the QD. The non-adiabatic coupling defined in Eq. (2.6) can be rewritten as

$$NA = -i\hbar \frac{<\tilde{\varphi}_k|\nabla_R H|\tilde{\varphi}_m>}{E_m - E_k} \cdot \dot{\boldsymbol{R}}. \qquad (2.9)$$

According to Fermi's Golden Rule, the decay rate is proportional to $|NA|^2$ and thus inversely proportional to the square of the energy difference between transition states, which is (E_m - E_k) in Eq. (2.9). Giving the denser energy states in the EQD, the non-adiabatic coupling should be stronger in the EQD and thus the hot electron relaxation rate should be higher in the EQD.

Based on the theoretical model proposed in our previous work[39], the temperature dependence of the hot carrier relaxation rate could be simply written as,

$$\gamma \sim |NA|^2 \sim |\boldsymbol{d_{km}}|^2 |\dot{\boldsymbol{R}}|^2 \sim |\boldsymbol{d_{km}}|^2 T_{MD}, \tag{2.10}$$

where $\gamma, NA, \boldsymbol{d_{km}}, \dot{\boldsymbol{R}}$, and T_{MD} represent the relaxation rate, non-adiabatic coupling, electron-phonon coupling term, ion velocity, and temperature, respectively. The last proportion is based on the statistical thermodynamic definition of temperature. Equation (2.10) indicates that γ should be proportional to T_{MD} if $\boldsymbol{d_{km}}$ is temperature-independent. However, our calculated results, shown in Fig. 2.8, deviate significantly from the expected trend. The decay rate can be better fitted to $T^{0.371}$ and $T^{0.148}$ for the QD and EQD respectively. This deviation indicates that $\boldsymbol{d_{km}}$ must be temperature-dependent. To confirm that, we obtained the $|\boldsymbol{d_{km}}|^2$ defined in Eq. (2.5) associated with the initial state and LUMO for both QD and EQD at different temperatures, and the results are plotted in Fig. 2.9. It is clear that $|\boldsymbol{d_{km}}|^2$ does have a negative temperature dependence, which can be fitted to $T^{-0.549}$ and $T^{-0.885}$ for the QD and EQD respectively. After substituting $|\boldsymbol{d_{km}}|^2$ with the fitting functions into Eq. (2.10), the obtained relationships between γ and T_{MD} are $\gamma \sim {T_{MD}}^{0.45}$ for the QD and $\gamma \sim {T_{MD}}^{0.11}$ for the EQD, which agree well with the previous results from the fitting. Thus the weaker temperature dependence of hot electron decay rate can be attributed to the negative temperature dependence of $\boldsymbol{d_{km}}$, which

probably arises from the negative dependence of $\boldsymbol{d_{km}}$ on the thermal expansion in NCs[111]. Furthermore, $\boldsymbol{d_{km}}$ has stronger negative temperature dependence in the EQD than the QD. Experimental results show that for CdSe NCs, as size decreases the lattice constants decrease correspondingly[115]. It could be deduced that lattice parameters in the EQD are larger than those in the QD and our calculated results shown in Fig. 2.1 confirm that Cd-Se bond is longer in the EQD than QD. Therefore, assuming the EQD and QD have the same thermal expansion coefficient then a larger thermal expansion is expected in the EQD with the same temperature rise, which will in turn make it reasonable that $\boldsymbol{d_{km}}$ has stronger negative temperature dependence in the EQD.

CHAPTER 3. PHOTOVOLTAICS -- WET CHEMISTRY SYNTHESIS AND CHARACTERIZATION OF SEMICONDUCTOR NANOCRYSTALS

3.1 Experiments and Characterizations

3.1.1 Experiments

Because of the advantages of organometallic synthesis method mentioned before, organometallic method is adopted to synthesize different kinds of semiconductor nanocrystals. Typical procedures of pyrolysis of organometallic compounds method include precursor preparation, precursor injection, crystal nucleation and growth, reaction quenching and post-synthesis treatments, as shown in Figure 3.1. Unless stated otherwise, all chemical reagents were purchased from Alfa Aesar.

In the step of precursor preparation, chalcogen precursor is prepared through heating a mixture of chalcogen element and metal precursor is prepared through heating a mixture of metal compound and surfactant. Chalcogen element, like selenium (Se), tellurium (Te), and sulfur (S), can be dissolved by reacting with tri-n-octylphosphine (TOP) to form some complex compound. Metal compound can be metal oxide, chloride, or acetate. Surfactant can be oleic acid (OA, TCI America), TOP/TOPO, or phosphonic acid (PA). Surfactant is the most influential factor that determines the shape and surface chemistry property of the synthesized nanocrystals by attaching to various crystal planes and modifying their growing speed. Solvent can be either coordinating, like diphenyl ether

(DPE), or non-coordinating, like 1-octadecene (ODE). At high temperatures, oleic acid may show some degree of decomposition and result in a precursor solution with a yellowish or brownish color.

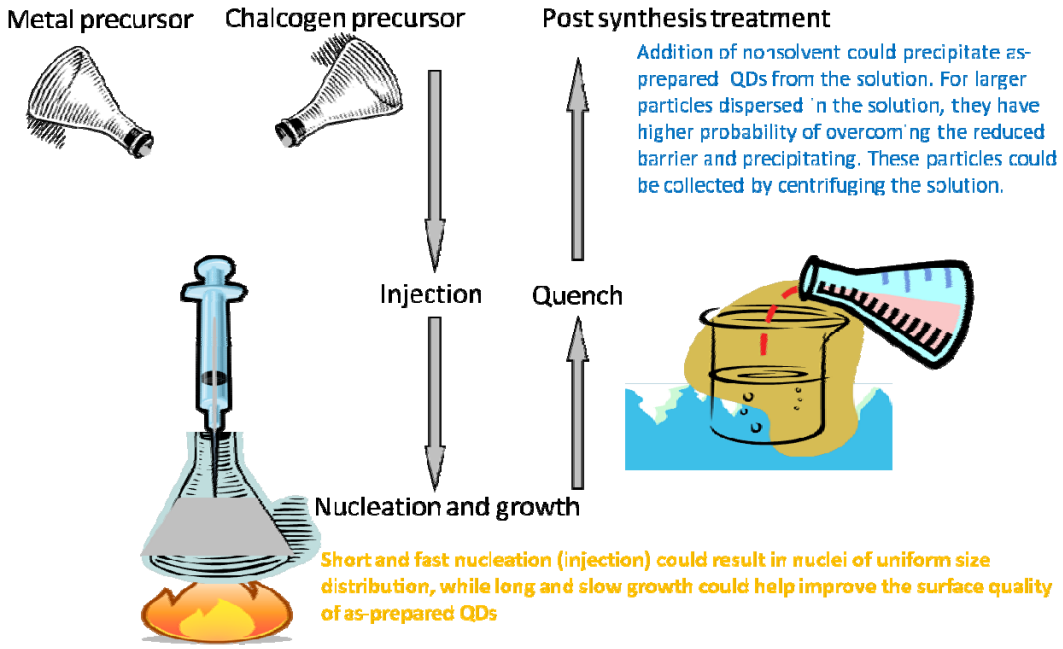

Figure 3.1. Illustration of pyrolysis of organometallic compound method.

In the step of precursor injection, the chalcogen precursor is first mixed with the metal precursor and then injected from a syringe into hot solvent under vigorous stirring. The fast injection leads to a short burst of homogeneous nucleation. The subsequent depletion of reagents and drop of temperature terminate the nucleation process. Continuous heating favors the growth of the nuclei. Murray[4] and Reiss[116] claim that slow growth can result in highly monodisperse nanocrystals, while Yin et al.[117] claim that slow growth can yield nanocrystals with broad size distribution. To obtain nanocrystals with narrow size distribution, Ostwald ripening process is not desired because it can broaden the size distribution of nanocrystals by growing big particles at the sacrifice of small particles.

In the step of reaction quenching, the hot solution is quenched in a mixture of ice and water and the reaction is immediately terminated due to the sharply dropped temperature. The fast termination of reaction provides a flexibility to precisely control the crystal size and avoid any over-growth.

After synthesis experiment is done, post-synthesis treatments can be performed to separate the nanocrystals from the raw solution, remove the excessive surfactants from the nanocrystal surface, narrow down the shape and size distribution, and modify the surface properties of the nanocrystals.

To minimize the ambiguities caused by samples' polydispersity and get a clear view of the relationship between material properties and morphologies, monodisperse nanocrystals are generally needed. There are two different approaches to narrow down size distribution, size selective precipitation[4] and size distribution focusing[116, 118].

Size distribution focusing is an in-synthesis treatment and is designed based on the proposal of Reiss that small crystals can grow faster than large crystals if the monomer concentrations are high enough[116], which is the opposite process of Ostwald Ripening. In experiment, the high concentrations of monomers are usually achieved by a secondary injection of precursors[118].

Size selective precipitation is a post synthesis treatment and is the most widely used method in narrowing down size distribution. Typical procedures of size selective precipitation include adding non-solvent into the solution, centrifuging the solution to separate precipitates from the supernatant, and redispersing precipitates with solvent. Depending on the requirements on the range of size distribution, size selective precipitation might need to be performed multiple times.

In our experiments, size selective precipitation is the only method used to narrow down the size distribution of synthesized nanocrystals. Hexanes and ethanol are used as the solvent and non-solvent pair.

3.1.2 Characterizations

Various characterizations are performed on synthesized nanocrystals to study their morphologies, structures, optical properties and surface chemistry conditions.

UV-visible absorption spectroscopy has been used to monitor the nanocrystal growth during synthesis and size distribution after synthesis. Samples for UV-visible absorption spectroscopy are prepared by dispersing the nanocrystals into hexanes. UV-visible spectra are recorded on a Molecular Dynamics SpectraMax Plus 384 UV-Visible Plate Reader with the spectrum scanning mode. The scanning range of the wavelength is set to be 400 – 750 nm with an increment of 1 nm.

XRD has been used to characterize the crystal phase and average crystal size of the synthesized nanocrystals. Samples for XRD are prepared by precipitating the nanocrystals from the solution, thoroughly washing them with ethanol and drying them in the nitrogen. XRD patterns are obtained on a Bruker D8 Focus X-Ray Diffractometer with the theta-2theta scanning mode. The x-ray is from a Cu kα source with a wavelength of 0.154 nm. The scanning range of 2theta is set to be 20 – 65 degrees with an increment of 0.0256 degrees. The scanning speed is set to be 5 degrees/min.

TEM has been used to characterize the morphology and the crystal structure of the synthesized nanocrystals. Samples for TEM are prepared by dispersing nanocrystals into hexanes and then dropping the solution onto copper grids coated with holey carbon films. TEM images are obtained on an FEI-Tecnai TEM with an accelerating voltage of 200 KV.

Raman spectroscopy has been used to investigate the phonon properties in the nanocrystals. Samples for Raman spectroscopy are prepared by thoroughly washing and drying the NCs and then applying the dry NC powders onto glass slides. Raman spectra are recorded on a Jobin-Yvon T64000 high resolution Raman spectrometer and a Horiba XploRA confocal Raman microscope with excitation energy of 2.33 eV (532 nm). The power of the laser is set to be low, ~0.2 mW. The spectrum is obtained by averaging five acquisitions, each of which takes 60 s.

3.2 Results and Discussions

3.2.1 Growth of CdSe NCs

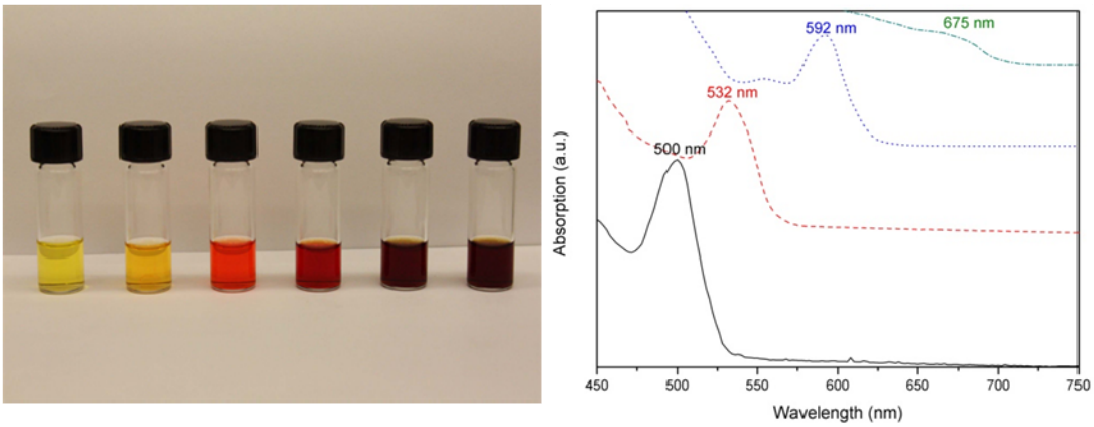

Figure 3.2. Picture and absorption spectra of CdSe NCs with different sizes.

Figure 3.2 shows a picture and absorption spectra of a series of CdSe NC samples. These samples are synthesized at the same temperature, 250 °C, for different reaction times. The NC size increases with increasing reaction time. Different sizes of CdSe NCs have different colors. As seen in the picture, from left to right, the NC size increases and the color changes from light yellow to dark red. With absorption spectra, useful information can be obtained about the NCs. The band gap can be calculated from the position of the absorption peaks, and the size distribution can be estimated from the width

of the peaks. As shown in Figure 3.2, the sharp absorption peak indicates the narrow size distribution of the QDs, which is achieved by precisely controlling the reaction conditions, such as fast injection, small fluctuation in reaction temperature, vigorous stirring and fast quenching. The absorption peak positions are marked. The spectra with absorption maxima located at 500, 532, 592 and 675 nm correspond to reaction times of 10 s, 30 s, 10 min, and 90 min, respectively. The absorption peak shifts from 500 nm to 670 nm as the reaction time increases from 10 s to 90 min. The red shift of absorption peak is attributed to the growth of the QDs, which decreases the band gap.

The reaction temperature is a crucial factor in determining the upper limit of the QD size from the energy perspective, and the absorption results also confirm it. The absorption maximum can only go up to 670 nm when the temperature is no higher than 250 ℃ no matter how long the reaction time is.

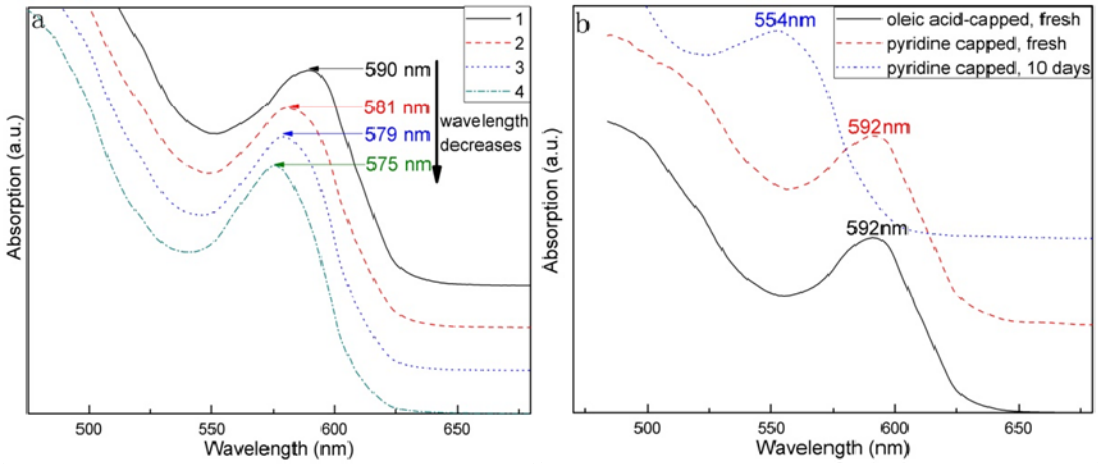

Figure 3.3. Absorption spectra. (a) After size-selective precipitation, (b) Before and after ligand exchange.

Size-selective precipitation is a post-synthesis procedure that can both narrow down the size distribution of as synthesized NCs and separate NCs of different sizes. In this process, bigger particles tend to aggregate and precipitate faster than smaller particles as

a result of the larger Coulomb attraction force between bigger particles. The effect of size selective precipitation is displayed in Figure 3.3a. Spectrum 1, 2, 3, and 4 correspond to samples obtained after being precipitated once, twice, three times and four times, respectively. It is shown that the QD size increases from sample 4 to 1, which is precipitated from the solution subsequently.

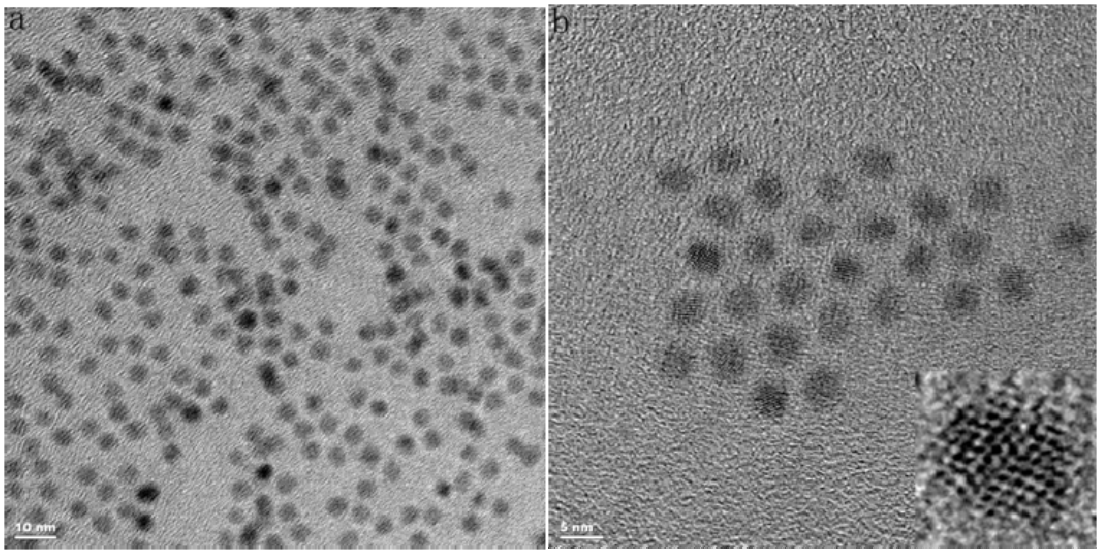

Figure 3.4. TEM images of the spherical CdSe NCs. Inset in (b) shows the lattice image of a single NC.

Ligand exchange is a post-synthesis procedure that can change the surface chemistry of as-synthesized NCs. Here, oleic acid is replaced by pyridine through ligand exchange. Figure 3.3b shows the visible absorption spectra recorded before and after the ligand exchange. No obvious change occurs in either position or width of the absorption peak before or after the ligand exchange, which is also found in the work of Lokteva et al. [119] Further study shows that the absorption peak taken from the same pyridine-capped sample 10 days after the ligand exchange shifts from 592 nm to 554 nm. The blueshift can be attributed to the oxidization of the QDs, which consequently decreases the

effective size of the QDs[120]. Because of the concern that QDs can get oxidized, no ligand exchange is performed on the QD samples that are to be used for characterizations.

Figure 3.4 displays typical TEM images of spherical CdSe NCs. Statistical results, based on a sample space of 150 random spherical NCs, show that the average size of the NCs is 4.3 nm with a standard deviation of 0.3 nm. The narrow size distribution agrees very well with the narrow width of the absorption peaks observed in Figure 3.2. The high-magnification TEM image in Figure 3.4b shows that neighboring NCs tend to organize in a short-range 2D hexagonal pattern. The inset in Figure 3.4b shows the lattice image of a single NC. Although some stacking faults are present in the NC, the periodic atomic arrangements can still be figured out, indicating the high crystallinity of the wet-chemistry synthesized QD.

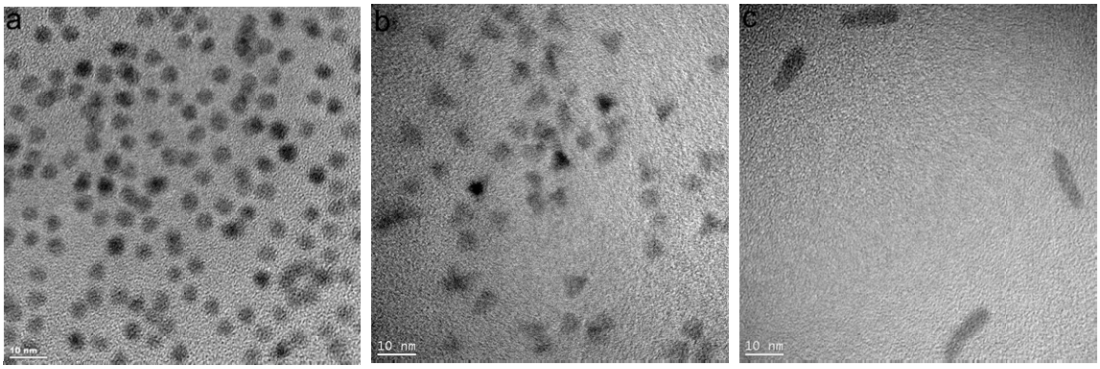

Figure 3.5. Typical TEM images of CdSe NCs of various shapes. (a) Spherical, (b) Triangular, (c) Elongated.

Besides spherical NCs, CdSe NCs of other shapes have also been synthesized. The morphology control here is mainly done by using different combinations of surfactants. A surfactant combination of OA and TDPA can result in spherical CdSe NCs. A combination of TOPO and TDPA can result in triangular NCs. A combination of TOPO, HPA and TDPA can result in elongated NCs. Generally, the shorter the carbon chain of

the PA is, the more anisotropic the shape is. Figure 3.5 shows typical TEM images of the spherical, triangular and elongated NCs, respectively. For the spherical samples, diameter variations up to ± 0.2 nm can be observed. For the triangular samples, diameter variations up to ± 0.4 nm can be observed. For the elongated samples, diameter variations up to ± 0.2 nm and length variations as much as ± 1.2 nm can be observed. The monodispersity in size and shape ensures that the influence of size and shape distribution on the characterization results can be minimized.

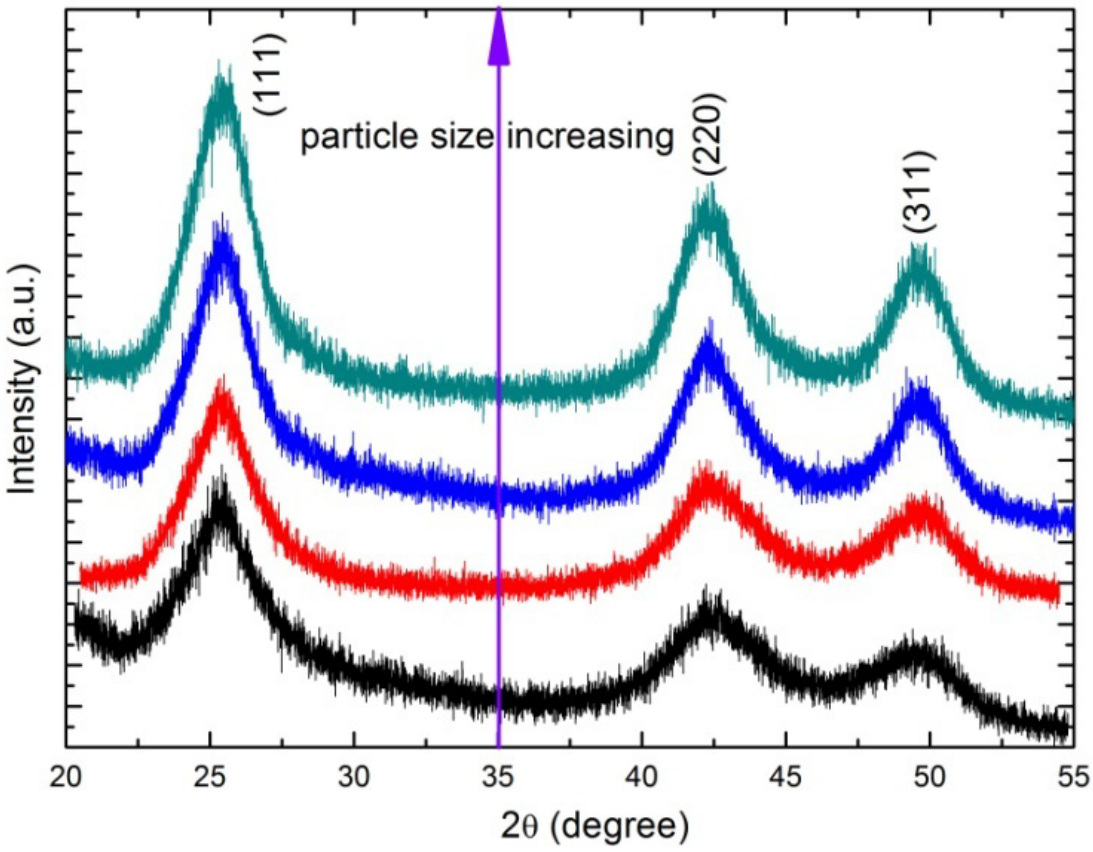

Figure 3.6. X-Ray diffraction patterns of a series of CdSe NC samples of various sizes.

Figure 3.6 shows the X-ray diffraction patterns of a series of CdSe NC samples of various sizes. These XRD patterns are taken on stress-free power samples using the same

x-ray diffractometer. All the diffraction patterns match the standard diffraction record of zinc-blende-structured CdSe. From bottom to top, the NC size increases. The diffraction peaks exhibit a trend of becoming narrower and stronger with increasing crystal size, while exhibit no trend of shifting with size.

3.2.2 Growth of PbSe NCs

3.2.2.1 Morphology Control of PbSe NCs

PbSe NCs of various shapes are obtained by simply replacing the solvent or tuning the volume ratio of TOP to OA. Octahedral (Figure 3.7a) and star-shaped (Figure 3.7b) NCs are produced with the same reaction system.

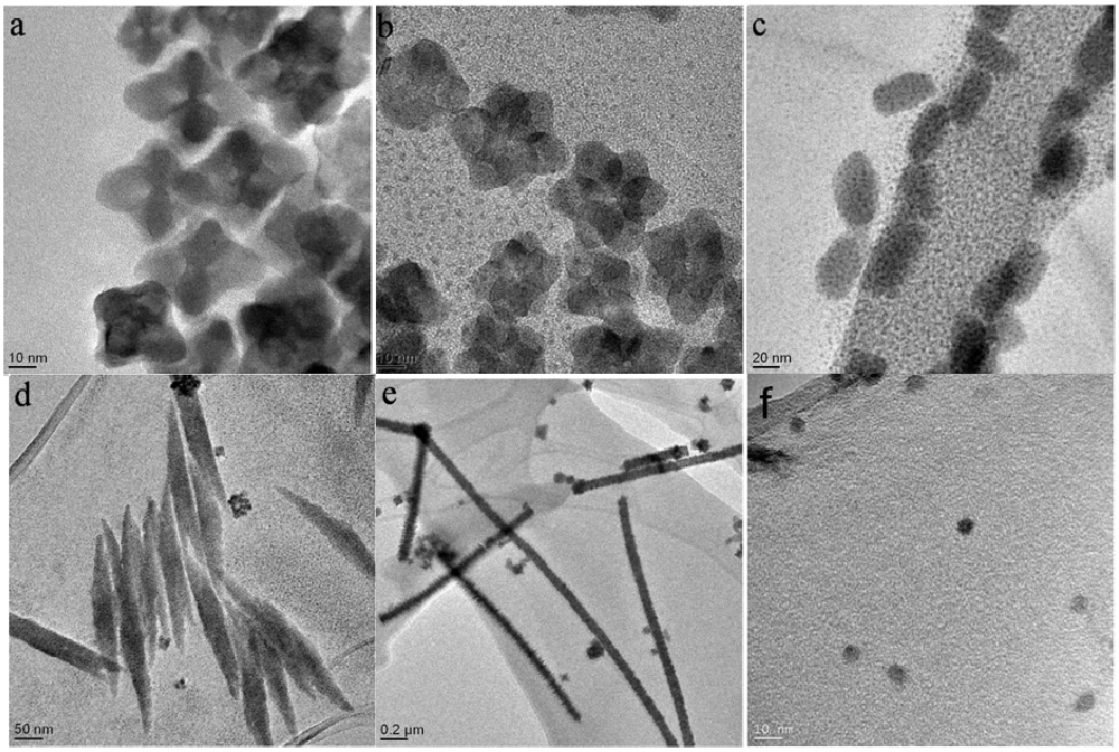

Figure 3.7. TEM images of PbSe NCs of various shapes. (a) Octahedral, (b) Star-shaped, (c) Diamond-shaped, (d)Elongated, (e) Nanowire, (f) Spherical.

According to the analysis made by Lu et al[72], star-shaped images are recorded along the [111] direction of octahedral NCs. When the commonly used solvent, ODE, is replaced by DPE, the resulted NCs exhibit different shapes from those produced with the reaction system using ODE as the solvent. High volume ratio of TOP to OA results in diamond-shaped NCs, and medium ratio results in elongated NCs, while low ratio results in nanowires. However, the change of Pb precursor won't lead to significant shape variation, as seen in the work of Lin et al[121]. Spherical NCs are produced by replacing ODE with squalane and keeping the volume ratio of TOP to OA at a medium level.

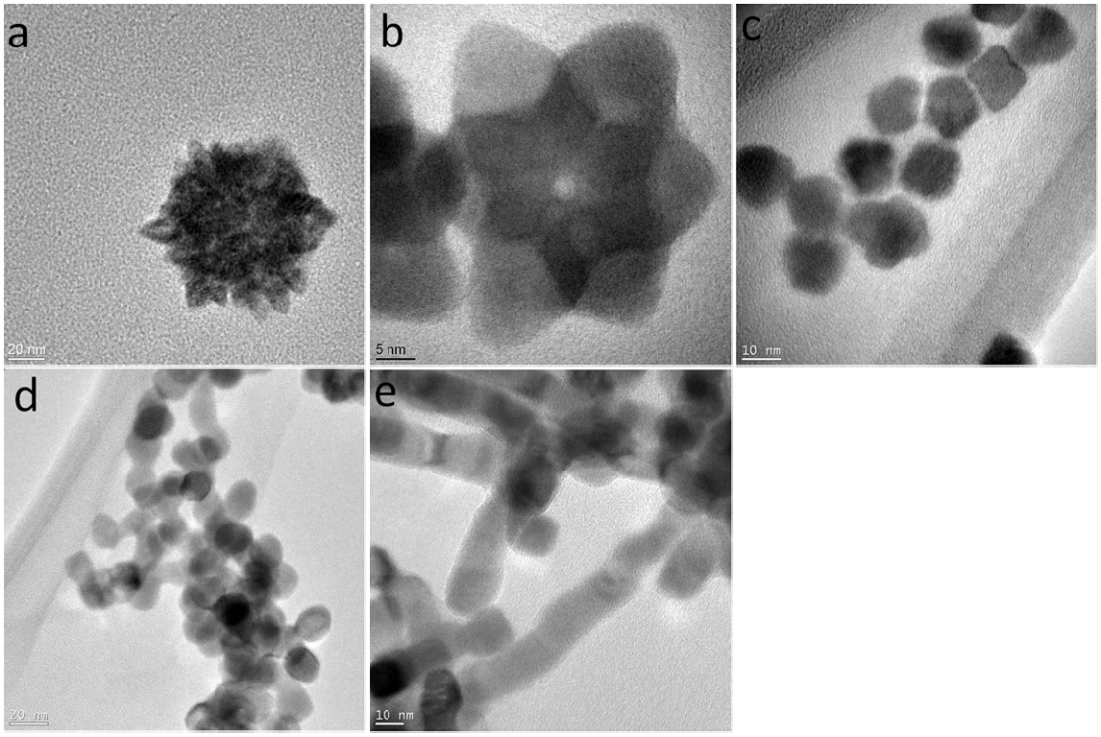

Figure 3.8. TEM images of PbSe NCs at different growing stages. (a) Initial, star-shaped , (b) Final, star-shaped, (c) Initial, nanowire, (d) Intermediate, nanowire, (e) Intermediate, nanowire.

3.2.2.2 Growth Mechanism of PbSe NCs

The growth of PbSe NCs is usually faster than that of CdSe NCs. The largest CdSe QDs that could be obtained in the pyrolysis of organometallic compound is around 11nm, which requires multiple injection of precursor, while the size of PbSe NCs can easily grow beyond 20 nm.

Figure 3.8 clearly shows the formation process of the star-shaped PbSe NCs. Small particles first aggregate and form a cluster with a diameter of 80nm. Later on, as the reaction proceeds, the small particles melt and re-crystallize into a big crystal. Figure 3.8c, 3.8d, and 3.8e demonstrate the growth process of PbSe nanowires. The originally discrete small crystals first get close enough to attach with each other. As the reaction proceeds, the boundaries of the attached crystals disappear and eventually grow into nanowires.

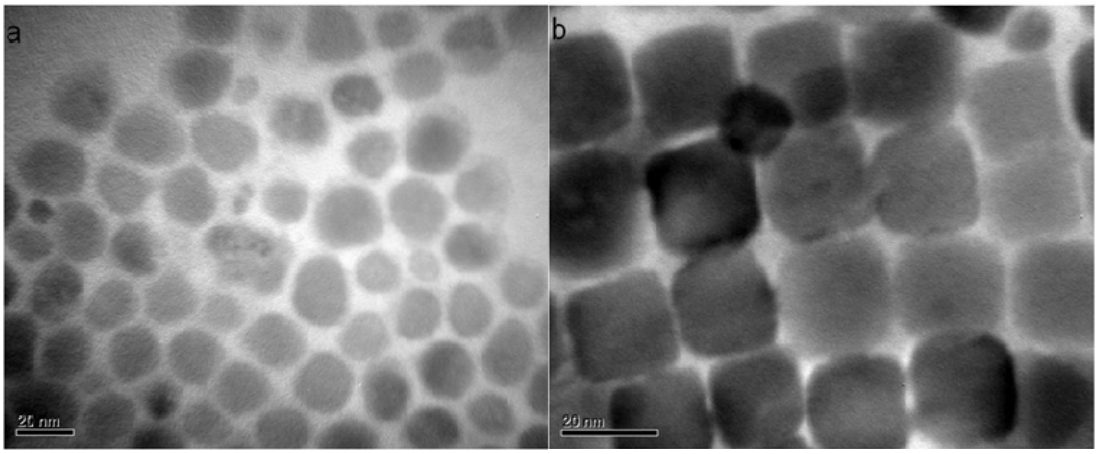

Figure 3.9. TEM images of PbTe NCs of various shapes. (a) Cuboctahedral, (b) Cubic.

3.2.3 Growth of PbTe NCs

The strategy to control the shape of PbTe NCs is to vary the molar ratio of Pb precursor and Te precursor and thus vary the molar ratio of surfactants. The cuboctahedral NCs are produced when the molar ratio of Te to Pb is 1, while the cubic NCs are produced when the molar ratio is 5.

3.2.4 Growth Mechanism of NCs in Wet-Chemistry Synthesis

Two mechanisms are observed in the growth process of semiconductor nanocrystals: addition of monomers and fusion of small crystallites.

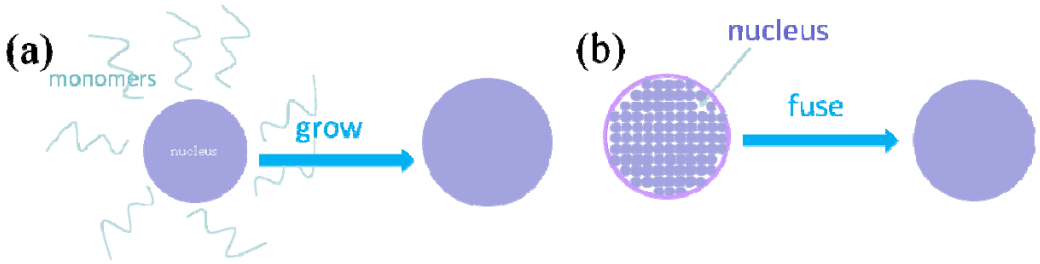

Figure 3.10. Illustration of nanocrystal growth mechanisms in the wet chemistry method. (a) Addition of monomers, (b) Fusion of small crystallites.

Figure 3.10 illustrates these two mechanisms. Figure 3.10a shows the details of monomer addition mechanism. First, nuclei are formed in the solution. Second, monomers in the solution are transported to the nuclei and added to the nuclei to grow them bigger. A typical material growing in this way is CdSe. Figure 3.10b shows the details of small crystallite fusion mechanism. First, small nuclei are formed in the solution. Second, these small nuclei get together and form a big cluster and then after getting enough energy they fuse into big crystals. Typical materials growing in this way include PbSe and PbTe.

3.3 Temperature and Geometry Dependent Raman Spectra of CdSe NCs

Table 3.1. Size and shape information of CdSe NC samples.

Sample Name	Shape	Size
Sample 1	Spherical	~ 2.8 nm
Sample 2	Spherical	~ 3.6 nm
Sample 3	Spherical	~ 4.4 nm
Sample 4	Triangular	~ 4.2 nm
Sample 5	Elongated	~ 4.6 nm (D), ~ 13 nm (L)

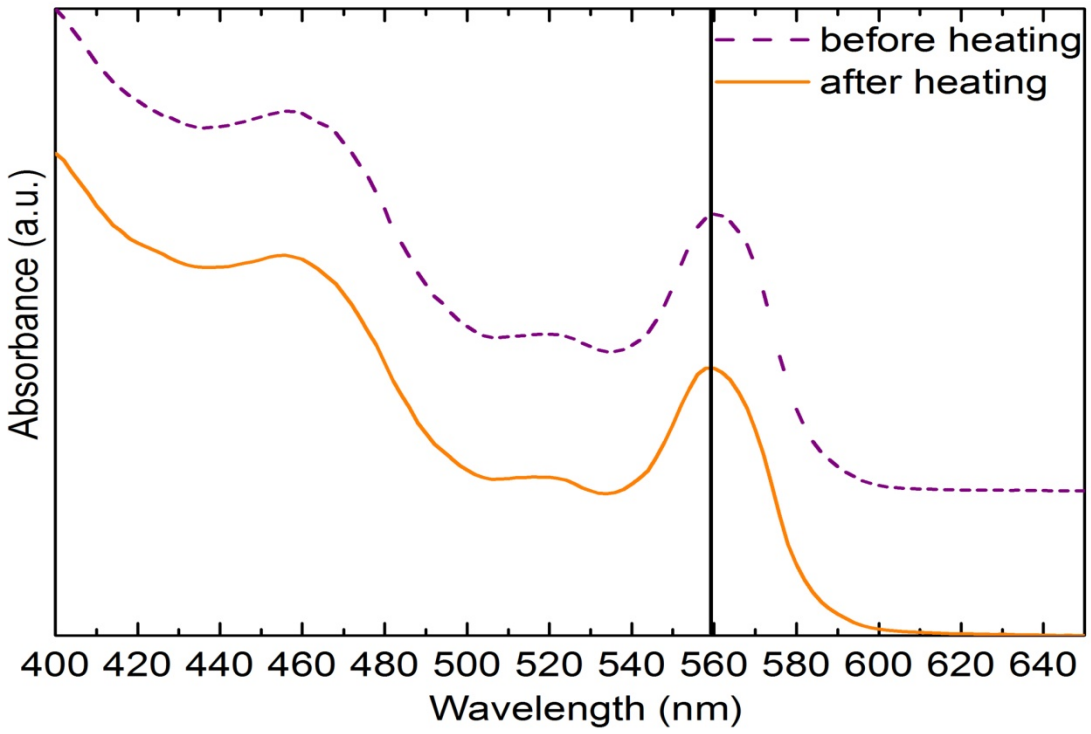

Figure 3.11. Typical UV-Vis spectra obtained before and after the Raman experiments.

Two series of CdSe NC samples have been characterized: spherical NCs of different diameters, and NCs of similar diameter but different shapes. All of them are synthesized by wet-chemistry method. Their morphology details are listed in Table 3.1. Sample 1, 2

and 3 are in the category of spherical NCs of different diameters, and their diameters are 2.8 nm, 3.6 nm and 4.4 nm, respectively. Sample 3, 4 and 5 are in the category of NCs of similar diameter but different shapes, and their shapes are spherical, triangular and elongated, respectively.

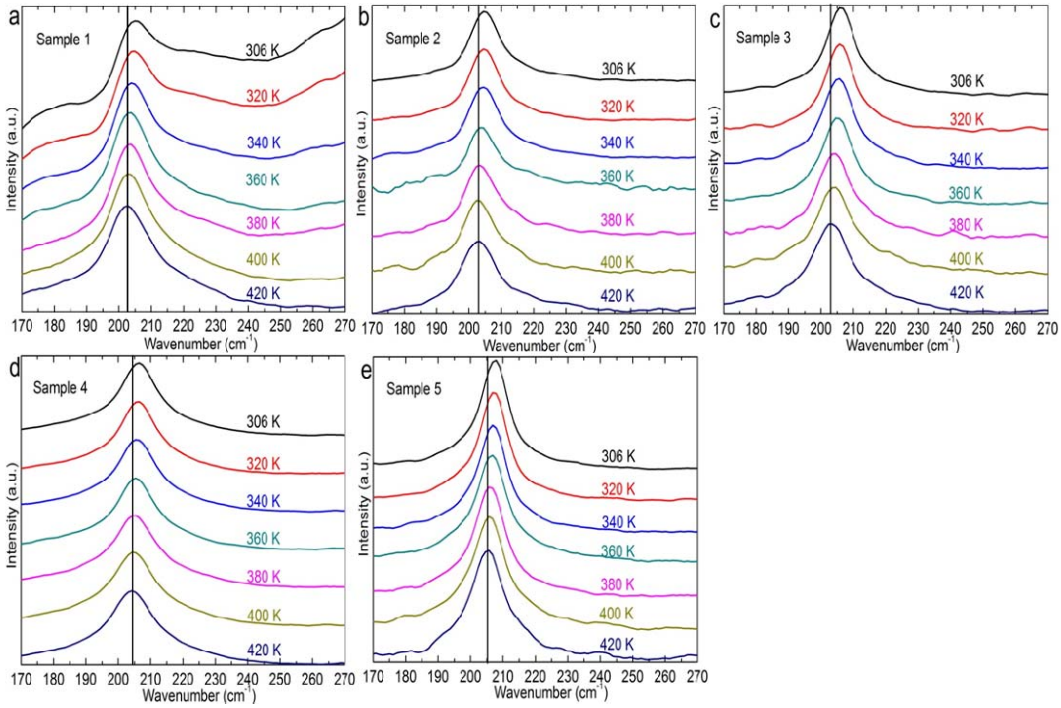

Figure 3.12. Typical Raman spectra obtained from 306 K to 420 K. (a) Sample 1, (b) Sample 2, (c) Sample 3, (d) Sample 4, (e) Sample 5.

UV-Vis absorption spectroscopy is used to monitor the size evolution and distribution of all the samples during the temperature-dependent Raman measurements. Figure 3.11 shows typical absorption spectra obtained before and after the Raman experiments. For the purpose of clarification, a vertical line is drawn to mark the peak position of the first excitonic transition between $1S_e$ and $1S_h$. It can be seen that no obvious change in the peak position or width has occurred during the Raman experiments, indicating no local-heating induced surface environment change or NC growth. This can be attributed to the

low excitation-laser power and the protection of residual OA and TOPO from oxidization (both OA and TOPO are strong binding ligands[119], unlike pyridine).

Figure 3.12 shows the Raman spectra as a function of the temperature for all the CdSe samples listed in Table 3.1. For the purpose of clarification, the spectra are normalized to the intensity of the LO phonon peaks and then shifted vertically. It is seen that for each sample the LO phonon peak shifts to lower frequency and broadens with increasing temperature, which can be attributed to the anharmonicity in the inter-atomic potential [54, 56, 122]. The broad SO phonon peak has been suppressed significantly, which can be attributed to the modified dielectric medium in the closely-packed NC assemblies[122].

Compared with its frequency, the full width at half maximum (FWHM) of Raman peak is very sensitive to temperature, size distribution and absolute value of peak intensity[122]. Although each sample has very narrow size and shape distribution, there still are variations of size distribution among different samples, as mentioned previously. Therefore, the rest of our study is restricted to the temperature dependence of peak frequency.

As suggested by Burke *et al*.[123], Raman frequency can be written in terms of temperature as,

$$\omega(T) = \omega_0 + \Delta\, \omega_{TE}(T) + \Delta\, \omega_A(T) \tag{3.1}$$

where ω_0, $\Delta\omega_{TE}(T)$, and $\Delta\omega_A(T)$ represent the frequency at 0 K, the frequency shift due to thermal expansion effect, and the frequency shift due to anharmonic phonon-phonon interaction, respectively. Within the temperature range studied in this work (300 K – 420 K), both $\Delta\omega_{TE}(T)$[122] and $\Delta\omega_A(T)$[124] can be approximated to change linearly with

temperature. Therefore, the overall frequency shift varies linearly with temperature and can be approximated as[123],

$$\Delta\omega(T) \approx -3\omega_0\alpha\gamma\Delta T - 4\frac{k}{hc\omega_0}a\Delta T = -\left(3\omega_0\alpha\gamma + 4\frac{k}{hc\omega_0}a\right)\Delta T, \qquad (3.2)$$

where $\alpha, \gamma,$ and a represent the linear thermal expansion coefficient, the Gruneisen parameter, and the constant for the anharmonic three-phonon process, respectively.

The peak frequency is extracted from the Raman spectra by fitting the peak profile with a Lorentzian function. Figure 3.13 shows the LO phonon peak frequency as a function of the temperature for two series of NC samples. The data points can be well fitted with the linear model and the fitting results are inserted in the figures.

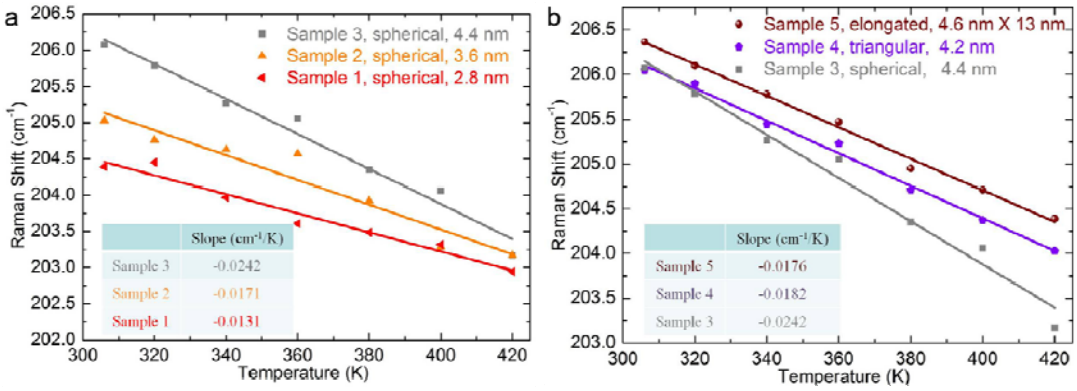

Figure 3.13. LO phonon frequency as a function of temperature. (a) Spherical CdSe NCs of different sizes, (b) Various-shaped CdSe NCs of similar size.

Figure 3.13a shows the results for spherical samples of different diameters. It is seen that the slopes are higher for larger samples, indicating higher temperature sensitivity in larger samples. Although the linear thermal expansion coefficient is found to decrease with increasing size[125], the constant for the anharmonic three-phonon process is found to increase with increasing size[56] and the anharmonic phonon process contributes much

more than the thermal expansion process[126]. Therefore it's reasonable that the slope increases with increasing crystal size.

As shown in Figure 3.13a and others' work[56, 127], the diameter has a noticeable impact on the Raman peak frequency. Figure 3.13b shows the results for samples of similar diameter but different shapes. This series of samples is designed to study the effect of shape while minimizing the effect of diameter. At room temperature, the Raman peak frequency of the elongated sample is slightly higher than that of the spherical and triangular samples because of the slightly larger diameter of the elongated sample, which is consistent with others' result[127]. The slope is smaller for the triangular sample than for the spherical sample. This is reasonable considering the diameter of the triangular sample is smaller. Furthermore, for 0D samples the shape doesn't seem to have as significant influence on the slope as the diameter. However, that is not always the case when comparing the results between the 0D and 1D samples. The slope is smaller for the elongated sample than the spherical sample even if the diameter of the former is larger. It has been shown that the elongated CdSe NCs are grown from the spherical NCs along the c-axis[128] and the LO phonon vibrates along the c-axis[43]. This indicates the necessity to take into account the thermal expansion effect in explaining the counterintuitive fitting result. The dimension along the c-axis is much larger in the elongated NCs than in the spherical NCs, and this results in a much smaller linear thermal expansion coefficient[125] in the elongated NCs. According to Equation 3.2, the significantly reduced contribution from the thermal expansion effect, together with a slightly increased contribution from anharmonic effect, can in turn lead to weaker temperature dependence

in the elongated NCs. Therefore it's reasonable to see a smaller slope in the elongated NCs than in the spherical NCs.

CHAPTER 4. THERMOELECTRICS -- WET CHEMISTRY SYNTHESIS AND BALL MILLING OF BISMUTH TELLURIDE-BASED NANOCRYSTALS

Besides wet chemistry method, ball milling method can also be used to make nanocrystals. Compared with wet-chemistry approach, ball milling approach has both advantages and disadvantages. Advantages include higher yield, no organic residue, more environment friendly and easier operation. Disadvantages include slower speed, less control over size and shape, and higher energy consumption. In thermoelectric applications, ball milling is more suitable in processes which require higher yield and less organic residue, while wet chemistry is more suitable in processes which require more precise control of the crystal geometry and smaller crystal size.

Furthermore, for practical thermoelectric applications, both p-type and n-type materials are needed, as shown in Figure 4.1a. In p-type materials, the majority charge carrier is hole, while in n-type materials, the majority charge carrier is electron. Intrinsic Bi_2Te_3 material is n-type semiconductor, and the switch of charge carrier can be realized by doping. For example, the doping of Se atoms into Bi_2Te_3 will form n-type material, while the doping of Sb atoms into Bi_2Te_3 will form p-type material. As shown in Figure 4.1b, in the case of Se atom doping, Se atoms will replace Te atoms and get into the lattice, while in the case of Sb atom doping, Sb atoms will replace Bi atoms and get into the lattice. Doping is mainly a diffusion process and dopants need to get enough energy before they can overcome the energy barrier and diffuse into the lattice. Therefore, it's important to

supply enough energy in the ball milling process in order to facilitate the doping process. Failure to do so will result in a mixture rather than a solid solution of the dopant and Bi_2Te_3.

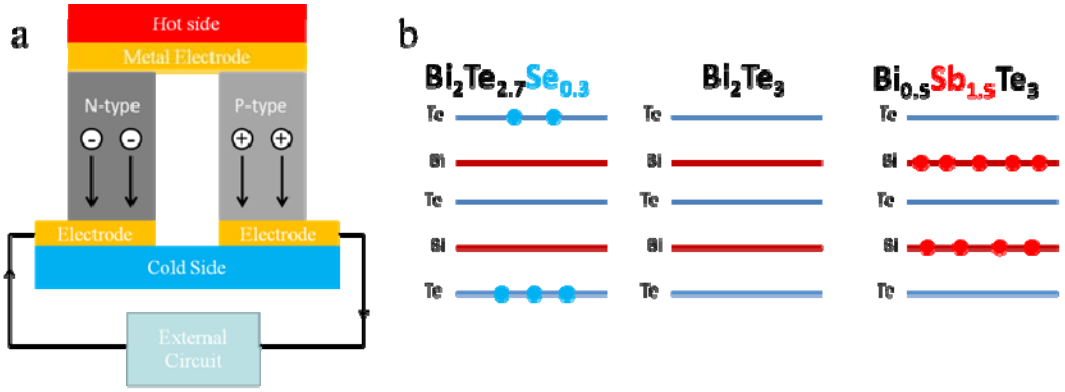

Figure 4.1. (a) Illustration of a thermoelectric power generator of the simplest form, (b) Illustration of Bi_2Te_3 doping.

4.1 Experiments and Characterization

4.1.1 Experiments

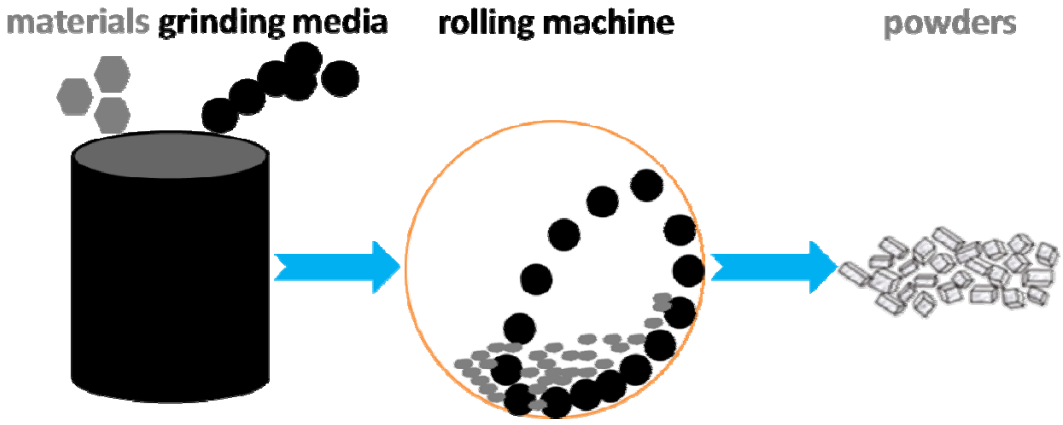

Figure 4.2. Illustration of ball milling method.

Wet chemistry method has been introduced in details in Chapter 3. Therefore, this part mainly introduces the details of ball milling method.

Ball milling experiments are performed on a tumble milling machine. All chemical reagents, unless stated otherwise, are purchased from Alfa Aesar. Figure 4.2 is an illustration of the procedures in ball milling. Unlike the bottom-up wet chemistry approach, ball milling is a top-down approach. The starting materials for ball milling are usually bulk materials, including Bi_2Te_3, Bi, Sb, Te, and Se. The bulk materials are first loaded into a jar together with ethanol and milling media. Then the jar is sealed under inert atmosphere (usually N_2) and put on the tumble milling machine to start ball milling. During the rotating process, the milling balls are first brought to some elevated position and gain potential energy. Then these balls start to fall off from the wall, during which their potential energy transforms into kinetic energy. The falling balls will collide with materials and transform their kinetic energy into heat, during which materials are crushed into smaller size. Since heat is constantly generated, it's necessary to add liquid solvent to help transfer out the heat and prevent undesired oxidation from occurring. After the experiment is finished, the milled materials are separated from the milling balls and then dried for further processes and characterizations.

4.1.2 Characterizations

Various characterizations are performed on synthesized nanocrystals to study their morphologies and structures.

SEM has been used to characterize the morphology of the nanocrystals. Samples for SEM are prepared by spreading the nanocrystal powders onto carbon tapes. SEM images are obtained on a Hitachi S-4800 Field Emission SEM with an accelerating voltage of 5 KV.

XRD has been used to characterize the crystal phase and average crystal size of the synthesized nanocrystals. Samples for XRD are prepared by precipitating the nanocrystals from the solution, thoroughly washing them with ethanol and drying them in the nitrogen. XRD patterns are obtained on a Bruker D8 Focus X-Ray Diffractometer with the theta-2theta scanning mode. The x-ray is from a Cu kα source with a wavelength of 0.154 nm. The scanning range of 2theta is set to be 20 – 65 degrees with an increment of 0.0256 degrees. The scanning speed is set to be 5 degrees/min.

TEM has been used to characterize the morphology and the crystal structure of the synthesized nanocrystals. Samples for TEM are prepared by dispersing nanocrystals into hexanes and then dropping the solution onto copper grids coated with holey carbon films. TEM images are obtained on an FEI-Tecnai TEM with an accelerating voltage of 200 KV.

FTIR spectroscopy has been used to monitor the surface chemistry conditions of the synthesized nanocrystals. Samples for FTIR spectroscopy are prepared by precipitating the nanocrystals from the solution, thoroughly washing them with ethanol and drying them in the nitrogen. IR absorption spectra are obtained on a Thermo Nicolet Nexus FTIR with a Smart iTR ATR.

Raman spectroscopy has been used to investigate the phonon properties in the nanocrystals. Samples for Raman spectroscopy are prepared by thoroughly washing and drying the NCs and then applying the dry NC powders onto glass slides. Raman spectra are recorded on a Jobin-Yvon T64000 high resolution Raman spectrometer and a Horiba XploRA confocal Raman microscope with excitation energy of 2.33 eV (532 nm). The power of the laser is set to be low, ~0.2 mW. The spectrum is obtained by averaging five acquisitions, each of which takes 60 s.

4.2 Results and Discussions

Several factors have been investigated to understand their influence on properties of the final products. Their influence on the final product is mainly evaluated based on the results of phase, size and morphology characterizations. Phase and size characterizations are mainly done using XRD, and morphology characterizations are mainly done using SEM and TEM. Quantitative analysis are made based on x-ray diffraction patterns using Scherrer equation.[129, 130] Scherrer equation was first proposed by Scherrer in 1918 and has been widely used to characterize the crystal size of powder and solid samples. Scherrer equation is written as

$$L = \frac{k\lambda}{\beta cos\theta}, \tag{4.1}$$

where L, k, λ, β and θ are the average crystal size, shape factor, x-ray wavelength, width of the diffraction peak, and position of the diffraction peak, respectively.

Table 4. 1. Synthesis conditions of the five samples shown in Figure 4.3, and 4.4.

Sample Name	Synthesis Condition
Sample 1	35 °C for 30 s
Sample 2	35 °C for 60 s
Sample 3	75 °C for 60 s
Sample 4	115 °C for 60 s
Sample 5	155 °C for 60 s

4.2.1 Wet-Chemistry Synthesized Nanocrystals

The x-ray diffraction patterns shown in Figure 4.3 are taken on stress-free powder samples using the same X-ray diffractometer. The synthesis conditions of the sample are shown in Table 4.1. All the diffraction patterns match the standard diffraction record of Rhombohedral-structured Bi_2Te_3. No unidentified peaks exist, indicating that the samples are impurity-free. The diffraction peaks exhibit a trend of becoming narrower, stronger and sharper with increasing the crystal size, while exhibit no trend of shifting with size.

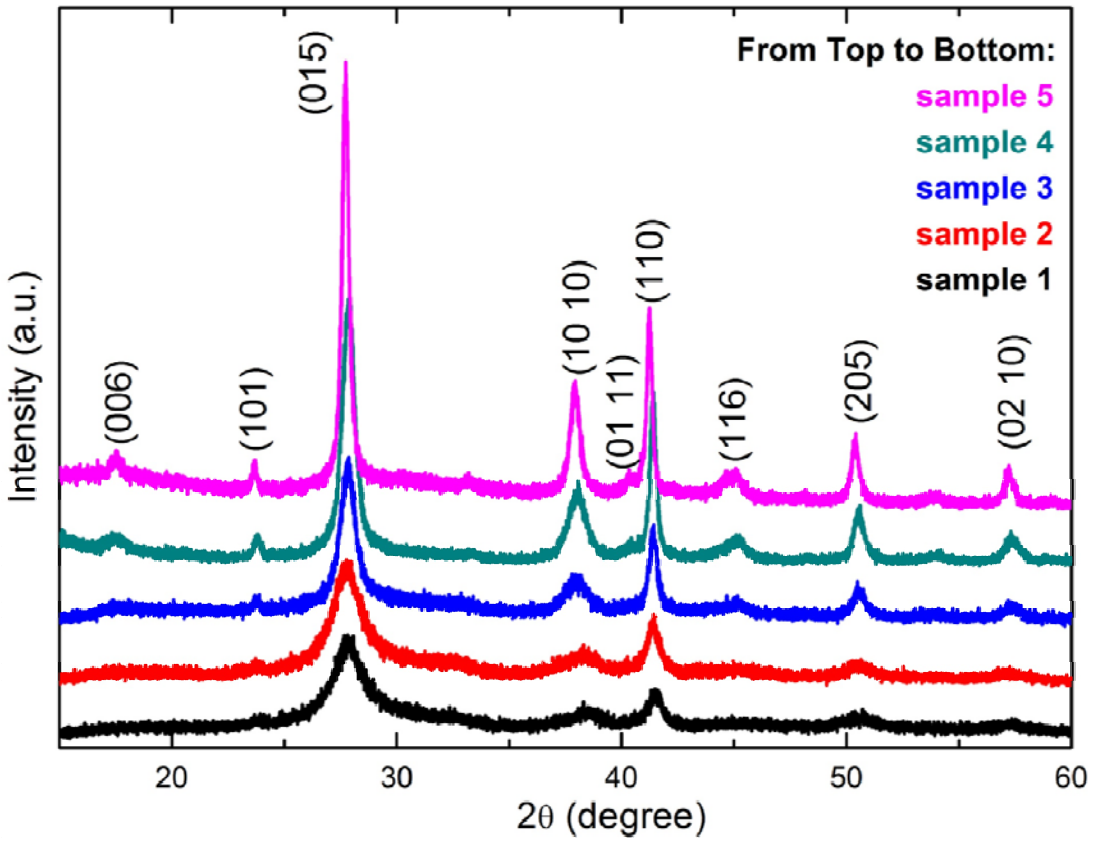

Figure 4.3. XRD patterns of Bi_2Te_3 NC samples synthesized at various conditions.

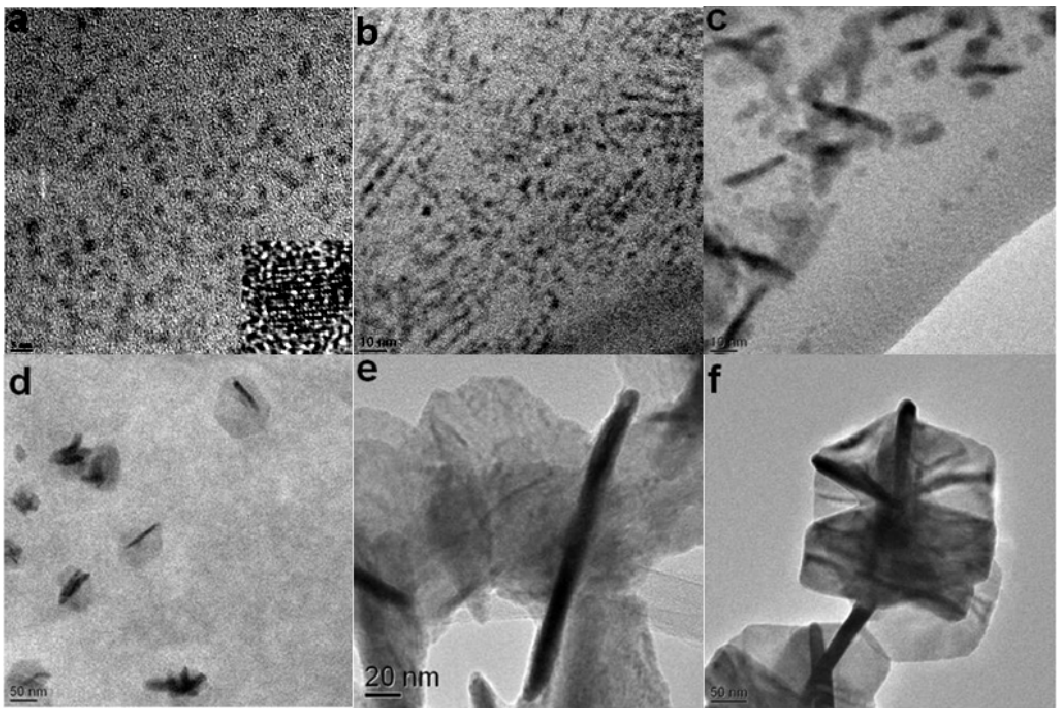

Figure 4.4. TEM images. (a) Sample 1, (b) Sample 2, (c) Sample 2, (d) Sample 3, (e) Sample 4, (f) Sample 5.

Representative TEM images of the same 5 samples are shown in Figure 4.4. Figure 4.4a and 4.4b are taken at different locations of Sample 1, made at the lowest reaction temperature (35 °C) that can yield Bi_2Te_3. The average size of nanoparticles in Sample 1 is 3±1 nm, much smaller than nanoparticles made by other groups. The inset of Figure 4.4a is the high-magnification TEM image of a single nanoparticle in Sample 1. Despite the existence of some lattice faults, the existence of periodical atomic arrangement confirms the high crystallinity of the nanoparticle. Although no obvious agglomeration of nanoparticles is observed and the dominant morphology is 0D nanoparticle in Sample 1, some nanoparticles are seen to self-arrange into line shapes, shown in Figure 4.4b, indicating the tendency of nanoparticles growing into nanorods.

Figure 4.4c shows the morphology of Sample 2, produced with a longer reaction time compared with Sample 1. Bi_2Te_3 nanorods have formed in Sample 2, matching the tendency of nanoparticles self-arranging into the line shape seen in Sample 1. The diameters of nanorods in Sample 2 match the diameters of nanoparticles in Sample 1. Although in Sample 2 some nanoparticles have grown into quasi-2D nanoflakes, the dominant morphology is 0D nanoparticle and 1D nanowire.

Figure 4.4d shows the morphology of Sample 3, made at a higher temperature compared with Sample 2. Compared with Sample 2, the growth of quasi-2D nanoflakes in Sample 3 has been significantly boosted, changing the dominant morphology from 0D and 1D nanocrystals in Sample 2 to 2D nanoplates in Sample 3.

Figure 4.4e and 4.4f show the morphologies of Sample 4 and 5 respectively, both made at higher temperatures compared with Sample 3. It is seen that further increase in reaction temperature leads to no significant morphology change but improvement in the crystallinity. Although both 1D nanorods and 2D nanoplates have been observed to grow larger, the dominant morphology is still 2D nanoplates in both Sample 4 and 5. The murky image of nanoplates in Sample 4 can be traced back to the partially crystallized parts and hence a relatively low local crystallinity, while Figure 4.4f shows that the crystallinity has been improved in Sample 5, which can be attributed to the increased reaction temperature.

Size increasing with increasing reaction time or temperature has been confirmed by the XRD results.

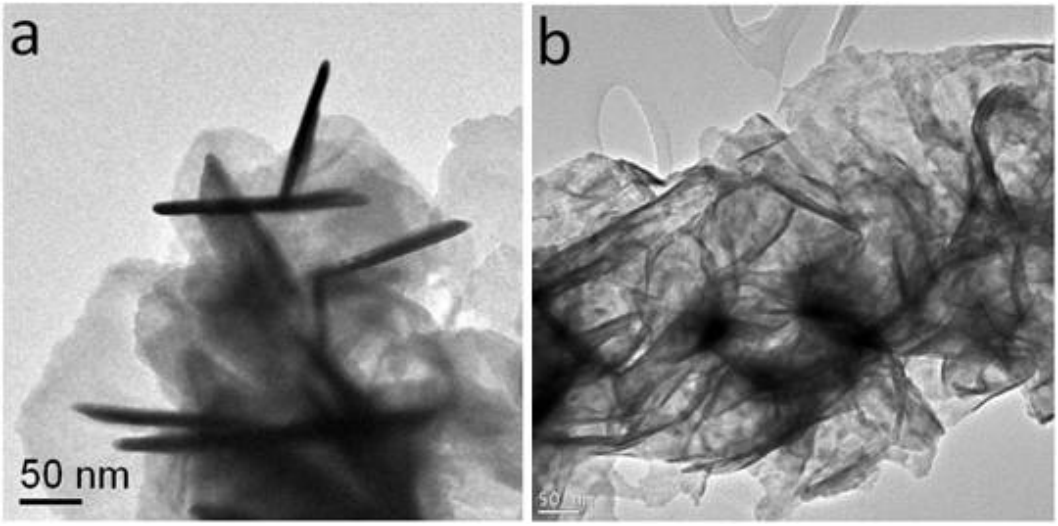

Figure 4.5. TEM images of Bi_2Te_3 NCs of various morphologies. (a) Mixed morphology of nanosheet and nanorod, (b) Single-morphology nanosheet.

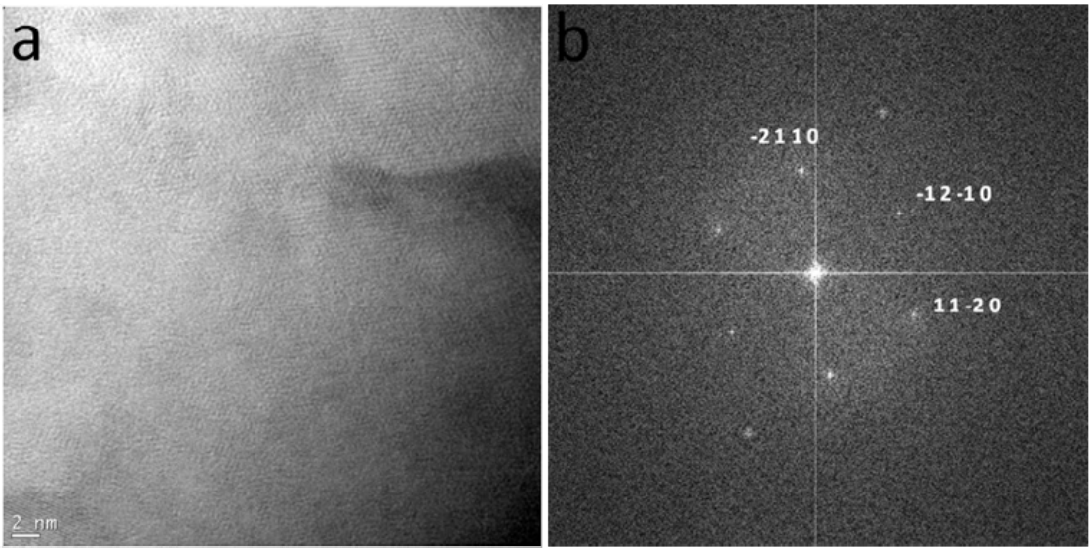

Figure 4.6. (a) High-magnification TEM image of nanosheet, (b) FFT simulated electron diffraction patterns of (a).

However, the morphology evolution is more complicated. A reaction system with ODE as the solvent generally results in a mixture of nanosheets and nanorods, as seen in Figure 4.5a. If ODE is replaced with DPE, the resulted product is single-morphology nanosheets,

as seen in Figure 4.5b. This is the first time that single-morphology Bi_2Te_3 nanosheets are synthesized using the pyrolysis of organometallic compound method.

In TEM images, the brightness is determined by the number of electrons penetrating the sample, so the contrast gives information about the thickness variation of the sample. Figure 4.6a shows a high magnification TEM image of single-morphology Bi_2Te_3 nanosheets. The uniform contrast in the TEM image indicates the uniform thickness of the nanosheet. Figure 4.6b shows an FFT simulated electron diffraction pattern of the same area shown in Figure 4.6a. A single set of diffraction spots with a six-fold symmetry can be figured out. The diffraction pattern can be identified as the projection of the reciprocal lattice of hexagonal Bi_2Te_3 in the [0001] direction, which indicates that both the upper and lower surfaces belong to the {0001} planes.

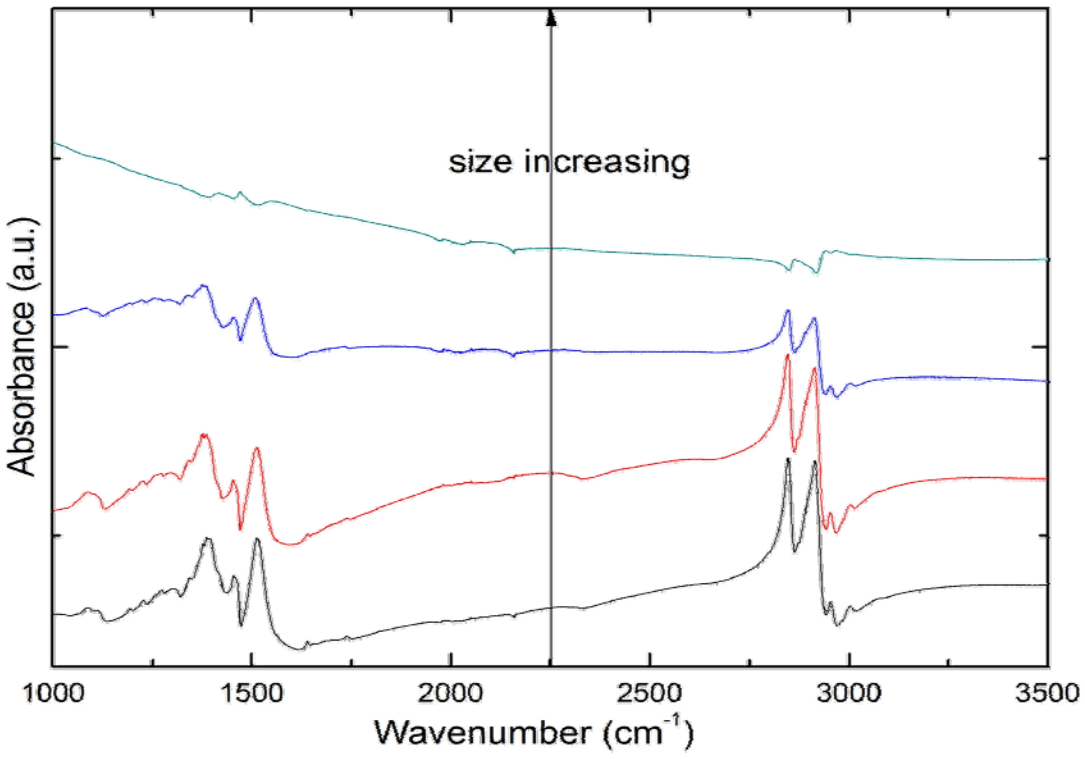

Figure 4.7. IR absorption spectra of a series of Bi_2Te_3 samples of various sizes.

Organic ligands on the surface of the NCs on one hand can prevent the degradation of NCs but on the other hand can form a barrier to prevent charge carriers from transferring between neighboring NCs. Therefore, it is necessary use effective methods to monitor the residue of organic ligands. Figure 4.7 shows the Infrared absorption spectra of Bi_2Te_3 NC samples of various sizes. From bottom to top, the nanocrystal size increases. The absorption peaks around 1465 cm^{-1} and 1585 cm^{-1} can be assigned to the carboxylate stretches, and the peaks between 2800 and 3000 cm^{-1} can be assigned to c-h stretch. These modes together confirm the existence of residual oleic acid on the NC surface. It can be seen that as crystal size increases, the absorption peaks become weaker and broader. This can be attributed to the decreasing surface to volume ratio with increasing crystal size.

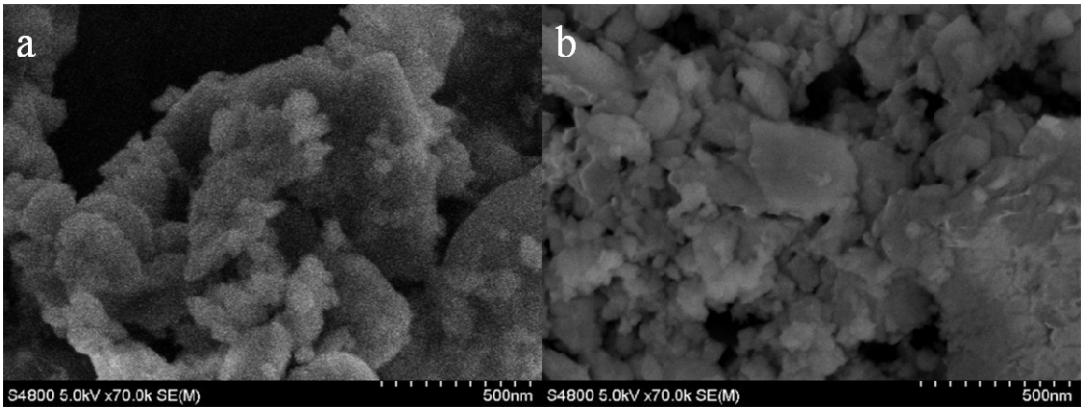

Figure 4.8. The effect of the milling medium size. (a) Ratio of small to big balls = 2: 1, (b) Ration of small to big balls = 1 : 2.

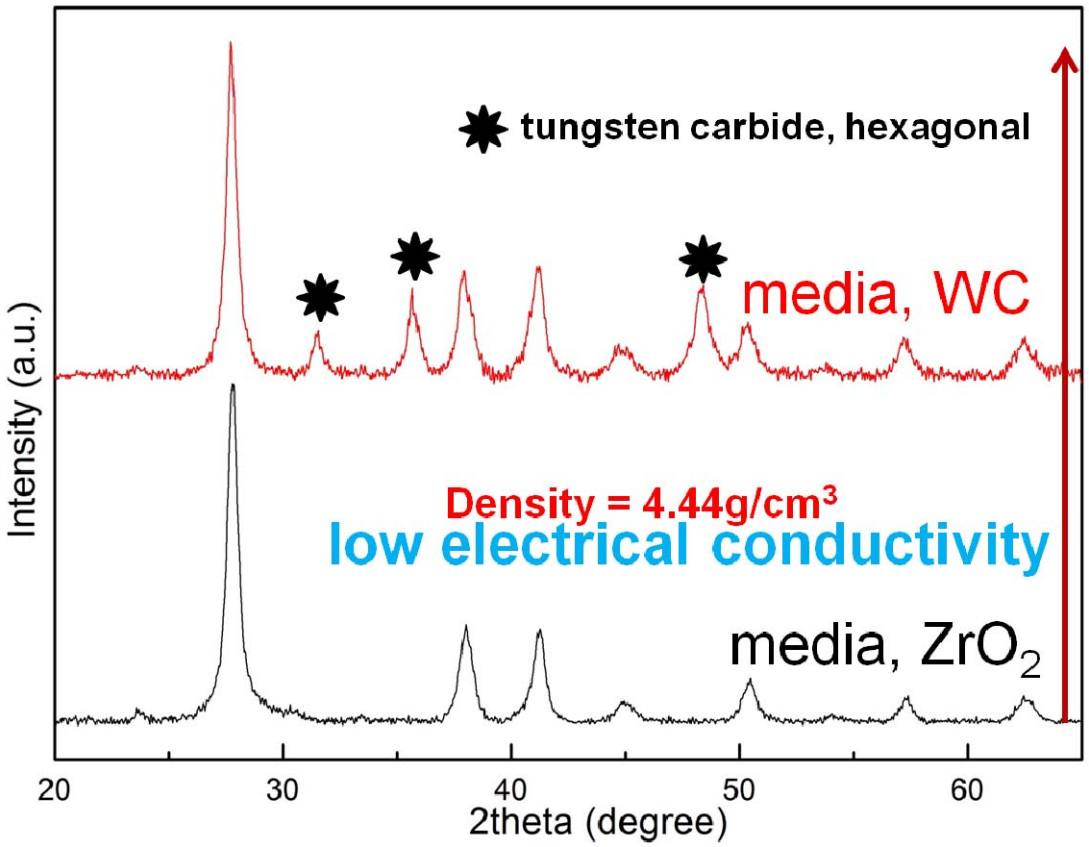

Figure 4.9. XRD patterns of samples milled by balls made of different materials.

4.2.2 Ball Milled Nanocrystals

The effect of the material and size of milling media has been studied. Figure 4.8 shows the SEM images of products milled by balls of different sizes. In Figure 4.8a, more small balls are used for milling. A considerable amount of coarse crystals coexist in the sample with fine crystals. In Figure 4.8b, more big balls are used for milling. The amount of coarse crystals has been significantly reduced and fine crystals are dominant in the sample. Comparison between Figure 4.8a and 4.8b shows that bigger balls are more efficient in grinding materials than smaller balls.

WC and ZrO_2 are both common materials for milling balls because of their excellent mechanical properties. WC is much heavier than ZrO_2. Figure 4.9 shows the XRD patterns of Bi_2Te_3 samples milled by balls made of different materials: WC and ZrO_2. The samples have been milled for the same amount of time, 72 h. From bottom to top, they are samples milled by ZrO_2 and WC, respectively. In the sample milled by WC, besides the diffractions peaks of Bi_2Te_3, three additional peaks can be figured out and attributed to WC, which means the sample has been contaminated by WC. In the sample milled by ZrO_2, only the peaks of Bi_2Te_3 can be figured out. However, the subsequent electrical conductivity measurement shows much lower electrical conductivity in ZrO_2-milled samples than in WC-milled samples, which is undesirable in thermoelectric applications. This can be attributed to material oxidation induced by the high temperature generated during milling and the oxygen element in ZrO_2. Therefore, although there's contamination from the balls, WC is a better milling medium than ZrO_2 and WC balls are used to mill all the samples in the rest of the experiments.

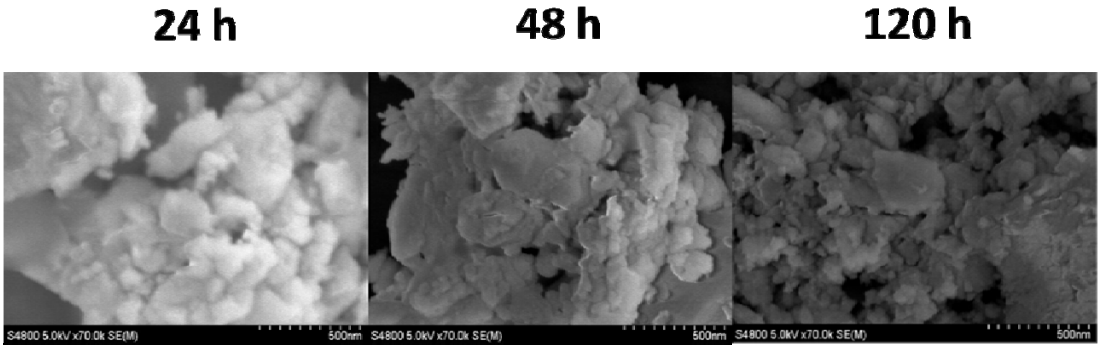

Figure 4.10. SEM images of samples milled for different times.

Figure 4.10 shows the SEM images of samples milled for different times. From left to right, the samples are milled for 24h, 48h, and 120h, respectively. As milling time

increases, more coarse crystals are ground into fine crystals, which results in an overall size reduction. More accurate conclusion can be drawn by quantitatively analyzing the XRD patterns using Scherrer Equation.

Figure 4.11 shows the XRD patterns of unmilled sample, sample milled with WC for 72h and 120h, respectively. For the purpose of clarification, the intensity of spectra has been normalized to the intensity of (015) peak and the pattern has been shifted in the vertical direction. The diffraction peak of the unmilled sample is very sharp, indicating the bulk nature of the material. As milling time increases, the (015) peak becomes broader, which according to the Scherrer Equation indicates size reduction in the sample. However, it is noteworthy that the diffraction peaks of WC also appear in the pattern for sample milled for 120h. Milling time analysis indicates that there's a tradeoff between sample size and sample purity.

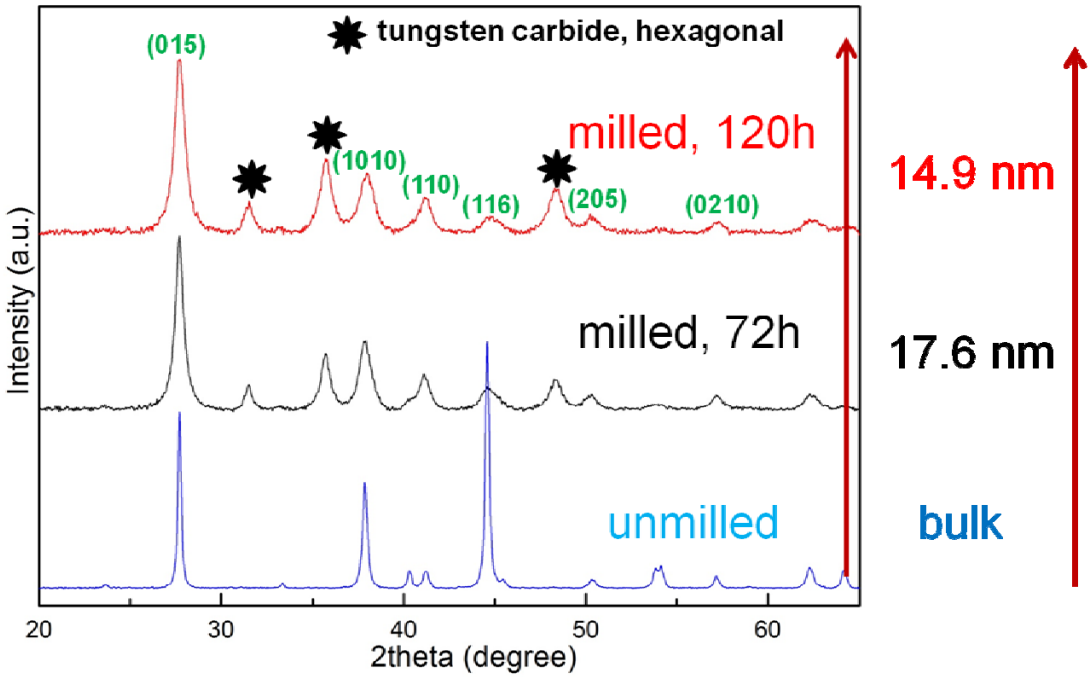

Figure 4.11. XRD patterns of unmilled sample, sample milled for 72h and 120h, respectively.

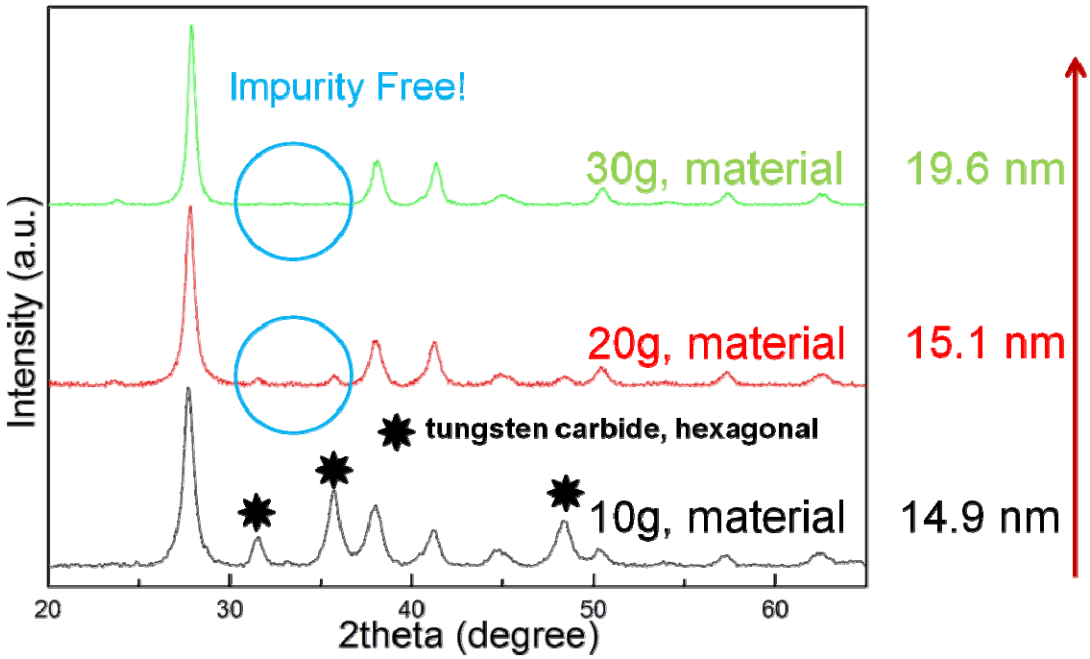

Figure 4.12. XRD patterns of samples made with 10g, 20g, 30g of starting materials.

The effect of amount of starting materials used for ball milling has also been explored. Figure 4.12 shows the XRD patterns of samples milled from various amount of starting materials. From bottom to top, the amount of materials has been increased from 10g to 20g to 30g. In the case of 10g materials, it can be seen the diffraction peaks of WC exist in the XRD pattern, indicating that a considerable amount of WC contamination in the sample. With increasing the amount of starting materials, the WC diffraction peaks eventually become weaker and then disappear in the case of 30g materials, indicating that the WC contamination has been minimized in the case of 30g materials. The estimated average crystal size, using Scherrer Equation, is 14.9, 15.1, and 19.6 nm, respectively, indicating there's a slight size increase with increasing the amount of starting material. Therefore, increasing the amount of starting material can minimize the amount of

contamination and increase the production yield without significantly sacrificing the nanocrystal size.

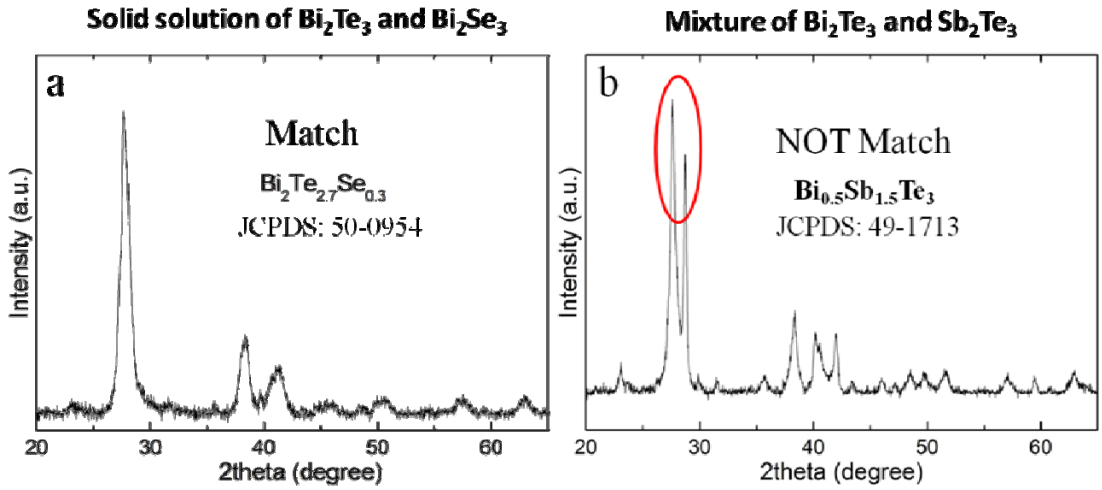

Figure 4.13. XRD patterns of Bi_2Te_3 samples after doping. (a) Se atom doping, (b) Sb atom doping.

In the case of ball milling Bi_2Te_3, the main function of milling is to provide enough energy to grind coarse crystals into fine ones. However, in the case of doping Bi_2Te_3, the milling process needs to provide energy to both grind coarse crystals and diffuse dopant atoms into the lattice. Therefore, the critical part for doping is whether enough energy can be supplied.

Figure 4.13 shows the XRD patterns of the Bi_2Te_3 samples after Se atom doping and Sb atom doping. The nominal compositions for Se-doped and Sb-doped Bi_2Te_3 samples are $Bi_2Te_{2.7}Se_{0.3}$ and $Bi_{0.5}Sb_{1.5}Te_3$, respectively. In Figure 4.13a, the diffraction pattern matches the standard diffraction pattern of $Bi_2Te_{2.7}Se_{0.3}$ (JCPDS: 50-0954), indicating the diffusion of Se atoms into Bi_2Te_3 lattice and formation of the solid solution of Bi_2Te_3 and Bi_2Se_3. In Figure 4.13b, as shown in the red circle, there are two peaks existing around 27 degrees. One can be assigned to the (015) diffraction of Bi_2Te_3 and the other can be

assigned to the (015) diffraction of Sb_2Te_3. This indicates that the sample is a mixture rather than a solid solution of Bi_2Te_3 and Sb_2Te_3. Further efforts have been made to optimizing the parameters of ball milling experiment, like increasing the milling speed to the maximum or increasing the milling time. Like what is shown before, they can further reduce the crystal size but they fail to drive Sb atoms into the Bi_2Te_3 lattice. Therefore, ball milling can't provide enough energy to facilitate the formation of the solid solution of Bi_2Te_3 and Sb_2Te_3. The sharp contrast between the results of the Se doping and Sb doping can be attributed to the different bonding strengths between monoatomic layers within the quintuple. As shown in Figure 4.1(b), each quintuple is formed by stacking five monoatomic layers on each other along the c-axis in the order of $Te^{(1)}$-Bi-$Te^{(2)}$-Bi-$Te^{(1)}$. There are two different types of Te atoms in the quintuple, and Se doping usually first occurs on $Te^{(1)}$ atoms. From the perspective of energy, the bonding strengths on $Te^{(1)}$ atoms are not as strong as those on the Bi atoms[70]. Therefore, it requires less energy for Se atoms to replace $Te^{(1)}$ than for Sb atoms to replace Bi atoms.

Table 4.2. Dominant morphology of the five samples shown in Figure 4.14.

Sample Name	Dominant Morphology
Sample 1	0D nanoparticle
Sample 2	0D nanoparticle and 1D nanorod
Sample 3	2D nanoplate
Sample 4	2D nanoplate
Sample 5	2D nanoplate

4.2.3 Morphology Dependent Raman Spectra of Bi_2Te_3 Nanocrystals

With the wet-chemistry synthesized Bi_2Te_3 nanocrystals of various morphologies, the morphology effect on Raman features has been systematically studied. Representative Raman spectra are shown in Figure 4.14. The dominant morphology in each sample has been inserted in Figure 4.14. For the purpose of clarification, all the spectra are normalized to the intensity of A_{1u} mode and shifted vertically. Five samples show two distinct sets of Raman features. The spectra of Sample 1 and 2 have similar features, while the spectra of Sample 3, 4 and 5 have similar features.

In the spectra of Sample 3, 4 and 5, three vibrational modes, E_g^2, A_{1u}, and A_{1g}^2, are present, among which E_g^2 and A_{1g}^2 are Raman active and A_{1u} is forbidden in bulk Bi_2Te_3. However, Tewelderhan et al [69, 70] have shown that the A_{1u} mode shows up in 2D few-quintuple Bi_2Te_3 layers due to the symmetry breaking in atomically-thin films. Considering the dominant morphology in Sample 3, 4 and 5 is 2D nanoplate, it's reasonable that their Raman features match the record of 2D few-quintuple Bi_2Te_3 layers [69, 70].

Due to symmetry breaking, A_{1u} mode becomes active not only in 2D nanostructure, but also in 0D and 1D structures. As the dimension shrinks from 2D to lower dimensions, the relative intensity of A_{1u} mode increases, which obscures the in-plane E_g^2 mode and makes it almost invisible, and the frequency of the A_{1g}^2 mode shifts from 135 cm^{-1} to 143 cm^{-1}. Although previous investigations on the blueshift of Raman modes in semiconductor nanocrystals have proposed several possible causes, like lattice contraction [46] and temperature decrease [42], the origin of the A_{1g}^2-mode blueshift from 2D structure to 0D/1D structure is not clear yet. Considering the morphology difference between 2D and

0D/1D structures, the blueshift of the mode can be induced by the shrink in the axial direction of the 0D/1D structure.

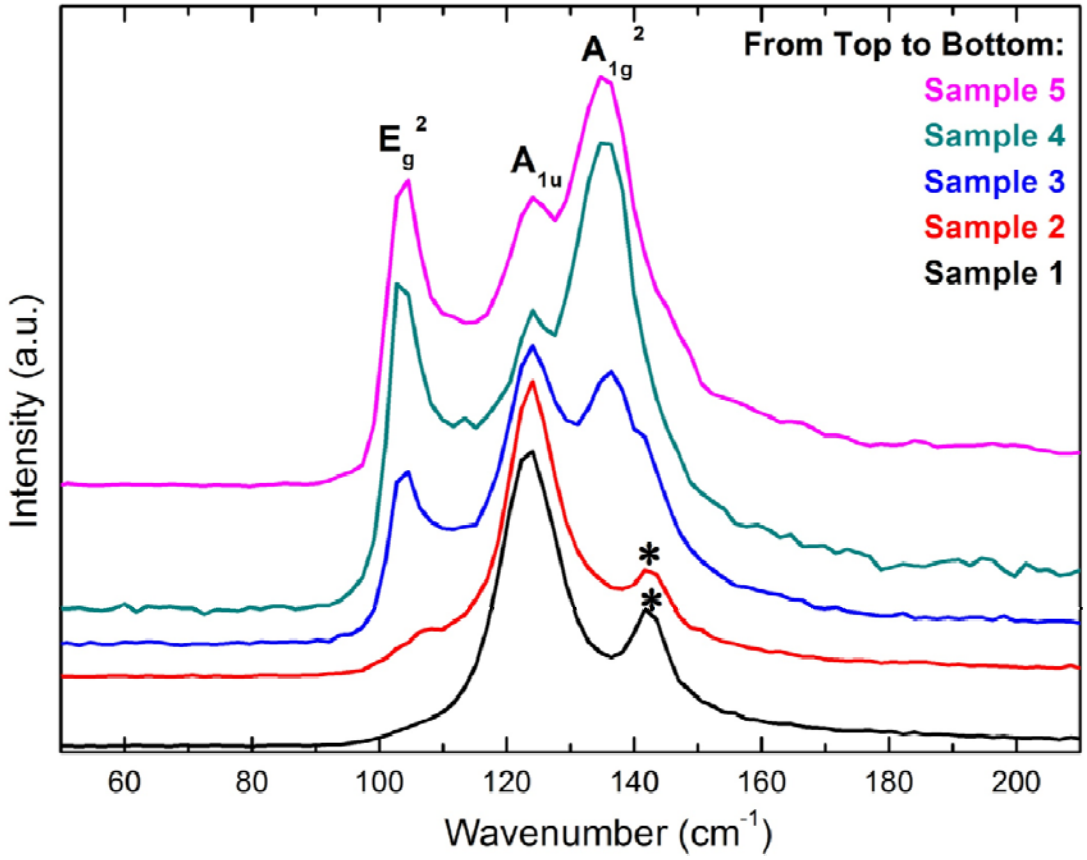

Figure 4.14. Raman spectra of wet-chemistry synthesized Bi_2Te_3 NCs.

Besides the wet-chemistry synthesized NCs, Raman spectra have also been obtained on ball-milled NCs. The sample shown here has an average crystal size of 15.4 nm and its Raman spectrum is shown in Figure 4.15. The Raman spectrum of bulk Bi_2Te_3 is also shown for the purpose of comparison. Like what is seen in the synthesized samples, in addition to the A_{1g}^2 and E_g^2 modes, the A_{1u} mode also exists in the spectrum of ball-milled NC sample. Compared with the wet-chemistry synthesized NCs, there are no organic ligands capping the ball-milled NCs. This indicates that the appearance of the A_{1u}

mode mainly depends on the crystal size rather than the surface chemistry condition of the crystals.

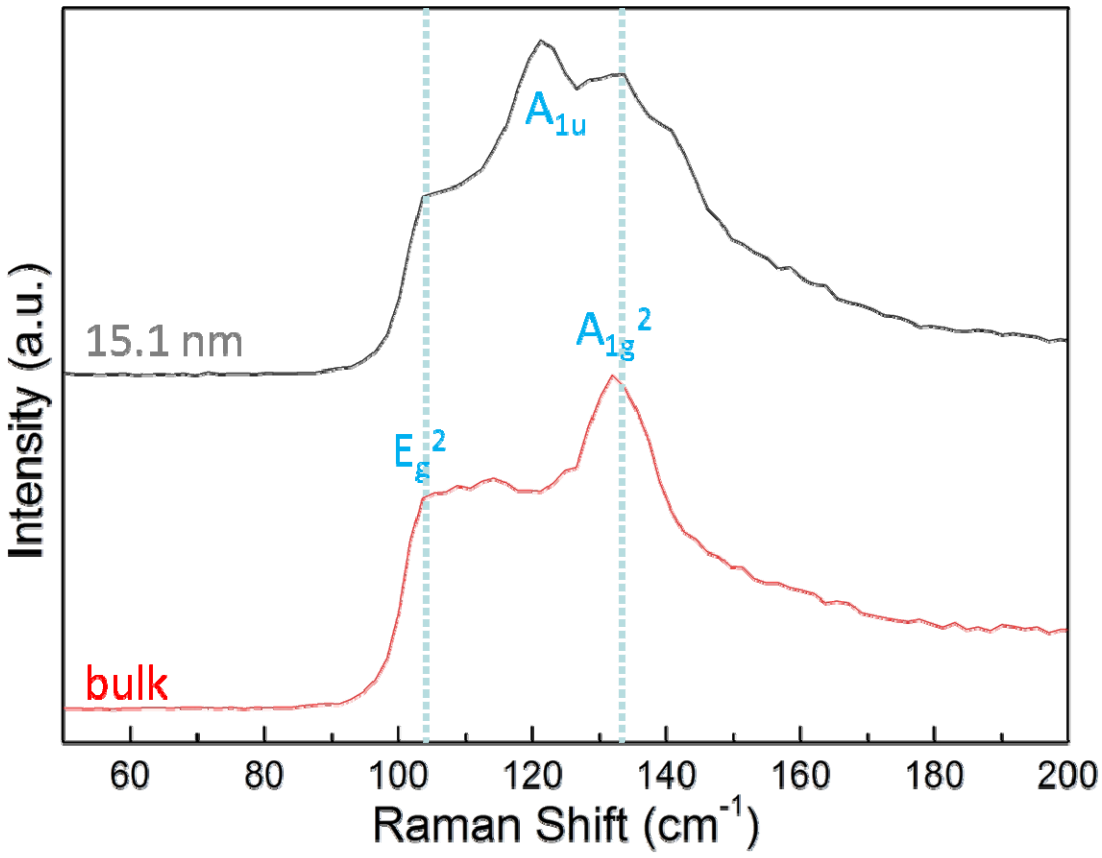

Figure 4.15. Raman spectra of bulk Bi_2Te_3 and ball-milled Bi_2Te_3 NCs.

CHAPTER 5. THERMOELECTRICS – THERMOELECTRIC PROPERTY CHARACTERIZATION OF NANOSTRUCTURED BULK HOT PRESSED FROM BISMUTH TELLURIDE-BASED NANOMATERIALS

The performance of thermoelectric materials is evaluated by a dimensionless parameter, figure of merit (ZT). ZT is defined as

$$ZT = \frac{S^2 \sigma T}{k}, \tag{5.1}$$

where S, σ, T, k represent the Seebeck coefficient, electrical conductivity, temperature and thermal conductivity, respectively. The product of S^2 and σ is called power factor. Basically, ZT increases with increasing Seebeck coefficient, electrical conductivity and temperature, but with decreasing thermal conductivity. A good material for thermoelectric applications should have high Seebeck coefficient, high electrical conductivity and low thermal conductivity. For decades, the ZT of bulk Bi_2Te_3-based alloys has been around 1 for not being able to further reduce thermal conductivity without significantly sacrificing the power factor. The nanoengineering method proposed by Poudel and coworkers points out a new approach to improve the ZT by increasing the number of grain boundaries in the material and has shown very promising results.[131] This chapter is dedicated to demonstrating the work we have done to implement the nanoengineering method into the fabrication of thermoelectric devices.

5.1 Experiments and Characterizations

5.1.1 Experiments

The first step of the nanoengineering method is to produce nanomaterials. Following that will be the fabrication of nanostructured bulk using the nanomaterials produced by wet-chemistry synthesis or ball milling. Nanostructured bulk is referred to as the bulk material with its grain size still remaining in the nanoscale. The purpose of this unique design is to decrease thermal conductivity by increasing phonon scattering occurring at grain boundaries. However, the electrical conductivity should not be sacrificed as a result of the grain size reduction. Therefore, the most critical part of the nanostructured bulk fabrication is to use an approach that can both densify the nanocrystals into bulk material and avoid any significant growth of the nanocrystals. Two approaches have been widely used to fabricate nanostructured bulk. They are hot pressing and spark plasma sintering (SPS). SPS is a sintering technique that combines pulsed DC current and uniaxial force to result in a fast consolidation of nanocrystals. The mechanism of SPS is still not very clear, but during SPS process, nanocrystals will densify into bulk material by going through plastic deformation and atom diffusion. There are several advantages of SPS that are beneficial for the nanostructured bulk fabrication. First, the density of the nanostructured bulk produced can be as high as 99% of the theoretical density because the plastic deformation and atom diffusion. Second, the growth of the nanocrystals can be suppressed to a large extent because of the short duration of the process. Third, the oxidation of the material can be avoided because of the vacuum or inert atmosphere used in the process.

Unlike the complex mechanism in SPS, hot pressing is more straightforward and simpler. Hot pressing can be performed on a hydraulic press machine with heating elements embedded in the upper and lower plates. During hot pressing process, nanocrystals are densified into bulk by the uniaxial force at moderate temperatures. There are several advantages of hot pressing that are beneficial for the nanostructured bulk fabrication. First, the density of the nanostructured bulk can be high because of the applied high uniaxial force. Second, the growth of the nanocrystals can be significantly suppressed because of the moderate temperature used in hot pressing.

Compared with SPS, hot pressing has some superior advantages. First, hot pressing equipment is cheaper and less complex than SPS equipment. Second, hot pressing does a better job in preserving the size of nanocrystals than SPS because of the relatively low process temperature. Here in our project, we mainly use hot pressing to fabricate nanostructured bulk from the nanocrystals.

Figure 5.1 shows a simple illustration of hot pressing method. Nanocrystal powders are first loaded into a stainless steel die very carefully to make sure the uniform material distribution. The die is then transported onto the hydraulic press machine and aligned with the center of the plate. Then pressure is eventually applied onto the die by the plates and heat is supplied to the die through the plates. The pressure and temperature will be maintained for some time and then eventually released. A nanostructured bulk pellet can be obtained after hot pressing. Pictures of nanocrystal powders and nanostructured bulk pellet are also shown in Figure 5.1.

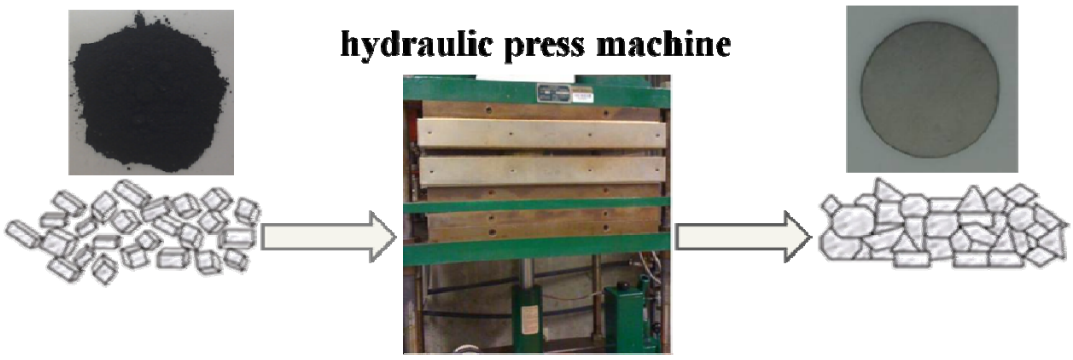

Figure 5.1. Illustration of hot pressing process.

5.1.2 Characterizations

SEM has been used to characterize the morphology of the nanostructured bulk. Samples for SEM are prepared by sticking the thinned pellet onto carbon tapes. SEM images are obtained on a Hitachi S-4800 Field Emission SEM with an accelerating voltage of 5 KV.

XRD has been used to characterize the crystal phase and average crystal size of the nanostructured bulk. Since nanostructured bulk is solid sample with a flat surface, no further preparation is needed. XRD patterns are obtained on a Bruker D8 Focus X-Ray Diffractometer with the theta-2theta scanning mode. The x-ray is from a Cu kα source with a wavelength of 0.154 nm. The scanning range of 2theta is set to be 20 – 65 degrees with an increment of 0.0256 degrees. The scanning speed is set to be 5 degrees/min.

Electrical conductivity is measured using a four-point probe method on a home-built probe station at room temperature. The probe station consists of a Micromanipulator 6000 in a dark box on top of a vibration isolation table. A Kiethley 4200 Semiconductor Parameter Analyzer is used to collect the data.

Seebeck coefficient is measured using MMR SB-100 Programmable Seebeck controller and MMR K-20 Programmable Temperature Controller from room temperature to 400 K. The heating rate is set to be 10 degrees/min.

Thermal conductivity measurement has been performed by an external company (TPRL, Inc.) from room temperature to 400 K. Thermal conductivity is written as

$$k = \alpha c_p \rho, \tag{5.2}$$

where α, c_p, and ρ represent thermal diffusivity, specific heat and volume mass density, respectively.

Volume mass density (ρ) is obtained by calculating the ratio of the sample's mass to volume.

Thermal diffusivity (α) is measured using the laser flash technique. The measurement system consists of a Korad K2 laser, a bell jar equipped with high-vacuum pumps, a tantalum or stainless steel tube heater surrounding a sample holding assembly, a thermocouple or an IR detector, appropriate biasing circuits, amplifiers, A/D converters, crystal clocks and a digital data acquisition system capable of accurately taking data in the 40 microsecond and longer time domain.

Specific heat (c_p) is measured using a standard Perkin-Elmer Model DSC-4 Differential Scanning Calorimeter with sapphire as the reference material. The heating rate of the sample is set to be 20 °C/min.

5.2 Results and Discussions

5.2.1 Effect of Thermal Annealing

In metallurgy, annealing is used to increase the ductility and release internal stresses of metals by heating them above some critical temperature, maintaining the temperature for

some time and then cooling it down to room temperature. During annealing, atom diffusion and rearrangement occur. These processes can occur at room temperature but will be greatly accelerated at elevated temperatures. Annealing is such a process that can facilitate diffusion and rearrangement by providing energies to break chemical bonds and helping atoms move to thermodynamically stable positions. Annealing can release the internal stresses and eliminate defects in materials and facilitate the formation of some material phase that is thermodynamically difficult to be formed at lower temperatures.

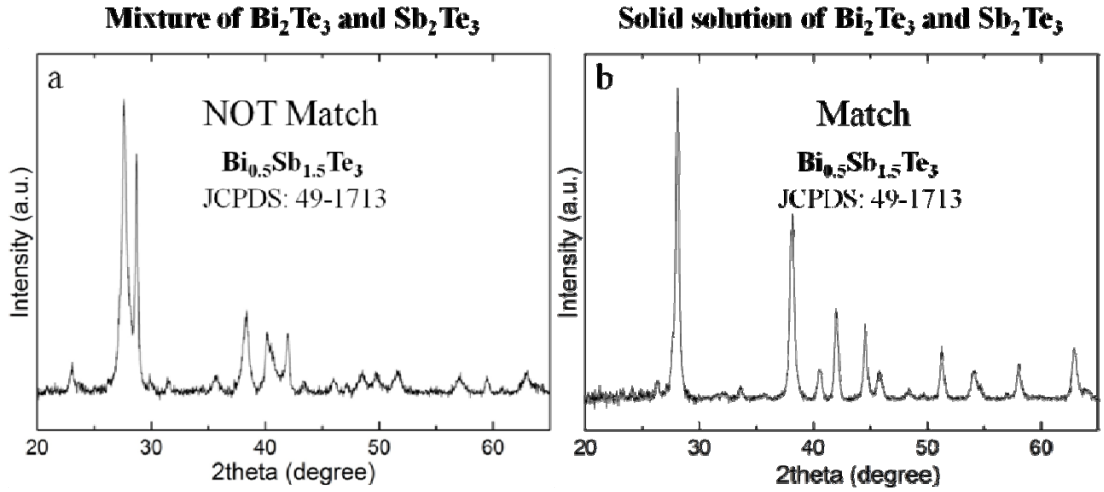

Figure 5.2. XRD patterns of Sb-doped Bi_2Te_3. (a) Before annealing, (b) After annealing.

Figure 5.2 shows the XRD patterns of Sb-doped Bi_2Te_3 before and after annealing. The doped Bi_2Te_3 is prepared by ball milling Bi_2Te_3, Sb and Te. For the purpose of clarification, their intensities have been normalized to the intensity of the strongest peaks. As seen in Figure 5.2a, there are two peaks existing around 27 degrees. These two peaks can be assigned to the (015) diffraction of Bi_2Te_3 and Sb_2Te_3, respectively. If the phase of $Bi_{0.5}Sb_{1.5}Te_3$ has been formed during the ball milling process, there should be only one peak existing around 27 degrees. The existence of two peaks means the separation of the

two phases, Bi_2Te_3 and Sb_2Te_3. Figure 5.2b shows the XRD pattern of the same sample that has been annealed at 400 °C for 1h. It can be seen that the original two peaks around 27 degrees have merged into one single peak. Furthermore, the diffraction pattern matches the standard diffraction record of $Bi_{0.5}Sb_{1.5}Te_3$, which indicates the formation of $Bi_{0.5}Sb_{1.5}Te_3$ phase after thermal annealing. In close contact with each other, atoms in Bi_2Te_3 and Sb_2Te_3 can gain enough energy to break the chemical bonds and diffuse into each other's lattice and result in a new phase of material. Further comparison between these two XRD patterns shows that the diffractions peaks become sharper and stronger after annealing. According to Scherrer equation, smaller full width at half maximum is induced by increase in crystal size. Therefore, thermal annealing can not only promote the phase formation but also grow the crystal grains. Crystal growth and phase formation both involve material diffusion, but crystal growth needs to overcome higher energy barriers because material atoms need to go through intergrain diffusion in crystal growth while only intragrain diffusion in phase formation.

Figure 5.3 shows XRD patterns and SEM images of the nanostructured bulk hot pressed from wet-chemistry synthesized Bi_2Te_3 NCs before and after annealing. The upper part shows the SEM images of three samples, before annealing, after annealing at 300 °C and 400 °C.

For the unannealed sample, at high magnification (200K), the surface is still very smooth and no clear crystal grain can be figured out in the image. It might be either because the grains are too small to see or because the grains are covered by amorphous organic ligands which don't emit enough secondary electrons for a clear image.

For the sample annealed at 300 °C, the surface becomes a little rougher and individual grains can be figured out in the image. Cracks and voids are showing up on the surface. The cracks and voids can be generated by the evaporation of organic ligands that used to reside on the surface of the nanocrystals. The sizes of the grains are still very small. It can be because of insignificant growth or no growth of grains at 300 °C. The reason why grains become visible after being annealed at 300 °C is partly because the evaporation of organic residues on the nanocrystal surface increase the number of secondary electrons that are emitted from the nanocrystals and used by the microscope to create a morphology-contrast based image. It's also clear that 300 °C can provide enough energy for organic residues to evaporate but not enough energy for crystal growth.

For the sample annealed at 400 °C, it is figured out that significant grain growth has occurred and the number of cracks and voids has increased. The increase in the number of cracks and voids can be induced by further evaporation of organic residues. The more thorough removal of organic ligands together with higher annealing temperature greatly promote the crystal grain growth by reducing the energy barrier for atoms to diffuse cross grain boundaries and providing more energies for material atom diffusion.

The lower part of Figure 5.3 shows the XRD patterns recorded on the three samples together with some quantitative analysis results. From bottom to top, the patterns correspond to unannealed sample, samples annealed at 300 °C and 400 °C, respectively. For the purpose of clarification, their intensities are normalized to the intensity of the (015) peak. From bottom to top, the full width at half maximum becomes smaller, indicating the increase in grain size. According to Scherrer equation, the estimated average crystal sizes for these three samples are 10.2 nm, 10.9 nm, and 18.8 nm,

respectively. The quantitative result agrees with the SEM image result that annealing at 300 °C can remove organic residues on the nanocrystal surface rather than promote the growth of the nanocrystals but annealing at 400 °C can both further remove organic residues and promote the growth of the nanocrystals.

Figure 5.4 shows the XRD patterns and SEM images of nanostructured bulk hot pressed from ball-milled NCs before and after annealing. The upper part shows the SEM images of two samples, before annealing, after annealing at 300 °C.

For the unannealed sample, unlike the unannealed sample hot pressed from wet-chemistry synthesized nanocrystals, small crystal grains can be clearly figured out in the SEM image. It can be because of two reasons. First, ball-milled nanocrystals are generally larger than wet-chemistry nanocrystals, which makes them easier to be seen under SEM. Second, since there are no organic ligands are used in ball milling, the surface of ball-milled nanocrystals is free of organic residues, which are known to emit fewer secondary electrons upon absorption of electrons and thus deteriorate the resolution of SEM images.

For the sample annealed at 300 °C, it is figured out that significant grain growth has already occurred. On the other hand, for the sample hot pressed from wet-chemistry synthesized nanocrystals, significant grain growth is not triggered until 400 °C. The reason for that can be attributed to the difference of the chemistry environments of the nanocrystal surfaces. Wet-chemistry synthesized nanocrystals are covered by a layer of organic ligands that are used to control the chemistry process in the synthesis, while ball-milled nanocrystals have fairly clean surface. In the hot pressed samples, ball-milled nanocrystals are in direct contact with each other and the energy that atoms need to

overcome can be easily achieved at 300 °C. As a result of that, significant crystal growth can occur at temperature as low as 300 °C.

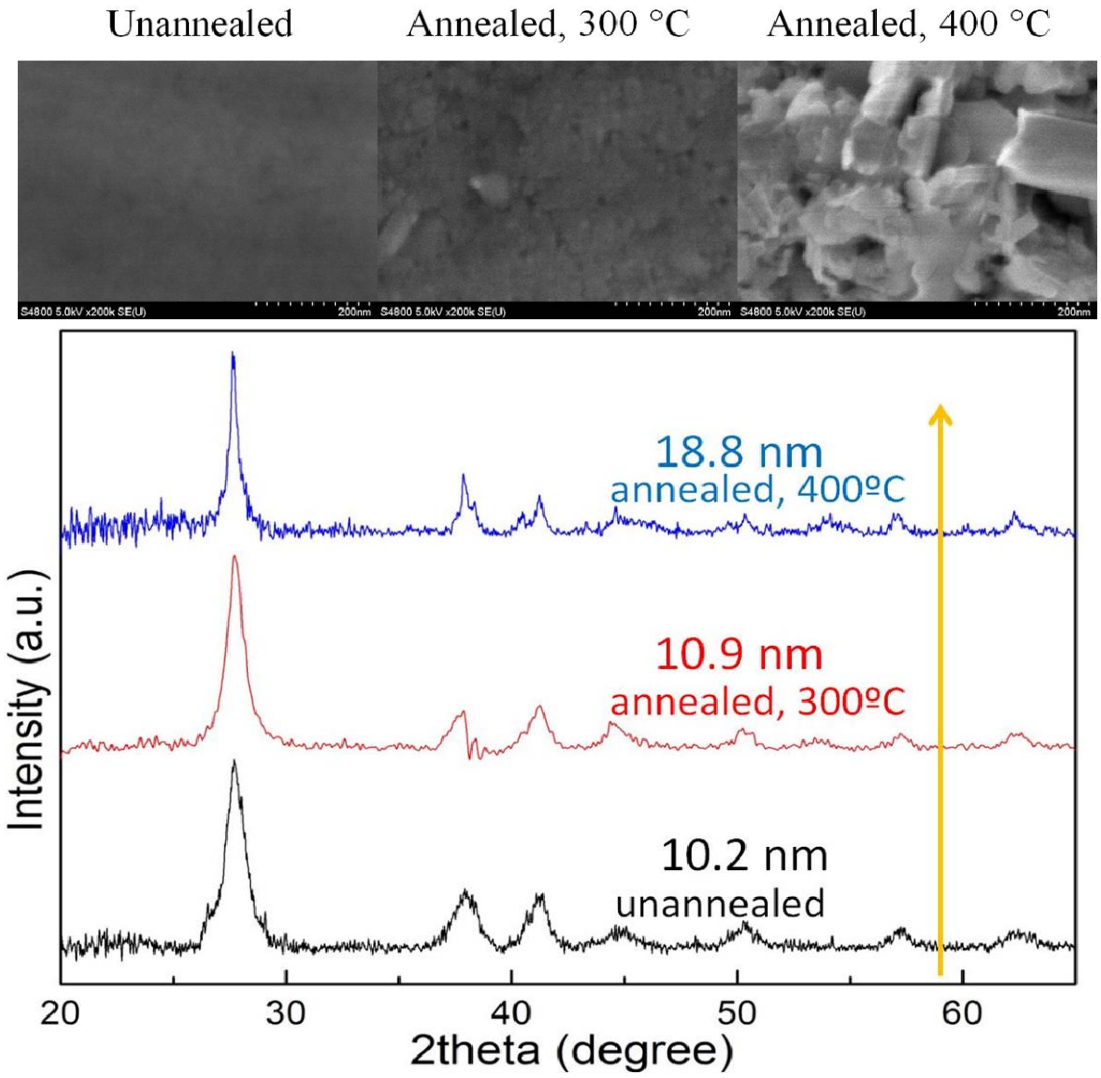

Figure 5.3. XRD patterns and SEM images of nanostructured bulk made from wet-chemistry synthesized Bi_2Te_3 NCs before and after annealing.

The lower part of Figure 5.4 shows the XRD patterns recorded on the two samples together with some quantitative analysis results. From bottom to top, the patterns correspond to unannealed sample, samples annealed at 300 °C, respectively. For the purpose of clarification, their intensities are normalized to the intensity of the strongest

peak. From bottom to top, the full width at half maximum becomes smaller, indicating the increase in grain size. According to Scherrer equation, the estimated average crystal sizes for these three samples are 21.7 nm, and 27.3 nm, respectively. The quantitative result confirms what has been observed in the SEM images.

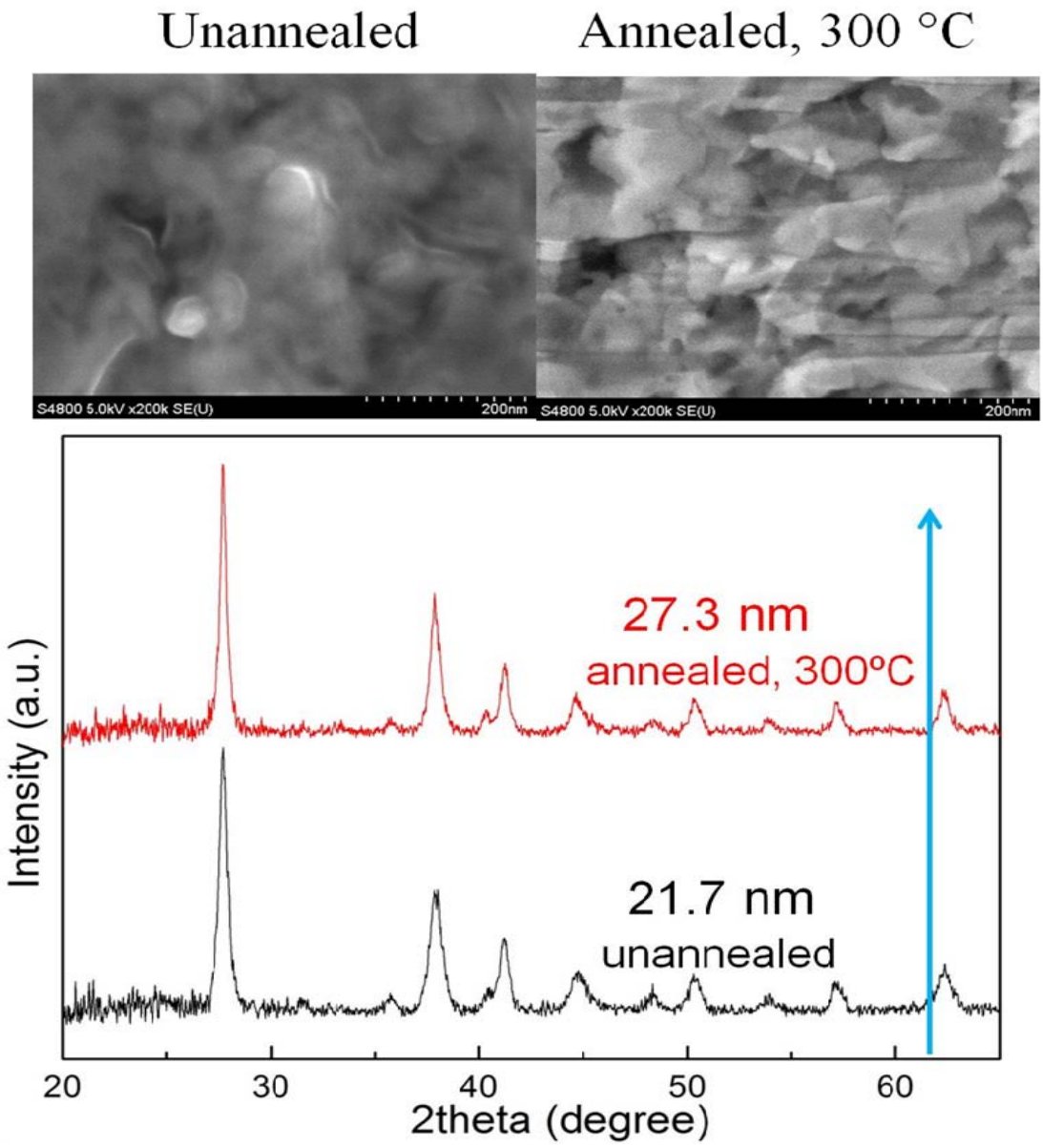

Figure 5.4. XRD patterns and SEM images of the nanostructured bulk made from ball-milled Bi_2Te_3 NCs before and after annealing.

Bi_2Te_3-based materials are sensitive to oxygen and can easily get oxidized when they are annealed in non-reducing atmosphere or low vacuum. Figure 5.5 shows the effect of annealing atmosphere on oxide formation of $Bi_{0.5}Sb_{1.5}Te_3$. From bottom to top, the XRD patterns correspond to unannealed sample, annealed sample, annealed and polished sample, respectively. The annealing is performed in argon atmosphere. The unannealed sample is composed of separate phases of Bi_2Te_3 and Sb_2Te_3. The annealing has facilitated the atom diffusion and resulted in a single phase of $Bi_{0.5}Sb_{1.5}Te_3$, but meanwhile the annealing has induced the oxidation process and generated an oxide phase of Bi, which can be figured out from the new peak around 26 degrees. After a layer of about 200 um thick has been polished off from the annealed sample, the oxide peak has been significantly reduced. This points out that the oxidation process starts from the surface and eventually proceeds from the outside layer to the inside layer and the oxygen source comes from the atmosphere rather than from the voids inside the sample.

5.2.2 Electrical Conductivity

Oxides are known to deteriorate the electrical conductivity of Bi_2Te_3-based materials.[131] Bi_2Te_3-based materials are sensitive to oxygen and oxide layer of 1.5 nm thick can easily grow at room temperature within 10 days at room temperature.[132] They are easier to be oxidized during nanocrystal preparation, hot pressing and thermal annealing because these processes are conducted at elevated temperatures. Annealing them in reducing-atmosphere can not only prevent them from being oxidized but also reduce the already-formed oxides. Compared with inert gas Ar, forming gas is more effective in prevent oxidation from occurring.

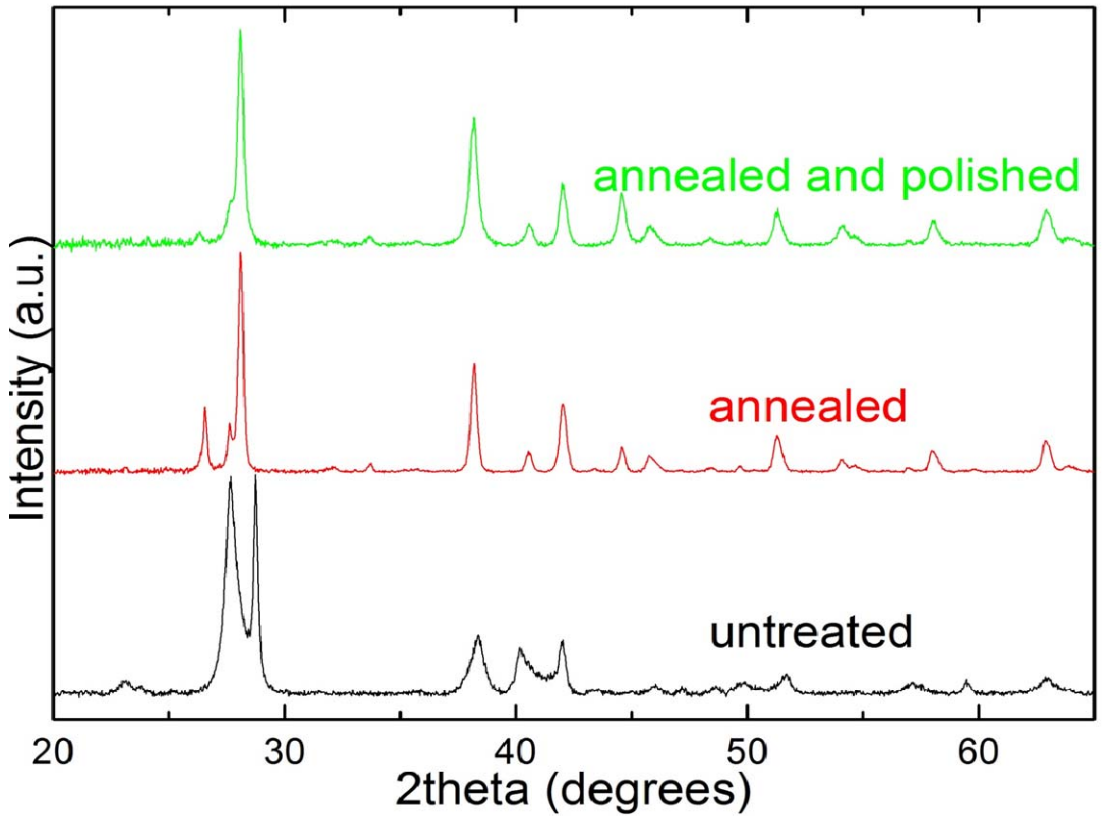

Figure 5.5. XRD patterns of annealed and unannealed $Bi_{0.5}Sb_{1.5}Te_3$ samples.

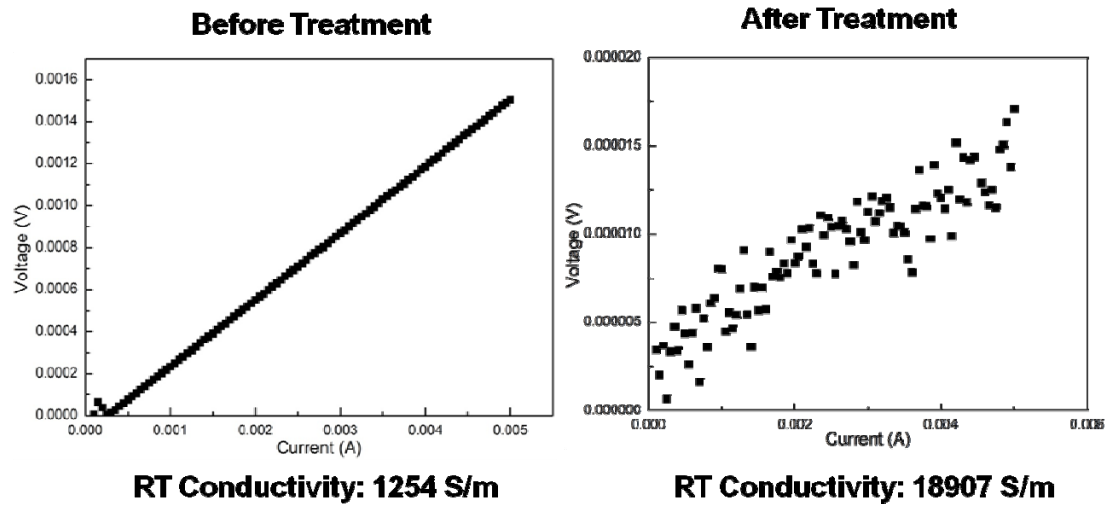

Figure 5.6.Typical I-V curve obtained on $Bi_{0.5}Sb_{1.5}Te_3$ samples before and after annealing in forming gas.

Figure 5.6 shows typical room-temperature I-V curves obtained on $Bi_{0.5}Sb_{1.5}Te_3$ samples before and after annealing in forming gas. The electrical conductivity measurement is set up according to Van der Pauw method. The calculated room-temperature electrical conductivity is 1254 S/m and 18907 S/m for the unannealed and annealed samples, respectively. It can be seen that annealing at 400 °C for 1h can greatly enhance the transport of charge carriers in the sample. This can be attributed to two reasons. First, annealing can improve the crystallinity of individual nanocrystals as well as the contact between neighboring nanocrystals. During annealing, atoms gain enough energy to diffuse to thermodynamically stable lattice sites and reduce the number of the defects within the nanocrystal, which improves the crystallinity and reduces the resistance to charge transport. Meanwhile, the atom diffusion also occurs between neighboring nanocrystals, which bridges the nanocrystals and increases the probability of intercrystal charge transport. Second, annealing can improve the contact between the material and metal electrode and reduce the contact resistance.[133] Post-metal-deposition annealing can facilitate the inter-penetration of metal atoms and material atoms and promote the formation of the electrically favorable phase of metal telluride. [134]

5.2.3 Seebeck Coefficient

The Seebeck effect is in the induction of electrical potential difference by a temperature difference in thermoelectric materials. Seebeck coefficient, also called thermoelectric power, measures materials' ability to generate a thermoelectric voltage upon the application of a temperature gradient across the materials. Seebeck coefficient has units of volts per kelvin (V/K), but μV/K is more commonly used. For degenerate

semiconductor materials or metals, there's an approximate relationship between the Seebeck coefficient and the charge carrier concentration,[135]

$$S \sim n^{-2/3}, \tag{5.3}$$

where n is the charge carrier concentration.

Figure 5.7 shows the Seebeck coefficient as a function of temperature for Bi_2Te_3 nanostructured bulk before and after annealing. These nanostructured bulk samples are hot pressed from ball-milled Bi_2Te_3 nanocrystals. From top to bottom, the plots correspond to unannealed sample, samples annealed at 300 °C and 400 °C, respectively. First, the Seebeck coefficients here all have a negative sign, indicating that the majority charge carriers in undoped Bi_2Te_3 nanocrystals are electrons. It can be figured out that the magnitude of Seebeck coefficient increases with increasing temperature in all three cases. The temperature dependence of Seebeck coefficient can be attributed to the temperature dependence of Fermi energy.[136] In metals, the Fermi energy is high and almost independent of temperature, but in semiconductors, the Fermi energy is low and is modified by temperature. Therefore, for semiconductors, their Seebeck coefficient increases with increasing temperature within low temperature range, and then decreases with increasing temperature within high temperature range, which is not shown here.

In Figure 5.7, the Seebeck coefficient result as a function of temperature is shown for three samples. It can be figured out that Seebeck coefficient increases after annealing and increases with increasing annealing temperature. The effect of annealing temperature on Seebeck coefficient can be explained by the influence of annealing temperature on charge carrier concentration. Annealing can influence the charge carrier concentration of Bi_2Te_3 samples in two ways.[137] First, annealing can reduce the number of defects, which are

the electron donors in Bi_2Te_3. Second, annealing can possibly induce the formation of bismuth oxide, which can result in an increase of hole concentration and an overall decrease of charge carrier concentration.

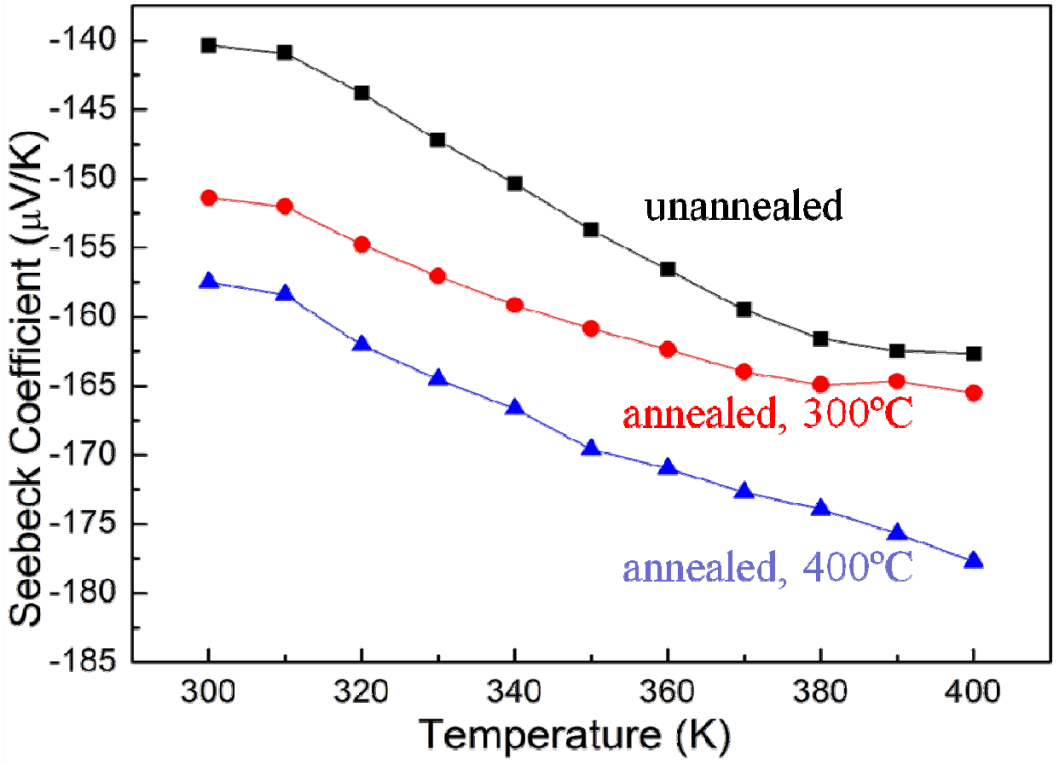

Figure 5.7. Seebeck coefficient as a function of temperature for Bi_2Te_3 samples before and after annealing.

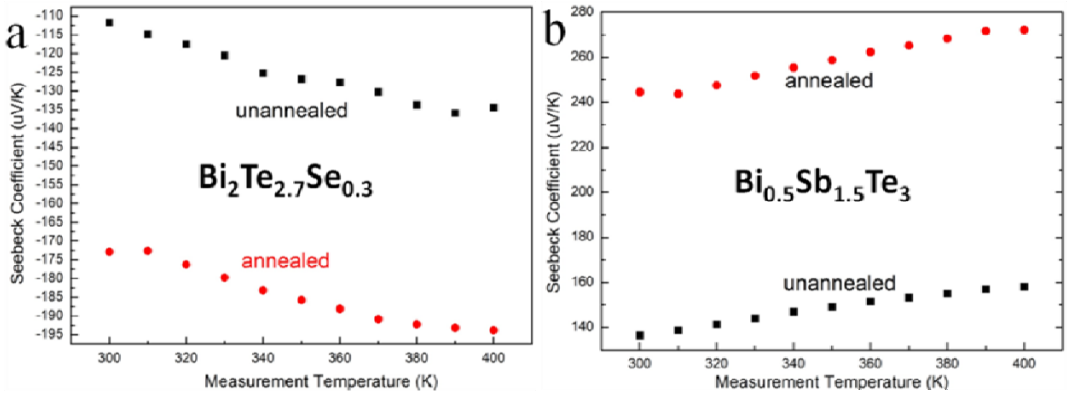

Figure 5.8. Seebeck coefficient as a function of temperature for doped Bi_2Te_3 samples. (a) $Bi_2Te_{2.7}Se_{0.3}$, (b) $Bi_{0.5}Sb_{1.5}Te_3$.

Figure 5.8 shows the Seebeck coefficient as a function of temperature for doped Bi_2Te_3 nanostructured bulk samples before and after annealing. The annealing conditions for both samples are 400 °C for 1h. In Figure 5.8(a), the negative sign of Seebeck coefficient indicates the formation of n-type semiconductor after Se doping in Bi_2Te_3. The magnitude of Seebeck coefficient increases with increasing temperature from 300 K to 400 K. There's a moderate increase of Seebeck coefficient after annealing, 60 μV/K. In Figure 5.8(b), the positive sign of Seebeck coefficient indicates the formation of p-type semiconductor after Sb doping in Bi_2Te_3. The magnitude of Seebeck coefficient increases with increasing temperature from 300 K to 400 K. Unlike the n-type material, there's a significant increase of Seebeck coefficient after annealing, 110 μV/K. Such dramatic influence of annealing temperature on Seebeck coefficient in Sb-doped Bi_2Te_3 can be attributed to the formation of single phase $Bi_{0.5}Sb_{1.5}Te_3$ after annealing. As shown in Figure 5.2(a), the unannealed sample is a mixture of Bi_2Te_3 and Sb_2Te_3, which are n-type and p-type semiconductor, respectively. The overall Seebeck coefficient is the difference of the Seebeck coefficients of the two phases, which are known to have different signs. However, the annealed sample, as shown in Figure 5.2(b), is composed of single-phase $Bi_{0.5}Sb_{1.5}Te_3$, which is known to be a p-type material. Therefore, there's no cancellation of Seebeck coefficients of different signs, which results in a drastic increase in overall Seebeck coefficient.

5.2.4 Thermal Conductivity

Thermal conductivity measures materials' capability to conduct heat. Heat transfers faster through materials with higher thermal conductivity than materials with lower thermal conductivity. Thermal conductivity has the unit of watts per meter kelvin.

Figure 5.9 shows the thermal conductivity as a function of temperature for two samples hot pressed from wet-chemistry synthesized Bi_2Te_3 nanocrystals. The upper plot corresponds to the sample with an average crystal size of 11.4 nm, and the lower plot corresponds to the sample with an average crystal size of 8.2 nm.

The thermal conductivity in semiconductors is contributed by the transport of charge carriers and phonons. The contribution from phonons is also called lattice thermal conductivity k_l, which is defined as

$$k_l = (1/3)\, v_s^2 \tau c, \tag{5.4}$$

where v_s, τ and c represents sound velocity, effective phonon relaxation time and specific heat, respectively[67].

In Figure 5.9, it can be seen that thermal conductivity increases with temperature for both samples. This can be explained by the increase of electronic contribution to the overall thermal conductivity. The charge carrier concentration increases with increasing temperature because of the decreased bandgap of semiconductor nanocrystals and the increased energy supplied to electrons in the valence band with increasing temperature.[40] The increase in charge carrier concentration increases the amount of heat that can be conducted by charge carriers and thus increase the thermal conductivity of the material.

In Figure 5.9, a clear dependence of the thermal conductivity on the crystal size can be figured out. The room-temperature thermal conductivity of bulk Bi_2Te_3 is around 2.2 W/m·K. The room-temperature thermal conductivities of 11.4-nm sample and 8.2-nm sample are only 0.23 W/m·K and 0.185 W/m·K respectively. This can be explained in two ways, the reduction of electronic thermal conductivity and lattice thermal conductivity with decreasing the grain size.

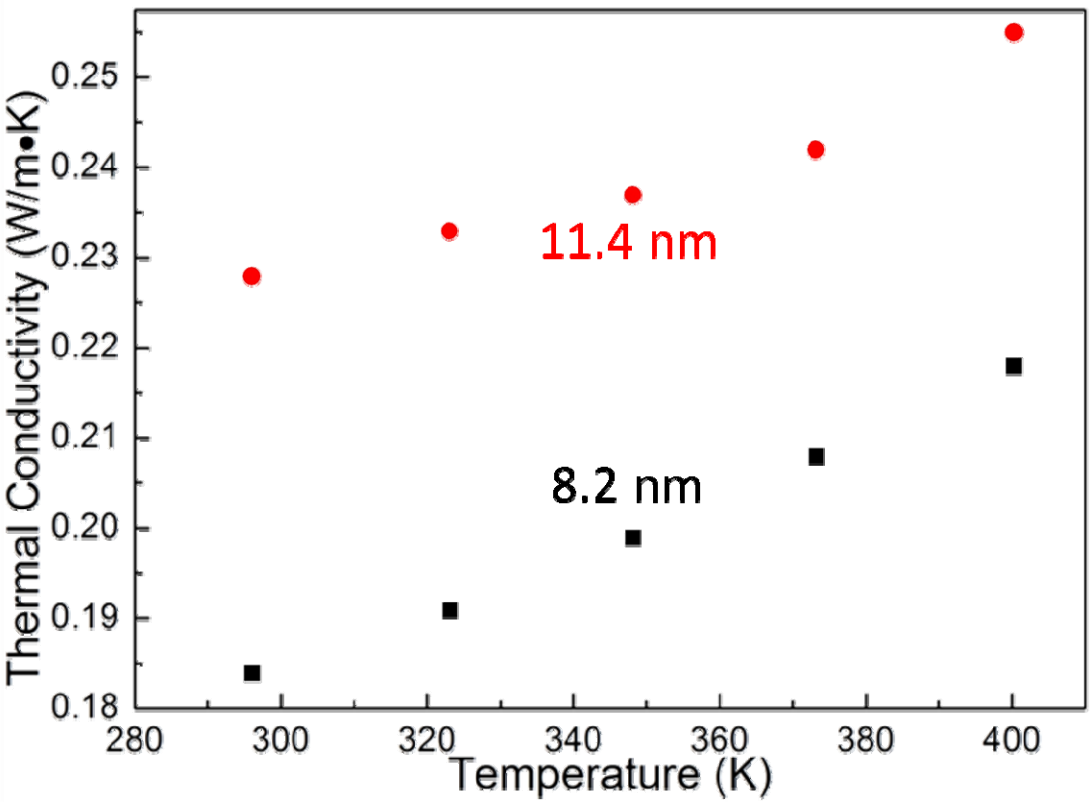

Figure 5.9. Thermal conductivity as a function of temperature for nanostructured bulk samples hot pressed from wet-chemistry synthesized nanocrystals.

First, according to Equation 5.4, the lattice thermal conductivity decreases with decreasing phonon relaxation time. Compared with bulk material, nanostructured bulk material is composed of small grains with nanoscale sizes. This nanostructure will

increase the scattering of phonons at grain boundaries and thus decrease the phonon mean free and decrease the relaxation time of phonons. Therefore, it is reasonable that lattice thermal conductivity decreases with decreasing grain size in nanostructured bulk samples.

Second, according to quantum confinement theory, the bandgap of semiconductor nanocrystals increases with decreasing the nanocrystal size. In smaller nanocrystals, more energies will be needed to excite electrons from valence band to conduction band and therefore fewer electrons will be excited and become available for conducting heat.

5.2.5 Figure of Merit

Table 5.1 shows a summary of room-temperature thermoelectric properties measured on the n-type $Bi_2Te_{2.7}Se_{0.3}$ sample as well as the state-of-the-art values[138]. The sample is hot pressed from ball-milled nanocrystals. By optimizing the parameters of hot pressing and subsequent treatments, the room-temperature figure of merit of n-type $Bi_2Te_{2.7}Se_{0.3}$ is around 0.32, which is quite lower than the state-of-the-art value 0.9. This is mainly because our electrical conductivity is almost 10 times lower.

Table 5.2 shows a summary of room-temperature thermoelectric properties measured on the p-type $Bi_{0.5}Sb_{1.5}Te_3$ sample as well as the state-of-the-art values[131]. For our p-type sample, the figure of merit result is much more exciting. The room-temperature figure of merit value is around 1.24, which has exceeded the value 1.18 reported in Gang Chen's Science paper[131] and is among the few highest values that have been achieved so far. The improvement in figure of merit mainly arises from the drastic reduction in thermal conductivity, which can be attributed to decreased lattice thermal conductivity from increased number of grain boundaries and defects.

Meanwhile, it is also noticed that our electrical conductivity value is lower than the values reported in the two literature papers. So far we have seen low electrical conductivity in both our n and p type samples. This is probably because of the relatively low densities of the hot pressed samples. We can either increase the pressure used in hot pressing or switch from hot pressing to spark plasma sintering. Further research is under way.

Table 5.1. Summary of room-temperature thermoelectric properties of n-type $Bi_2Te_{2.7}Se_{0.3}$ and the state-of-the-art values.

Sample Name	$Bi_2Te_{2.7}Se_{0.3}$	state of the art[138]
Temperature (K)	300	300
Electrical Conductivity (S/m)	9730	96500
Seebeck Coefficient (V/K)	0.000173	0.000189
Thermal Conductivity (W/m·K)	0.272	1.17
Figure of Merit	0.32	0.9

Table 5.2. Summary of room-temperature thermoelectric properties of p-type $Bi_{0.5}Sb_{1.5}Te_3$ and the state-of-the-art values.

Sample Name	$Bi_{0.5}Sb_{1.5}Te_3$	state of the art[131]
Temperature (K)	300	300
Electrical Conductivity (S/m)	9730	96500
Seebeck Coefficient (V/K)	0.000173	0.000189
Thermal Conductivity (W/m·K)	0.272	1.17
Figure of Merit	0.32	0.9

CHAPTER 6. SUMMARY AND FUTURE PLANS

6.1 Material Synthesis and Characterization

In our synthesis, monodisperse CdSe, PbSe, and PbTe nanocrystals of various morphologies have been synthesized by using different combinations of surfactant and solvent in the refined phosphonic-acid-assisted organometallic method.

Post-synthesis treatment like size selective precipitation is usually needed to narrow the size distribution. However, it is found in our work that by controlling the synthesizing conditions more precisely, nearly monodisperse NCs can be readily synthesized.

For the characterization, XRD spectra confirm the formation of desired crystal structures and TEM images confirm the morphology and crystallinity of as-prepared nanocrystals. Visible absorption spectra show that absorption peak shifts to longer wavelength with increasing the nanocrystal size.

Bi_2Te_3 nanocrystals have been produced by both organometallic and ball-milling methods.

Two mechanisms are observed in the wet-chemistry growth process of semiconductor nanocrystals: addition of monomers and fusion of small crystals. A typical material growing by addition of monomers is CdSe. Typical materials growing by fusion of small crystals include Bi_2Te_3 and PbSe.

Raman spectroscopy has been used to investigate the size, shape and temperature dependence of phonon vibrational modes. For CdSe nanocrystals, the LO-phonon frequency decreases and bandwidth increases with increasing the temperature or decreasing the size. The analysis of 0D samples shows that the influence of diameter is dominant over that of shape and the temperature sensitivity increases with increasing the diameter. On the other hand, the comparison between 0D and 1D samples shows that temperature sensitivity decreases with increasing the dimension along the c-axis.

The 2D nanostructure shows similar Raman features as those of few-quintuple-thick Bi_2Te_3 layers, while the 0D and 1D nanostructures show a blue-shifted A_{1g}^2 mode and a much stronger A_{1u} mode, which is the first report regarding the morphology impact on the Raman modes of Bi_2Te_3 nanocrystals.

For thermoelectric applications, nanostructured bulk approach has been adopted to improve the figure of merit of Bi_2Te_3 based alloys. Due to the increased phonon scattering at the grain boundaries introduced in nanostructured bulk process, significantly reduced thermal conductivities have been observed in nanostructured bulk Bi_2Te_3 samples fabricated by hot-pressing method. It is also observed that thermal conductivity decreases with decreasing the average grain size. Several post-fabrication treatments, like removal of surface oxide layer by Ar plasma and hydrazine and thermal annealing, have further improved the thermoelectric properties of the samples. The room-temperature figure of merit values obtained on n-type $Bi_2Te_{2.7}Se_{0.3}$ and p-type $Bi_{0.5}Sb_{1.5}Te_3$ are around 0.32 and 1.23, respectively. The n-type value is still lower than the state-of-the-art value, but the p-type value is among the highest values that have been obtained so far. Certain property, like the electrical conductivity, has been found to be consistently way lower

than the state-of-the-art value, so further efforts should be emphasized to identify the root causes and improving them.

6.2 Phonon-Assisted Hot Electron Decay

We have used the time-domain DFT and NAMD to study the phonon-assisted hot electron relaxation dynamics in the CdSe QD and EQD. The electronic DOS shows shape-dependent features. The band gap is narrower and electron and hole states are denser in the EQD than in the QD. The band gap shows negative temperature dependence for both QD and EQD. The temperature dependence is stronger for EQD. By taking the Fourier transforms of the LUMO energies, the electron-phonon coupling spectra were also evaluated. At higher temperatures, higher-frequency phonon modes are induced to scatter with electrons for both QD and EQD. The electron-phonon coupling is stronger in the EQD than in the QD, which favors a generally faster relaxation in the EQD. The hot electron decay rate shows a weaker temperature dependence than expected for both QD and EQD. This could be attributed to the negative temperature dependence of the electron-phonon coupling term $|\mathbf{d}_{\mathbf{km}}|$. The hot electron decay rate is higher and shows a stronger temperature dependence in the EQD than in the QD. In all, our work shows that the shapes of NCs can affect the optical and electronic properties of the NCs through modifications of their electronic structure. The results presented in this paper can help to understand the fundamental mechanisms of hot electron relaxation dynamics in NCs and to guide future experiments.

6.3 Future Plan

For thermoelectric applications, future efforts will be dedicated to further improving the figure of merit by increasing the electrical conductivity and Seebeck coefficient and

decreasing the thermal conductivity. Promising approaches include treating nanocrystals with hydrazine and ion bombarding the surface of the nanostructure bulk samples. Hydrazine treatment can remove oxides and insulating organic ligands from the surface of the nanocrystals, and ion bombardment can effective remove oxides from the surface of the pellet sample and improve the contact between metal electrodes and the material. These two approaches together are supposed to increase the electrical conductivity of the sample.

For photovoltaic applications, future efforts will be dedicated to fabricating high-efficiency semiconductor solar cell devices and gaining a better understanding of the interaction between phonons and electrons in semiconductor materials.

LIST OF REFERENCES

LIST OF REFERENCES

[1] Nozik AJ. Spectroscopy and hot electron relaxation dynamics in semiconductor quantum wells and quantum dots. Annual Review of Physical Chemistry. 2001;52:193-231.

[2] Nelson J. The physics of solar cells. London: Imperial College Press; 2003.

[3] Prezhdo OV. Multiple excitons and the electron-phonon bottleneck in semiconductor quantum dots: An ab initio perspective. Chemical Physics Letters. 2008;460:1-9.

[4] Murray CB, Norris DJ, Bawendi MG. Synthesis and characterization of nearly monodisperse CdE (E = S, Se, Te) semiconductor nanocrystallites. Journal of the American Chemical Society. 1993;115:8706-15.

[5] Kuno M, Lee JK, Dabbousi BO, Mikulec FV, Bawendi MG. The band edge luminescence of surface modified CdSe nanocrystallites: Probing the luminescing state. Journal of Chemical Physics. 1997;106:9869-82.

[6] Kalyuzhny G, Murray RW. Ligand effects on optical properties of CdSe nanocrystals. Journal of Physical Chemistry B. 2005;109:7012-21.

[7] Kwak WC, Kim TG, Chae WS, Sung YM. Tuning the energy bandgap of CdSe nanocrystals via Mg doping. Nanotechnology. 2007;18.

[8] Sliem MA, Chemseddine A, Bloeck U, Fischer RA. PbSe nanocrystal shape development: oriented attachment at mild conditions and microwave assisted growth of nanocubes. Crystengcomm. 2011;13:483-8.

[9] Choi JJ, Lim YF, Santiago-Berrios MB, Oh M, Hyun BR, Sung LF, et al. PbSe Nanocrystal excitonic solar cells. Nano Letters. 2009;9:3749-55.

[10] Koleilat GI, Levina L, Shukla H, Myrskog SH, Hinds S, Pattantyus-Abraham AG, et al. Efficient, stable infrared photovoltaics based on solution-cast colloidal quantum dots. Acs Nano. 2008;2:833-40.

[11] Zheng Z, Zhao L, Wang M, Liu M, Marcus MS, Liu Y, et al. High efficiency CdSe quantum-dot sensitized solar cells. 35th Ieee Photovoltaic Specialists Conference2010.

[12] Guyot-Sionnest P, Wehrenberg B, Yu D. Intraband relaxation in CdSe nanocrystals and the strong influence of the surface ligands. Journal of Chemical Physics. 2005;123.

[13] Jarosz MV, Porter VJ, Fisher BR, Kastner MA, Bawendi MG. Photoconductivity studies of treated CdSe quantum dot films exhibiting increased exciton ionization efficiency. Physical Review B. 2004;70.

[14] Gur I, Fromer NA, Geier ML, Alivisatos AP. Air-stable all-inorganic nanocrystal solar cells processed from solution. Science. 2005;310:462-5.

[15] Yu WW, Qu LH, Guo WZ, Peng XG. Experimental determination of the extinction coefficient of CdTe, CdSe and CdS nanocrystals. Chemistry of Materials. 2004;16:560-5.

[16] Guyot-Sionnest P, Shim M, Matranga C, Hines M. Intraband relaxation in CdSe quantum dots. Physical Review B. 1999;60:R2181-R4.

[17] Schaller RD, Pietryga JM, Goupalov SV, Petruska MA, Ivanov SA, Klimov VI. Breaking the phonon bottleneck in semiconductor nanocrystals via multiphonon emission induced by intrinsic nonadiabatic interactions. Physical Review Letters. 2005;95:196401.

[18] Cooney RR, Sewall SL, Anderson KEH, Dias EA, Kambhampati P. Breaking the phonon bottleneck for holes in semiconductor quantum dots. Physical Review Letters. 2007;98:177403.

[19] Hendry E, Koeberg M, Wang F, Zhang H, Donega CD, Vanmaekelbergh D, et al. Direct observation of electron-to-hole energy transfer in CdSe quantum dots. Physical Review Letters. 2006;96:4.

[20] An JM, Califano M, Franceschetti A, Zunger A. Excited-state relaxation in PbSe quantum dots. Journal of Chemical Physics. 2008;128:7.

[21] Guyot-Sionnest P, Wehrenberg B, Yu D. Intraband relaxation in CdSe nanocrystals and the strong influence of the surface ligands. Journal of Chemical Physics. 2005;123:074709.

[22] Urayama J, Norris TB, Singh J, Bhattacharya P. Observation of phonon bottleneck in quantum dot electronic relaxation. Physical Review Letters. 2001;86:4930-3.

[23] Yoffe AD. Semiconductor quantum dots and related systems: electronic, optical, luminescence and related properties of low dimensional systems. Advances in Physics. 2001;50:1-208.

[24] Pandey A, Guyot-Sionnest P. Slow electron cooling in colloidal quantum dots. Science. 2008;322:929-32.

[25] Schaller RD, Klimov VI. High efficiency carrier multiplication in PbSe nanocrystals: Implications for solar energy conversion. Physical Review Letters. 2004;92:186601.

[26] Nozik AJ. Nanoscience and nanostructures for photovoltaics and solar fuels. Nano Letters. 2010;10:2735-41.

[27] Nozik AJ, Beard MC, Luther JM, Law M, Ellingson RJ, Johnson JC. Semiconductor quantum dots and quantum dot arrays and applications of multiple exciton generation to third-generation photovoltaic solar cells. Chemical Reviews. 2010;110:6873-90.

[28] Rabani E, Baer R. Distribution of Multiexciton Generation rates in CdSe and InAs nanocrystals. Nano Letters. 2008;8:4488-92.

[29] Ellingson RJ, Beard MC, Johnson JC, Yu PR, Micic OI, Nozik AJ, et al. Highly efficient multiple exciton generation in colloidal PbSe and PbS quantum dots. Nano Letters. 2005;5:865-71.

[30] Witzel WM, Shabaev A, Hellberg CS, Jacobs VL, Efros AL. Quantum simulation of multiple-exciton generation in a nanocrystal by a single photon. Physical Review Letters. 2010;105:137401.

[31] Prezhdo OV. Photoinduced Dynamics in Semiconductor Quantum Dots: Insights from Time-Domain ab Initio Studies. Accounts of Chemical Research. 2009;42:2005-16.

[32] Yu PR, Nedeljkovic JM, Ahrenkiel PA, Ellingson RJ, Nozik AJ. Size dependent femtosecond electron cooling dynamics in CdSe quantum rods. Nano Letters. 2004;4:1089-92.

[33] Mohamed MB, Burda C, El-Sayed MA. Shape dependent ultrafast relaxation dynamics of CdSe nanocrystals: Nanorods vs nanodots. Nano Letters. 2001;1:589-93.

[34] Craig CF, Duncan WR, Prezhdo OV. Trajectory surface hopping in the time-dependent Kohn-Sham approach for electron-nuclear dynamics. Physical Review Letters. 2005;95:163001.

[35] Sean A. Fischer BFH, Angeline B. Madrid, Walter R. Duncan, and Oleg V. Prezhdo. Regarding the validity of the time-dependent Kohn–Sham approach for electron-nuclear dynamics via trajectory surface hopping. Journal of Chemical Physics. 2011;134:024102.

[36] Kilina SV, Craig CF, Kilin DS, Prezhdo OV. Ab initio time-domain study of phonon-assisted relaxation of charge carriers in a PbSe quantum dot. Journal of Physical Chemistry C. 2007;111:4871-8.

[37] Hyeon-Deuk K, Madrid AB, Prezhdo OV. Symmetric band structures and asymmetric ultrafast electron and hole relaxations in silicon and germanium quantum dots: time-domain ab initio simulation. Dalton Transactions. 2009:10069-77.

[38] Kilina SV, Kilin DS, Prezhdo OV. Breaking the phonon pottleneck in PbSe and CdSe quantum dots: time-domain density functional theory of charge carrier relaxation. Acs Nano. 2009;3:93-9.

[39] Bao H, Habenicht BF, Prezhdo OV, Ruan XL. Temperature dependence of hot-carrier relaxation in PbSe nanocrystals: An ab initio study. Physical Review B. 2009;79:235306.

[40] Chen LL, Bao H, Tan TZ, Prezhdo OV, Ruan XL. Shape and temperature dependence of hot carrier relaxation dynamics in spherical and elongated CdSe quantum dots. Journal of Physical Chemistry C. 2011;115:11400-6.

[41] Alivisatos AP, Harris TD, Brus LE, Jayaraman A. Resonance Raman-scattering and optical-absorption studies of Cdse microclusters at high-pressure. Journal of Chemical Physics. 1988;89:5979-82.

[42] Tanaka A, Onari S, Arai T. Raman-scattering from CdSe microcrystals embedded in a germanate glass matrix. Physical Review B. 1992;45:6587-92.

[43] Hwang YN, Shin SH, Park HL, Park SH, Kim U, Jeong HS, et al. Effect of lattice contraction on the Raman shifts of CdSe quantum dots in glass matrices. Physical Review B. 1996;54:15120-4.

[44] Ingale A, Rustagi KC. Raman spectra of semiconductor nanoparticles: Disorder-activated phonons. Physical Review B. 1998;58:7197-204.

[45] Trallero-Giner C, Debernardi A, Cardona M, Menendez-Proupin E, Ekimov AI. Optical vibrons in CdSe dots and dispersion relation of the bulk material. Physical Review B. 1998;57:4664-9.

[46] Zhang JY, Wang XY, Xiao M, Qu L, Peng X. Lattice contraction in free-standing CdSe nanocrystals. Applied Physics Letters. 2002;81:2076-8.

[47] Neeleshwar S, Chen CL, Tsai CB, Chen YY, Chen CC, Shyu SG, et al. Size-dependent properties of CdSe quantum dots. Physical Review B. 2005;71.

[48] Dzhagan VM, Valakh MY, Raevskaya AE, Stroyuk AL, Kuchmiy SY, Zahn DRT. Size effects on Raman spectra of small CdSe nanoparticles in polymer films. Nanotechnology. 2008;19.

[49] Nien YT, Zaman B, Ouyang J, Chen IG, Hwang CS, Yu K. Raman scattering for the size of CdSe and CdS nanocrystals and comparison with other techniques. Materials Letters. 2008;62:4522-4.

[50] Vinogradov VS, Karczewski G, Kucherenko IV, Mel'nik NN, Fernandez P. Raman spectra of structures with CdTe-, ZnTe-, and CdSe-based quantum dots and their relation to the fabrication technology. Physics of the Solid State. 2008;50:164-7.

[51] Hugall JT, Baumberg JJ, Mahajan S. Surface-enhanced Raman spectroscopy of CdSe quantum dots on nanostructured plasmonic surfaces. Applied Physics Letters. 2009;95.

[52] Mohr M, Thomsen C. Phonons in bulk CdSe and CdSe nanowires. Nanotechnology. 2009;20:115707.

[53] Wang C, Jiang Y, Chen LL, Li SY, Li GH, Zhang ZP. Temperature dependence of optical properties and size tunability CdSe quantum dots via non-TOP synthesis. Materials Chemistry and Physics. 2009;116:388-91.

[54] Tanaka A, Onari S, Arai T. Raman scattering from CdSe microcrystals embedded in a germanate glass matrix. Physical Review B. 1992;45:6587-92.

[55] Meulenburg RW. Compressive and tensile stress in colloidal CdSe semiconductor quantum dot. Physical Review B. 2004;70.

[56] Kusch P, Lange H, Artemyev M, Thomsen C. Size-dependence of the anharmonicities in the vibrational potential of colloidal CdSe nanocrystals. Solid State Communications. 2011;151:67-70.

[57] Dzhagan VM, Valakh MY, Raevskaya AE, Stroyuk AL, Kuchmiy SY, Zahn DRT. Temperature-dependent resonant Raman scattering study of core/shell nanocrystals - art. no. 012045. In: Perrin B, Bonello B, Devos A, Duquesne JY, Rossignol C, editors. 12th International Conference on Phonon Scattering in Condensed Matter2007. p. 12045.

[58] Song L, Ma WJ, Ren Y, Zhou WY, Xie SS, Tan PH, et al. Temperature dependence of Raman spectra in single-walled carbon nanotube rings. Applied Physics Letters. 2008;92.

[59] Calizo I, Balandin AA, Bao W, Miao F, Lau CN. Temperature dependence of the Raman spectra of graphene and graphene multilayers. Nano Letters. 2007;7:2645-9.

[60] Rowe DM, Bhandari CM. Modern Thermoelectrics. Holt, Rinehart&Winston, London. 1983.

[61] Rowe DM. Thermoelectrics Handbook: Macro to Nano. illustrated ed: CRC Press, Boca Raton; 1995.

[62] Chen G, Shakouri A. Heat transfer in nanostructures for solid-state energy conversion. Journal of Heat Transfer-Transactions of the Asme. 2002;124:242-52.

[63] Hicks LD, Dresselhaus MS. Thermoelectric figure of merit of a one-dimensional conductor. Physical Review B. 1993;47:16631-4.

[64] Hicks LD, Dresselhaus MS. Effect of quantum-well structures on the thermoelectric figure of merit. Physical Review B. 1993;47:12727-31.

[65] Zhao L-D, Zhang B-P, Liu W-S, Li J-F. Effect of mixed grain sizes on thermoelectric performance of Bi(2)Te(3) compound. Journal of Applied Physics. 2009;105.

[66] Mavrokefalos A, Moore AL, Pettes MT, Shi L, Wang W, Li X. Thermoelectric and structural characterizations of individual electrodeposited bismuth telluride nanowires. Journal of Applied Physics. 2009;105.

[67] Qiu B, Sun L, Ruan X. Lattice thermal conductivity reduction in Bi(2)Te(3) quantum wires with smooth and rough surfaces: a molecular dynamics study. Physical Review B. 2011;83.

[68] Zhao Y, Hughes RW, Su Z, Zhou W, Gregory DH. One-step synthesis of bismuth telluride nanosheets of a few quintuple layers in thickness. Angewandte Chemie-International Edition. 2011;50:10397-401.

[69] Teweldebrhan D, Goyal V, Rahman M, Balandin AA. Atomically-thin crystalline films and ribbons of bismuth telluride. Applied Physics Letters. 2010;96.

[70] Teweldebrhan D, Goyal V, Balandin AA. Exfoliation and characterization of bismuth telluride atomic quintuples and quasi-two-dimensional crystals. Nano Letters. 2010;10:1209-18.

[71] Russo V, Bailini A, Zamboni M, Passoni M, Conti C, Casari CS, et al. Raman spectroscopy of Bi-Te thin films. Journal of Raman Spectroscopy. 2008;39:205-10.

[72] Lu WG, Fang JY, Ding Y, Wang ZL. Formation of PbSe nanocrystals: a growth toward nanocubes. Journal of Physical Chemistry B. 2005;109:19219-22.

[73] Park J, Lee KH, Galloway JF, Searson PC. Synthesis of cadmium selenide quantum dots from a non-coordinating solvent: growth kinetics and particle size distribution. Journal of Physical Chemistry C. 2008;112:17849-54.

[74] Wang X, Li K, Dong Y, Jiang K. Preparation and characterization of monodispersed PbSe nanocubes. Crystal Research and Technology. 2010;45:94-8.

[75] Liu Y, Qiu HY, Xu Y, Wu D, Li MJ, Jiang JX, et al. Selective synthesis of wurtzite CdSe nanorods and zinc blend CdSe nanocrystals through a convenient solvothermal route. Journal of Nanoparticle Research. 2007;9:745-52.

[76] Ge JP, Li YD, Yang GQ. Mechanism of aqueous ultrasonic reaction: controlled synthesis, luminescence properties of amorphous cluster and nanocrystalline CdSe. Chemical Communications. 2002:1826-7.

[77] Zhu JJ, Palchik O, Chen SG, Gedanken A. Microwave assisted preparation of CdSe, PbSe, and Cu2-xSe nanoparticles. Journal of Physical Chemistry B. 2000;104:7344-7.

[78] Deng ZT, Cao L, Tang FQ, Zou BS. A new route to zinc-blende CdSe nanocrystals: Mechanism and synthesis. Journal of Physical Chemistry B. 2005;109:16671-5.

[79] Norris DJ, Bawendi MG. Measurement and assignment of the size-dependent optical spectrum in CdSe quantum dots. Physical Review B. 1996;53:16338-46.

[80] Bullen CR, Mulvaney P. Nucleation and growth kinetics of CdSe nanocrystals in octadecene. Nano Letters. 2004;4:2303-7.

[81] Kurth DG, Lehmann P, Lesser C. Engineering the surface chemical properties of semiconductor nanoparticles: surfactant-encapsulated CdTe-clusters. Chemical Communications. 2000:949-50.

[82] Gao MY, Sun JQ, Dulkeith E, Gaponik N, Lemmer U, Feldmann J. Lateral patterning of CdTe nanocrystal films by the electric field directed layer-by-layer assembly method. Langmuir. 2002;18:4098-102.

[83] Wang W, Banerjee S, Jia SG, Steigerwald ML, Herman IP. Ligand control of growth, morphology, and capping structure of colloidal CdSe nanorods. Chemistry of Materials. 2007;19:2573-80.

[84] Ritter JJ. A novel synthesis of polycrystalline bismuth telluride. Inorganic Chemistry. 1994;33:6419-20.

[85] Ritter JJ, Maruthamuthu P. Synthesis of polycrystalline bismuth telluride by a metal-organo complex method. Inorganic Chemistry. 1995;34:4278-80.

[86] Zhao XB, Ji XH, Zhang YH, Cao GS, Tu JP. Hydrothermal synthesis and microstructure investigation of nanostructured bismuth telluride powder. Applied Physics a-Materials Science & Processing. 2005;80:1567-71.

[87] Zhou LN, Zhang XB, Zhao XB, Zhu TJ, Qin YQ. Influence of NaOH on the synthesis of Bi2Te3 via a low-temperature aqueous chemical method. Journal of Materials Science. 2009;44:3528-32.

[88] Kim SH, Park BK. Solvothermal synthesis of Bi2Te3 nanotubes by the interdiffusion of Bi and Te metals. Materials Letters. 2010;64:938-41.

[89] Zhang YH, Xu GY, Ren P, Wang Z, Ge CC. Effects of various reductants and surfactants on the nanostructure of Bi2Te3 synthesized by a hydrothermal process. Journal of Elec Materi. 2011;40:835-9.

[90] Sander MS, Prieto AL, Gronsky R, Sands T, Stacy AM. Fabrication of high-density, high aspect ratio, large-area bismuth telluride nanowire arrays by electrodeposition into porous anodic alumina templates. Advanced Materials. 2002;14:665-7.

[91] Zhao XB, Yang SH, Cao YQ, Mi JL, Zhang Q, Zhu TJ. Synthesis of nanocomposites with improved thermoelectric properties. Journal of Elec Materi. 2009;38:1017-24.

[92] Purkayastha A, Lupo F, Kim S, Borca-Tasciuc T, Ramanath G. Low-temperature, template-free synthesis of single-crystal bismuth telluride nanorods. Advanced Materials. 2006;18:496-+.

[93] Deng Y, Nan CW, Wei GD, Guo L, Lin YH. Organic-assisted growth of bismuth telluride nanocrystals. Chemical Physics Letters. 2003;374:410-5.

[94] Yu SH, Yang J, Wu YS, Han ZH, Lu J, Xie Y, et al. A new low temperature one-step route to metal chalcogenide semiconductors: PbE, Bi2E3 (E = S, Se, Te). Journal of Materials Chemistry. 1998;8:1949-51.

[95] Yuan D, Zhou XS, Wei GD, Liu J, Nan CW, Zhao SJ. Solvothermal preparation and characterization of nanocrystalline Bi2Te3 powder with different morphology. Journal of Physics and Chemistry of Solids. 2002;63:2119-21.

[96] Schlecht S, Yosef M, Weimer S, Ieee. Synthesis and characterization of nanoscale Bi2Te3, Sb2Te3, PbTe and Ag2Te powders: activated metals and soluble tellurium sources as synthetic tools2006.

[97] Purkayastha A, Kim S, Gandhi DD, Ganesan PG, Borca-Tasciuc T, Ramanath G. Molecularly protected bismuth telluride nanoparticles: Microemulsion synthesis and thermoelectric transport properties. Advanced Materials. 2006;18:2958-+.

[98] Scheele M, Oeschler N, Meier K, Kornowski A, Klinke C, Weller H. Synthesis and thermoelectric characterization of Bi(2)Te(3) nanoparticles. Advanced Functional Materials. 2009;19:3476-83.

[99] Duncan WR, Craig CF, Prezhdo OV. Time-domain ab initio study of charge relaxation and recombination in dye-sensitized TiO2. Journal of the American Chemical Society. 2007;129:8528-43.

[100] Tully JC. Molecular-dynamics with electronic-transitions. Journal of Chemical Physics. 1990;93:1061-71.

[101] Marques MAL, Gross EKU. Time-dependent density functional theory. Annual Review of Physical Chemistry. 2004;55:427-55.

[102] Hammes-Schiffer S, Tully JC. Proton-transfer in solution - molecular-dynamics with quantum transitions. Journal of Chemical Physics. 1994;101:4657-67.

[103] Kresse G, Furthmuller J. Efficiency of ab-initio total energy calculations for metals and semiconductors using a plane-wave basis set. Computational Materials Science. 1996;6:15-50.

[104] Parandekar PV, Tully JC. Mixed quantum-classical equilibrium. Journal of Chemical Physics. 2005;122:094102.

[105] Perdew JP, Wang Y. Accurate and simple analytic representation of the electron-gas correlation-energy. Physical Review B. 1992;45:13244-9.

[106] Vanderbilt D. Soft self-consistent pseudopotentials in a generalized eigenvalue formalism. Physical Review B. 1990;41:7892-5.

[107] Klimov VI, McBranch DW. Femtosecond 1P-to-1S electron relaxation in strongly confined semiconductor nanocrystals. Physical Review Letters. 1998;80:4028-31.

[108] Pulci O, Onida G, Del Sole R, Reining L. Ab initio calculation of self-energy effects on optical properties of GaAs(110). Physical Review Letters. 1998;81:5374-7.

[109] Li LS, Hu JT, Yang WD, Alivisatos AP. Band gap variation of size- and shape-controlled colloidal CdSe quantum rods. Nano Letters. 2001;1:349-51.

[110] Kim CK, Lautenschlager P, Cardona M. Temperature-dependence of the fundamental energy-gap in GaAs. Solid State Communications. 1986;59:797-802.

[111] Hang Z, Yan D, Pollak FH, Pettit GD, Woodall JM. Temperature-dependence of the direct band-gap of InxGa1-xAs (x=0.06 and 0.15). Physical Review B. 1991;44:10546-50.

[112] Joshi A, Narsingi KY, Manasreh MO, Davis EA, Weaver BD. Temperature dependence of the band gap of colloidal CdSe/ZnS core/shell nanocrystals embedded into an ultraviolet curable resin. Applied Physics Letters. 2006;89.

[113] Olkhovets A, Hsu RC, Lipovskii A, Wise FW. Size-dependent temperature variation of the energy gap in lead-salt quantum dots. Physical Review Letters. 1998;81:3539-42.

[114] Wise FW. Lead salt quantum dots: The limit of strong quantum confinement. Accounts of Chemical Research. 2000;33:773-80.

[115] Neeleshwar S, Chen CL, Tsai CB, Chen YY, Chen CC, Shyu SG, et al. Size-dependent properties of CdSe quantum dots. Physical Review B. 2005;71:201307.

[116] Reiss H. The growth of uniform colloidal dispersions. Journal of Chemical Physics. 1951;19:482-7.

[117] Yin Y, Alivisatos AP. Colloidal nanocrystal synthesis and the organic-inorganic interface. Nature. 2005;437:664-70.

[118] Peng XG, Wickham J, Alivisatos AP. Kinetics of II-VI and III-V colloidal semiconductor nanocrystal growth: "focusing" of size distributions. Journal of the American Chemical Society. 1998;120:5343-4.

[119] Lokteva I, Radychev N, Witt F, Borchert H, Parisi J, Kolny-Olesiak J. Surface treatment of CdSe nanoparticles for application in hybrid solar cells: the effect of multiple ligand exchange with pyridine. Journal of Physical Chemistry C. 2010;114:12784-91.

[120] Alivisatos AP. Semiconductor clusters, nanocrystals, and quantum dots. Science. 1996;271:933-7.

[121] Yuan L, Zhang D, Zhang J, Hu Y. shape evolution of star-shaped colloidal PbSe nanocrystals. Proceedings of the 3rd IEEE Int Conf. 2008:515.

[122] Doerk G, Carraro C, Maboudian R. Temperature dependence of Raman spectra for individual silicon nanowires. Physical Review B. 2009;80.

[123] Burke H, Herman I. Temperature dependence of Raman scattering in Ge1-xSix alloys. Physical Review B. 1993;48:15016-24.

[124] Balkanski M, Wallis R, Haro E. Anharmonic effects in light scattering due to optical phonons in silicon. Physical Review B. 1983;28:1928-34.

[125] Lu K, Sui ML. Thermal-expansion behaviors in nanocrytalline materials with a wide grain-size range. Acta Metallurgica Et Materialia. 1995;43:3325-32.

[126] Menéndez J, Cardona M. Temperature dependence of the first-order Raman scattering by phonons in Si, Ge, and α-Sn: Anharmonic effects. Physical Review B. 1984;29:2051-9.

[127] Lange H, Artemyev M, Woggon U, Thomsen C. Geometry dependence of the phonon modes in CdSe nanorods. Nanotechnology. 2009;20:045705.

[128] Manna L, Scher EC, Alivisatos AP. Synthesis of soluble and processable rod-, arrow-, teardrop-, and tetrapod-shaped CdSe nanocrystals. Journal of the American Chemical Society. 2000;122:12700-6.

[129] Scherrer P. Bestimmung der Grösse und der inneren Struktur von Kolloidteilchen mittels Röntgenstrahlen. Nachr Ges Wiss Göttingen 1918;26.

[130] Patterson AL. The Scherrer Formula for X-Ray particle size determination. Physical Review. 1939;56:978-82.

[131] Poudel B, Hao Q, Ma Y, Lan Y, Minnich A, Yu B, et al. High-thermoelectric performance of nanostructured bismuth antimony telluride bulk alloys. Science. 2008;320:634-8.

[132] Bando H, Koizumi K, Oikawa Y, Daikohara K, Kulbachinskii VA, Ozaki H. The time-dependent process of oxidation of the surface of Bi2Te3 studied by X-ray photoelectron spectroscopy. Journal of Physics-Condensed Matter. 2000;12:5607-16.

[133] Gupta RP, Xiong K, White JB, Cho K, Alshareef HN, Gnade BE. Low resistance ohmic contacts to Bi2Te3 using Ni and Co metallization. Journal of the Electrochemical Society. 2010;157:H666-H70.

[134] Gupta RP, Iyore OD, Xiong K, White JB, Cho K, Alshareef HN, et al. Interface characterization of cobalt Contacts on bismuth selenium telluride for thermoelectric devices. Electrochemical and Solid State Letters. 2009;12:H395-H7.

[135] Snyder GJ, Toberer ES. Complex thermoelectric materials. Nature Materials. 2008;7:105-14.

[136] Das VD, Soundararajan N. Size and temperature effects on the seebeck coefficient of thin bismuth-films. Physical Review B. 1987;35:5990-6.

[137] Zhao LD, Zhang BP, Liu WS, Zhang HL, Li JF. Effects of annealing on electrical properties of n-type Bi2Te3 fabricated by mechanical alloying and spark plasma sintering. Journal of Alloys and Compounds. 2009;467:91-7.

[138] Yan XA, Poudel B, Ma Y, Liu WS, Joshi G, Wang H, et al. Experimental studies on anisotropic thermoelectric properties and structures of n-type Bi2Te2.7Se0.3. Nano Letters. 2010;10:3373-8.

VITA

VITA

Liangliang Chen obtained his Bachelor degree in 2005 from Department of Materials Science and Engineering, Tsinghua University. Liang joined Purdue in Fall 2007 and worked on his Ph.D. degree with Prof. Xiulin Ruan. He expects to be granted his Doctor of Philosophy degree from School of Mechanical Engineering at Purdue University in December 2013.